Alma Mater Studiorum · Università di Bologna

Scuola di Scienze
Corso di Laurea Magistrale in Fisica

MANUFACTURING AND CHARACTERIZATION OF AMORPHOUS SILICON ALLOYS PASSIVATION LAYERS FOR SILICON HETEROJUNCTION SOLAR CELLS

Relatore:
Prof. Daniela Cavalcoli

Presentata da:
Daniele Palaferri

Correlatori:
Dott. Martin Hermle
Kurt-Ulrich Ritzau

Sessione II
Anno Accademico 2012/2013

Abstract

Nel presente lavoro di tesi magistrale sono stati depositati e caratterizzati film sottili (≈10 nm) di silicio amorfo idrogenato (a-Si:H), studiando in particolare leghe a basso contenuto di ossigeno e carbonio. Tali layer andranno ad essere implementati come strati di passivazione per wafer di Si monocristallino in celle solari ad eterogiunzione HIT (*heterojunctions with intrinsic thin layer*), con le quali recentemente è stato raggiunto il record di efficienza $\eta = 24.7\%$ [Eu-Pan13]. Lo scopo alla base di questa tesi è migliorare la stabilità termica di tali film sottili quando esposti ad alte temperature (sopra i 300°C): una elevata stabilità termica permetterebbe la post-deposizione di un TCO più conduttivo o un processo di metallizzazione a base di Ni e Cu (più economico del processo standard a base di Ag). Inoltre l'a-Si:H, nonostante l'eccellente passivazione, ha lo svantaggio principale che l'elevata esposizione termica causa due effetti di degradazione: effusione dell'idrogeno [DWo07] e crescita di cristalliti vicino all'interfaccia c-Si/a-Si [Kon07]. Tali fenomeni aumentano notevolmente la densità di *dangling bonds* non saturati, che sono il maggior centro di ricombinazione per le cariche foto-generate, e quindi riducono efficienza e *fill factor* del segnale in uscita.

La deposizione è avvenuta mediante PECVD (*plasma enhanced chemical vapour deposition*). Tecniche di spettroscopia ottica, come FT-IR (*Fourier transform infrared spectroscopy*) e SE (*spettroscopic ellipsometry*) sono state utilizzate per analizzare le configurazioni di legami eteronucleari (Si-H, Si-O, Si-C) e le proprietà strutturali dei film sottili: un nuovo metodo è stato implementato per calcolare i contenuti atomici di H, O e C da misure ottiche. In tal modo è stato possibile osservare come una bassa incorporazione ($< 10\%$) di ossigeno e carbonio sia sufficiente ad aumentare la porosità ed il grado di disordine a lungo raggio del materiale: relativamente a quest'ultimo aspetto, è stata sviluppata una nuova tecnica per determinare dagli spettri ellisometrici l'energia di Urbach, che esprime la coda esponenziale interna al gap in semiconduttori amorfi e fornisce una stima degli stati elettronici in presenza di disordine reticolare.

Nella seconda parte della tesi sono stati sviluppati esperimenti di annealing isocrono, in modo da studiare i processi di cristallizzazione e di effusione dell'idrogeno, correlandoli con la degradazione delle proprietà optoelettroniche. Per analizzare quest'ultime sono stati utilizzati strumenti come QSSPC (*quasi steady-state photoconductance*), per estrarre il tempo di vita effettivo dei portatori fotogenerati, e SunsVoc, per studiare l'*open-circuit voltage*. Per tali misure gli strati di silicio amorfo sono stati depositati su superfici sia planari che testurizzate (le quali consentono un migliore confinamento ottico). L'analisi dei differenti risultati ottenuti studiando queste particolari leghe (a-SiO_x e a-SiC_y) ha permesso di concludere che solo con una bassa percentuale di ossigeno o carbonio, i.e. ≤ 3.5 %, è possibile migliorare la risposta termica dello specifico layer, ritardando i fenomeni di degradazione. Difatti, nel caso di maggiori percentuali, la porosità del sistema facilita l'effusione dell'idrogeno e il conseguente deteriorarsi delle proprietà optoelettroniche.

ALMA MATER STUDIORUM
UNIVERSITÀ DI BOLOGNA

Fraunhofer
ISE

Abstract

In the present thesis thin films ($\approx$ 10 nm) of hydrogenated amorphous silicon (a-Si:H) were deposited and characterized, particularly studying suboxide and subcarbide alloys. These nano-sized structures will be implemented as passivation layers in HIT silicon heterojunction solar cells, which recently gave an efficiency record $\eta = 24.7\%$ [Eu-Pan13]. The aim of this work is to improve the thermal stability of these thin films when exposed at high temperatures (above 300°C): such a higher stability could allow a post-deposition of a more conductive TCO or a Cu- and Ni-based metallization (cheaper than the standard process made on silver). Indeed hydrogenated amorphous silicon, although has an excellent passivation, has the principal disadvantage that high thermal exposure causes two electronically degrading effects: hydrogen effusion [DWo07] and growth of crystallites near the interface c-Si/a-Si [Kon07]. These phenomena considerably increase the non-saturated *dangling bonds* density, which are the most relevant recombination centres for the photo-generated charge carriers; therefore they reduce efficiency and *fill factor* of the output signal.

The growth of amorphous silicon layers was done using PECVD (*plasma enhanced chemical vapour deposition*). Optical spectroscopy techniques, as FT-IR (*Fourier transform infrared spectroscopy*) and SE (*spettroscopic ellipsometry*), were used to analyse the hetero-nuclear bonds configurations (Si-H, Si-O, Si-C) and to investigate the structural properties of amorphous silicon thin films: a new method was implemented to calculate the atomic content of H, O e C using only optical systems. Thus it was possible to observe how a low incorporation ($< 10\%$) of oxygen and carbon atoms is enough to increase the porosity and the long range disorder of the studied material: pertinent to this aspect, a new technique was developed to determine the Urbach energy from ellipsometric spectra, which expresses the exponential tail inside the amorphous semiconductors gap, being linked to disorder electronic states.

In the second part of the thesis isochronical annealing experiments were performed, to study and correlate the crystallization process, the hydrogen effusion and the degradation of optoelectronic properties: for the latter case, instruments like QSSPC (*quasi steady-state photoconductance*), to extract the effective lifetime of photo-generated charge carriers and SunsVoc, to observe the *open-circuit voltage*, were used. The amorphous silicon layers were deposited on planar and texturized surfaces. The analysis of the different results, produced studying these particular alloys (a-SiO_x and a-SiC_y), brought to the conclusion that only with a small percentage of oxygen and carbon, i.e. ≤ 3.5 %, it is possible to improve the thermal response of the specific layer, retarding the degrading phenomena. Indeed, in the case of higher atomic percentage, the system porosity facilitates the hydrogen effusion and the opto-electronic degradation.

ALMA MATER STUDIORUM
UNIVERSITÀ DI BOLOGNA

Fraunhofer
ISE

Contents

Introduction

Photovoltaic solar energy technology (PV) is one of the solutions to the ever-growing global energy demand, providing a stable and renewable energy source to sustain basic human needs.

Considering the actual research on PV, an interesting technology is represented by the heterojunction silicon solar cells (SHJ), that can reach high efficiency, i.e. a conversion of solar energy in electric power of almost 25 %[1], with a rather simple and fast manufacturing process. These particular cells are a combination of two different structural phases of silicon: the crystalline wafer (Float-zone or Czochralski, $\approx$ 200 μm), as absorber of the solar radiation, being coated on both sides with thin films of hydrogenated amorphous silicon (a-Si:H). The a-Si:H serves both as a passivation layer to decrease the surface recombination as well as a selective contact depending on respective doping. The final structure is composed by a transparent conductive oxide (TCO), used to transport the photogenerated charge carriers to the metallic contacts, acting as electrodes.

Motivation

The SHJ solar cell has several advantages over standard Si photovoltaics (based on p-n homojunctions). The manufacturing needs shorter time, lower temperature and thinner wafers and reduces the number of production steps. Also, the **HIT** (heterojunctions with an intrinsic thin layer) cell concept [Tan92], with the implementation of intrinsic films, improves the efficiency.

However, a low temperature production process imposes the use of special metal pastes to build up the electric contacts: the standard *screen printing* is made at around $T \approx 800$ °C, while the metal alloys actually investigated for SHJ, are cured in a range $T = 200 \div 600$ °C [DWo12]. The metallization process is intimately correlated to the thermal stability of the thin films: when exposed to temperatures higher than 200 °C, excellent passivation properties of a-Si:H layers degrade, due to hydrogen effusion, with result in a drop of the cell efficiency. Therefore the H loss strongly restricts the upper

[1] Recently, on 13 Febrary 2013, Sanyo Panasonic Eletronics announced it achieved a record conversion efficiency of 24.7% with SHJ solar cell [Eu-Pan13]

temperature required for curing of metal pastes. A higher temperature stability of the passivation layers could enable metallization with both increased conductivity and less additional components, reducing its specific cost. Since metallization is the second most expensive part in cell production (after the wafer cost), lowering the restraints on SHJ metallization would make this cell concept with few production steps even more attractive.

In order to improve the thermal stability of the passivation, alternatives to standard a-Si:H passivation layer, i.e. alloys of amorphous Si constituted by low incorporation ($< 10\%$) of oxygen and carbon atoms, were deposited and characterized within the framework of this master thesis.

The studied thin layers can be implemented into the HIT concept, which requires a low temperature metallization step (for example *screen printing* of silver containing metallic pastes), allowing a better thermal response and a reduced electronic degradation of the heterojunction. This would allow the use of higher annealing temperatures thus less expensive components for the paste and lead to higher specific conductivity. An other possible application could be the implementation in the hybrid concept of a SHJ [Biv10], designed with an amorphous silicon emitter on the back and a diffused front contact with dielectric passivation: the metal in this case directly contacts the crystalline silicon (c-Si) and, in the case of Ni, forms a silicide at around 450 °C, leading to a high degree of mechanical adhesion to the c-Si [Mon13]. The Ni also serves as a diffusion barrier to copper (Cu) and thus allows the replacement of Ag with the less cost intensive Cu.

The entire work was realized at the *Fraunhofer ISE (Institute for Solar Energy Systems)*, Freiburg im Breisgau.

Structure of the thesis

In the first and the second chapter the fundamental parameters of solar cells' physics and the structure and properties of a silicon heterojunction solar cell are exposed.

The structural and electronic properties of a-Si thin films are shown in the third chapter, focusing on the particular alloys a-SiO_x:H and a-SiC_y:H.

This is followed by the fourth chapter highlighting the deposition process, the *plasma enhanced chemical vapour deposition*(PECVD) setup and the parameters used for the deposition of thin layers.

The fifth chapter outlines the characterization methods, explaining the physical mechanisms and its technical realization. Additionally, the assumptions to evaluate the results are explained.

Then the overall experimental results of this study on a-SiO_x:H and a-SiC_y:H are presented and discussed in the sixth chapter.

A short summary and conclusion form the last part of the thesis.

CHAPTER 1

Basic Principles of Solar Cells

In this first chapter the physical properties of solar cells and the fundamental parameters used to define them will be presented. A basic introduction to the recombination mechanism of photo-generated charge carriers will be given as well. For a more detailed description the reader is referred to [Sog06] *and* [Pved].

1.1 p-n junctions

The solar cell is a device that converts solar radiation to electric power. In most cases, the base material is a semiconductor, where the absorption of photons with energies exceeding the band gap produces electron-hole pairs. Hence, implementing a p-n junction, it is possible to separate the charge carriers by the depletion region at the interface.

Considering a general case, the depletion region can be seen as a consequence of the thermal equilibrium established connecting two differently doped semiconductors: the diffusion of carriers due to the large carrier concentration gradients (holes diffuse from p-type semiconductor to n-type semiconductor and electrons diffuse from n-type semiconductor to p-type semiconductor) is balanced by drift currents due to an electric field formed in a layer without mobile charge carriers and just ionized impurity atoms. An other consequence of the equilibrium is the alignment of the Fermi levels of p-type and n-type semiconductors.

The electrostatic potential difference between the p-type semiconductor and the n-type semiconductor at thermal equilibrium is called built-in potential V_b and is given by:

$$V_b = \frac{kT}{q} ln \left(\frac{N_A N_D}{n_i^2} \right) \ , \tag{1.1}$$

where N_A and N_D are the concentrations of the acceptor and donor in p-type and n-type semiconductor, respectively; n_i is the intrinsic carrier concentration, T is the equilibrium temperature, q the electron charge and k the Boltzmann constant. When

the p-n junction is not illuminated and a *forward bias voltage* V_F is applied, the built-in potential and the drift current are reduced, while the diffusion of electrons and holes increases from the n-side to the p-side and from the p-side to the n-side, respectively; therefore, considering the minority carrier injection, it is possible to express the total current density as:

$$J = J_0 \left(e^{\frac{qV_F}{kT}} - 1 \right) , \tag{1.2}$$

where J_0 is the saturation current density. When a *reverse bias* V_R is applied, the electrostatic voltage is increased and the total current density is:

$$J = J_0 \left(e^{\frac{-qV_R}{kT}} - 1 \right) . \tag{1.3}$$

It is necessary to specify that equations 1.2 and 1.3 represent just an ideal case. A real behaviour of the p-n junction considers the recombination effects at the forbidden energy gap: equation 1.4 shows a more general formula for the forward-current density:

$$J = J_0 \left(e^{\frac{qV_F}{nkT}} - 1 \right) , \tag{1.4}$$

where n is the ideality factor, having a value between 1 and 2: in the ideal case, when the diffusion current dominates, $n = 1$, while in the real case, when the recombination current dominates, $n = 2$.

1.2 Fundamental parameters of solar cell

When the p-n junction is illuminated, the number of electron-hole pairs is proportional to the light intensity (number of incident photons): the resulting excess charge carrier density will contribute to the photo-current flowing in the space-charge region.

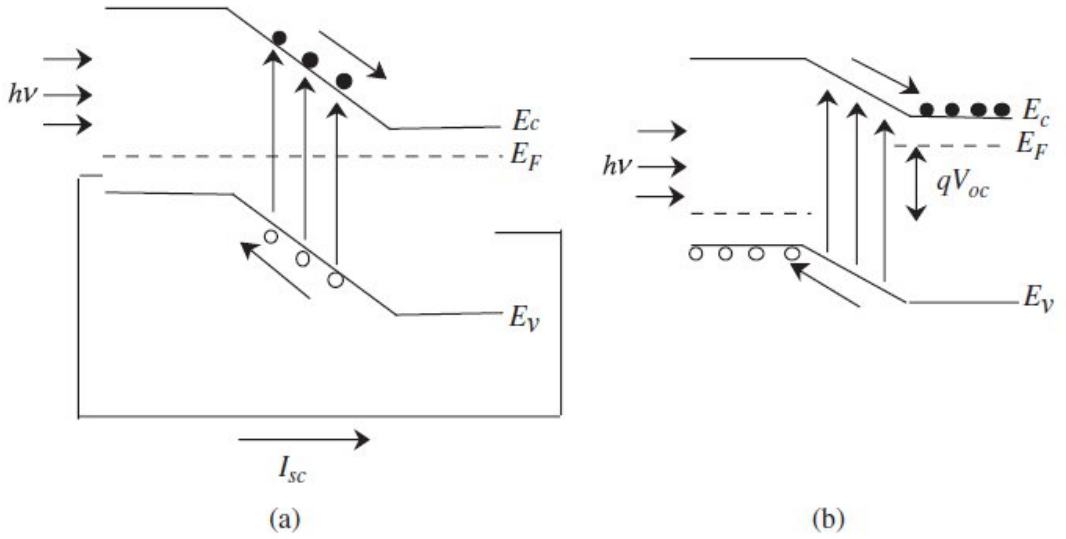

Figure 1.1: Energy band diagrams of illuminated p-n junction in the short-circuited (a) and open-circuited configuration (b), from [Sog06].

When the p- and n-side are short-circuited, the current is called the short-circuit current I_{SC} and $I_{SC} = I_L$, i.e. the photogenerated current, if the series resistance is zero. When

the p-n junction is open-circuited, the *open-circuit voltage* V_{OC} is generated due to the charge carrier separation and represents the difference between the two Fermi levels. Fig. 1.1(a) and (b) show the variations of the energy band diagram induced by these two cases.

The I-V characteristics for p-n junction under illumination and darkness is reported in Fig.1.2. The equation representing the case under light exposure is

$$I = I_0 \left(e^{\frac{qV}{nkT}} - 1 \right) - I_{SC} \ . \tag{1.5}$$

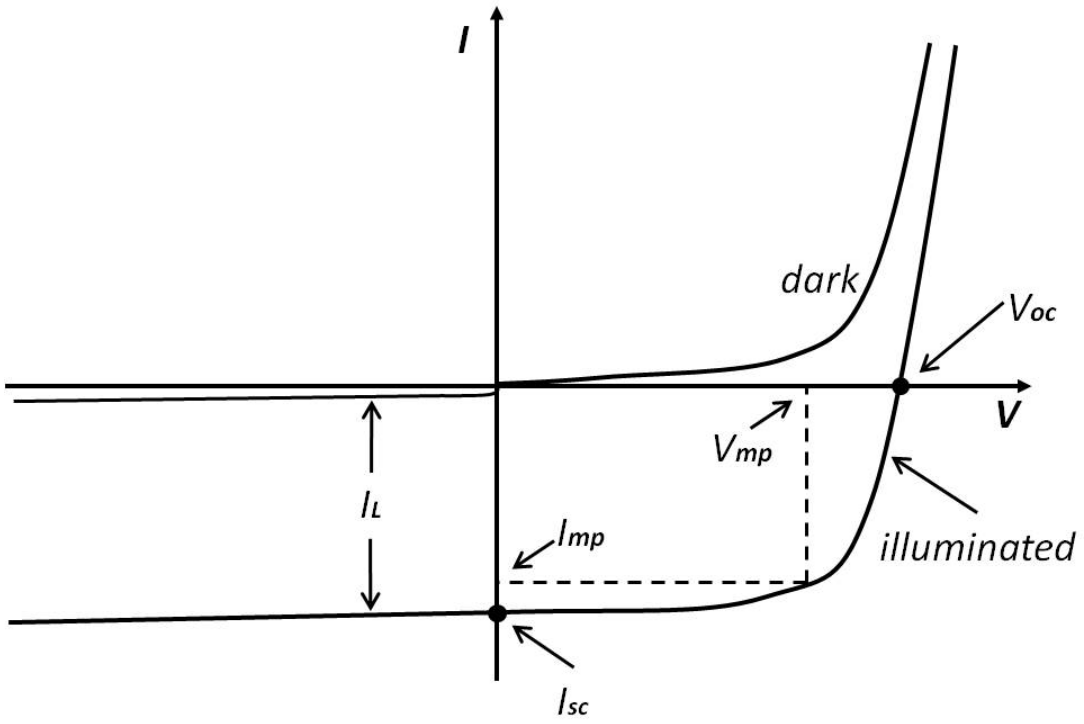

Figure 1.2: Current-voltage characteristics of p-n junction under illumination and darkness, from [Pri11].

When the junction is open-circuited (for $I = 0$), is possible to obtain the voltage:

$$V_{OC} = \frac{nkT}{q} ln \left(\frac{I_{SC}}{I_L} + 1 \right) \ . \tag{1.6}$$

Considering the condition under which the solar cell gives the maximum output power, it is possible to extract the *optimal operation points* V_{mpp} and I_{mpp}, also called the *maximum power points*. Two further important parameters to study the functionality of solar cells are the $fill\ factor\ FF$ and the conversion efficiency η, respectively in equation 1.7 and 1.8 .

$$FF = \frac{V_{mpp} I_{mpp}}{V_{OC} I_{SC}} \tag{1.7}$$

$$\eta = \frac{V_{mpp} I_{mpp}}{P_{in}} = \frac{V_{OC} I_{SC} FF}{P_{in}} \tag{1.8}$$

where P_{in} is the total power of the incident light.

1.3 Recombination paths

As mentioned above, the output current I flowing from a p-n junction solar cell has not an ideal behaviour, but is affected by the recombination of charge carriers: equation 1.9 describes the real case.

$$I = I_{ph} - I_{rec} = I_{ph} - I_{bulk\ rec} - I_{surf\ rec} - I_{cont\ rec} \tag{1.9}$$

where I_{ph} is the photo-generated current, I_{rec} the total recombination loss, $I_{bulk\ rec}$, $I_{surf\ rec}$ and $I_{cont\ rec}$ are the terms due to bulk, surface and contact recombination, respectively.

In the next two paragraphs the bulk and surface recombination will be analysed in detail as their microscopical mechanism is crucial for the scope of this thesis.

1.3.1 Bulk recombination

Recombination in the semiconductor bulk can be classified in three different phenomena, namely radiative recombination, Auger recombination and defect recombination via localized energy states in the forbidden energy gap. The first two are intrinsic material properties whereas the last is determined by the manufacturing process. To examine in depth this process it is useful to define the recombination lifetime as

$$\tau = \frac{\Delta n}{r} \ , \tag{1.10}$$

where Δn is the excess carrier density created by illumination and r is the recombination rate.

The direct (or radiative) recombination can be seen as the reverse process of photon absorption: the transition of an electron from the conduction band to the valence band results in a electron-hole pair annihilation, emitting the excess energy as a photon. The r_{rad} for this case is:

$$r_{rad} = B(pn - n_i^2) \ , \tag{1.11}$$

where B is the Einstein coefficient, determined experimentally as $B = 9.5 \times 10^{-15} cm^3/s$ at 300 $^\circ C$ [Sch74]. For indirect band gap semiconductors (such as silicon) this value is very small and therefore can be neglected in Si solar cells analysis.

The recombination due to traps in the energy gap is an intensely studied recombination process as this phenomenon is correlated to the presence of defects or impurities in the semiconductor. Shockley, Read [Sho52] and Hall [Hal52] have formulated the theory for this case in 1952: the recombination rate for a single defect level can be expressed as

$$r_{SRH} = \frac{pn - n_i^2}{\tau_{po}(n + n_l) + \tau_{no}(p + p_l)} \ , \tag{1.12}$$

where τ_{po} and τ_{no} are the fundamental hole and electron lifetimes which are related to the thermal velocity of charge carriers v_{th}, the density of the investigated defects N_t, and the capture cross-sections σ_p and σ_n for holes and electrons, respectively:

$$\tau_{po} = \frac{1}{\sigma_p v_{th} N_t} \quad and \quad \tau_{no} = \frac{1}{\sigma_n v_{th} N_t} \ . \tag{1.13}$$

The factors p_l, n_l in equation 1.12 are statistical factors defined by the potential ψ_i referenced to the intrinsic level and E_t the energy level of the defect:

$$p_l = n_l exp\left(\frac{\psi_i - E_t}{kT}\right) \quad and \quad n_l = p_l exp\left(\frac{\psi_i - E_t}{kT}\right) \ . \tag{1.14}$$

The total recombination rate due to defects in the bulk will be the sum of the recombination rates of the different defects, as they occur independently.

The Auger recombination is a three bodies process: the amount of energy due to an electron-hole annihilation causes the energy transfer to a third particle (electron or hole). The recombination rate is:

$$r_{Auger} = C_n p n^2 - n_0^2 p_0 + C_p n p^2 - p_0^2 n_0 \ . \tag{1.15}$$

Anyway, depending on the injection level of the Si-based system, the coefficients could be neglected from the calculation of recombined charges in the semiconductor.

1.3.2 Surface recombination

On surfaces of semiconductors (or on interfaces if we consider a multi-layer system) the not fully bonded atoms of the layer (*dangling bonds*) represent intrinsic defects where the carriers can recombine very efficiently.

The SRH model for bulk defects has to be modified to derive the surface recombination rate

$$r_S = \frac{p_S n_S - n_i^2}{\frac{n_S + n_l}{S_{po}} + \frac{p_S + p_l}{S_{no}}} \ , \tag{1.16}$$

where n_S, p_S are the concentrations of electrons and holes at the surface, and S_{n0}, S_{p0} are the fundamental surface recombination velocities of electrons and holes proportional to the density of surface states per unit area N_{ts} and to the capture cross-sections σ_p, σ_n for the specific defect by

$$S_{n0} = \sigma_n v_{th} N_{ts} \quad and \quad S_{p0} = \sigma_p v_{th} N_{ts} \ . \tag{1.17}$$

Defining the charge carriers losses at the surface with Δn_S, it is possible to derive the relation:

$$r_S = S \Delta n_S \ , \tag{1.18}$$

where S is the surface (or interface) recombination velocity. This parameter depends on the injection level of the semiconductor, but also on the surface condition, so it is widely used to check the accuracy of a passivation mechanism at the surface, applied to saturate the dangling bonds. This topic will be analysed in detail in the next chapter.

CHAPTER 2

Silicon Heterojunction Solar Cell

In this chapter the concept of silicon hetero-junction solar cells is explained and each constituent layer is analysed in detail. In the last part the parasitic absorption and the transparency of the constituent materials are discussed, comparing them with a standard solar spectral irradiance.

2.1 Introduction: PV based on c-Si wafer

A mono-crystalline silicon wafer is a flat material realized by sectioning an highly pure monocrystalline Si ingot: its typical thickness is in the range of 100 - 200 μm.

The Si ingot can be grown by the Float-zone method (FZ crystal growth), based on zone-melting principle: under vacuum or inert gas atmosphere, a high-purity polycrystalline rod and a monocrystalline seed crystal are held face to face in a vertical position; then they are rotated and partially melted by an induction radio-frequency circuit; finally the melt zone is moved along the polysilicon rod, solidifying in single-crystal material. An other well-known process is the Czochralski method (CZ crystal growth), that consists in melting polysilicon inside a rotating crucible of quartz: a single crystal silicon seed is placed on the surface and gradually drawn upwards, taking up the molten silicon that solidifies in single crystal. The first (FZ) produces the highest quality and is mainly used in research; the latter (CZ) is for industrial cell production.

Given the wide use in electronics device, in 1954 [Cha95] silicon p-n junction was first used to produce a solar cell, obtaining an efficiency η of 6%.

Nowadays more than 90 % of the current production uses first generation PV wafer based crystalline silicon. As reported in [vSa11], [EUPV07], the direct production costs for c-Si modules are around 1 €/W_p[1] in 2013, and are expected to go below 0.75 €/W_p in 2020 and lower in the long term, as stated in the Strategic Research Agenda of the European Photovoltaic Technology Platform. So the household cost of electricity from the grid is now higher than the production on the using rooftop PV in sites like

[1]The W_p (Watt-peak) indicates the cost production of a PV module exposed to a Sun Spectra of 1.5 AM, with irradiation of 1.00 kW/m^2 and a cell temperature of 298.15 K

southern Germany and even more e.g. in Italy.

From the last 2 decades the photovoltaic technology has focused on optimization of efficiencies and reduction of costs: the thin film investigation enabled 2 new generations of PV, adding innovative scientific concepts and new kinds of absorber material (respect to the conventional Si). The ever increasing interest in nanotechnology, photonics, optical metamaterials and organic semiconductors allow new cell concepts to enter production: thin film silicon (TFS), cadmium telluride (CdTe), copper indium selenide (CIS), organic cells etc...

2.2 The heterojunction concept

Crystalline silicon-based solar cells can be divided into two main groups: homojunction wafer-based crystalline silicon (c-Si) solar cells and heterojunction silicon solar cells.

The homojunction solar cell simply consists in a pn structure of c-Si with a homogeneous band gap and the same electron affinity: as can be seen in the diagram structure of figure 2.1 .

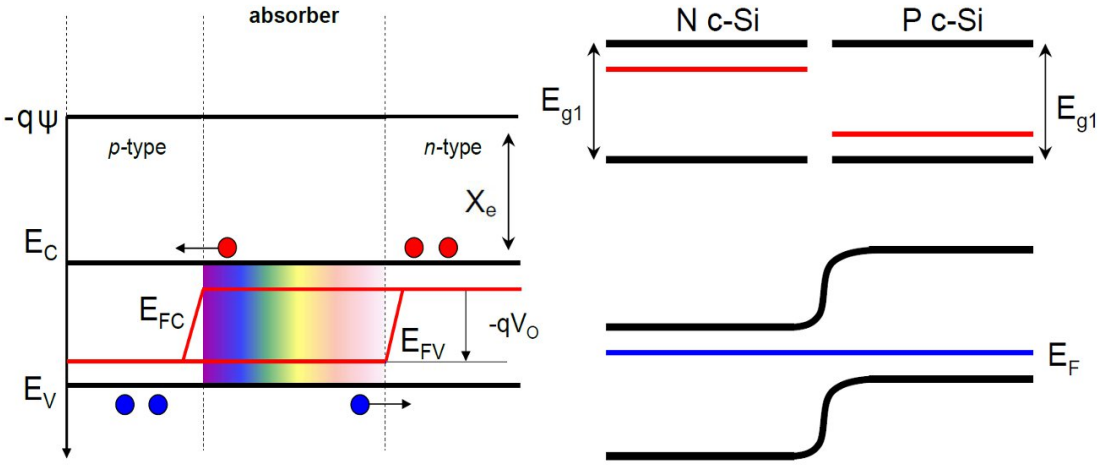

Figure 2.1: pn Homojunction, from [vSa11]

When light is absorbed the created charges (electrons or holes) move to the electrodes (placed at the front and at the rear side of the junction) through the p or the n side, creating a majority and a minority current: this last one is detrimental for Auger recombination losses at the junction, because the minority charge will recombine in the oppositely doped layer, reducing the output conductivity. An other higher recombination center of the homojunction cell is the direct contact with the electrode: the border metal-semiconductor is a high active losses region for this kind of cell and limits V_{oc} [DWo12].

The thin film silicon solar cell consist of an homojunction, and the used semiconductor does not have to be c-Si, but a-Si or μ-Si to obtain a low-cost of the cell production. However due to light induced degradation and low growth rates for μcSi this concept has a declining market share.

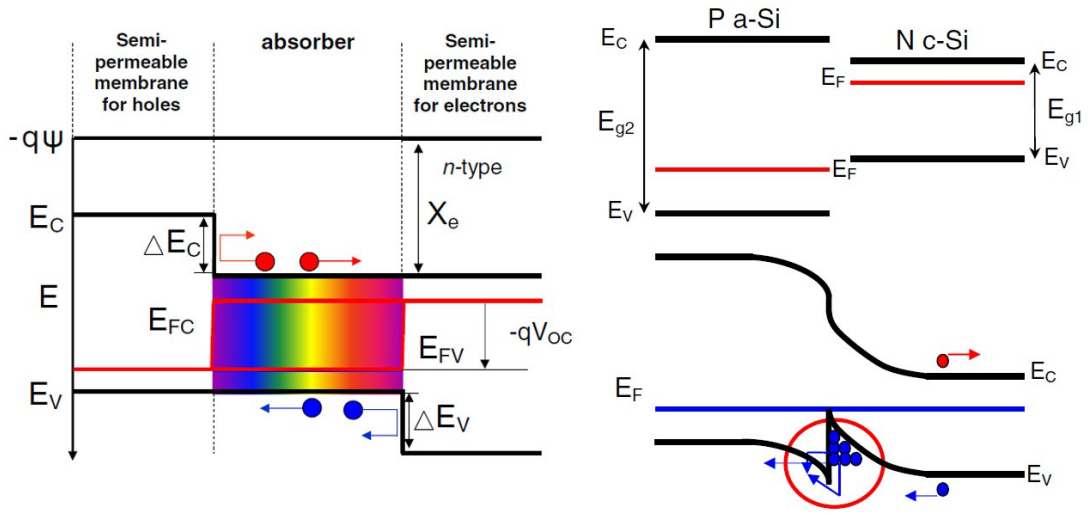

Figure 2.2: pn Heterojunction diagrams, from [vSa11]

The heterojunction solar-cell is a combination of the c-Si homojunction and with an a-Si thin-film: the c-Si serves as the absorber and on both sides the amorphous silicon passivates the surfaces and creates a selective contact through respective doping enabling the extraction of charge carriers created by incoming photons. In the band diagram of this case, the a-Si has a higher energy gap (see figure 2.2), so at the contacting point there will not just be the band bending due to the different doping level, but also due to different electron affinities. This energy offset ΔE_C or ΔE_V (difference between E_{g-cSi} and E_{g-aSi}) results in a potential barrier that was absent in the homojunction case and that allows just one type of charge to pass through. For this reason the a-Si layers are referred to as "semi-permeable" membrane, being a fundamental advantage as it reduces the recombination losses of the photo-generated carriers.

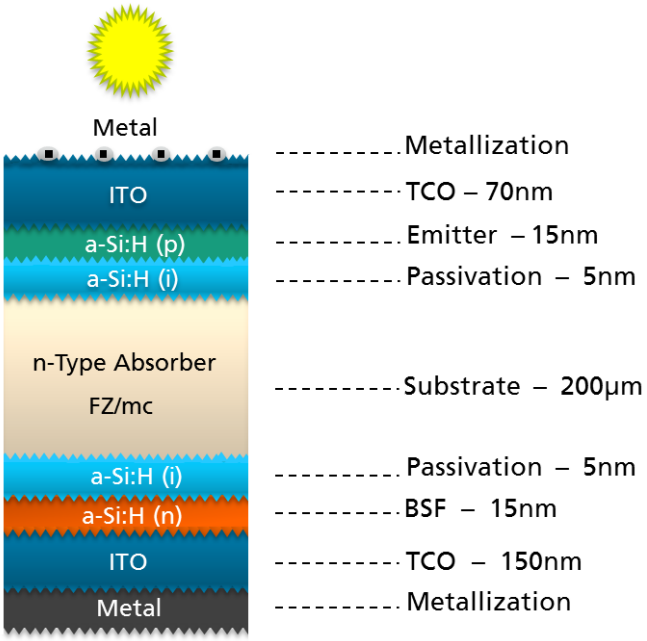

Figure 2.3: Silicon heterojunction sketch

The SHJ electrical transport is partially diffusive and dominantly with tunnelling carriers, as observed in [Sch10]. A common criterion to deposit a-Si on the absorber is maintaining the thickness of the layers as low as necessary to avoid parasitic absorption losses (see paragraph 2.3): the a-Si buffer layers are in an usual range of 5-10 nm.

The final structure of a typical SHJ is shown in the figure 2.3: this sketch has texturized layers on the top to enhance light trapping. In this work samples with planar layers were studied as well. Furthermore the reader should keep in mind that the sketch is not to real scale: next to each layer the respective thickness is shown.

In the next sub-paragraphs all single layers are analysed in detail.

2.2.1 Planar and texturized wafers

Planar <100> wafers can be texturized to enhance light trapping. The texturization process is based on etching the surfaces of c-Si with potassium hydroxide (KOH) and isopropanol (IPA), obtaining a random distribution of inverted pyramids with <111> oriented lateral facets and a higher probability of light absorption respect to flat surfaces. The pyramids are formed because the surfactants act differently depending upon which crystal facet is exposed: Bean [Bea78] explained this anisotropical etching phenomenon, showing that <100> surfaces are etched faster than <111>. The typical pyramid base length is $\approx 3 \div 8 \mu m$ [Mun09].

2.2.2 Passivation by hydrogenated amorphous silicon: insertion of intrinsic layer

An important issue for designing an highly efficient SHJ is the reduction of the recombination centres at the interface of the heterostructure. As mentioned in the first chapter, the SRH defects are the main recombination centres and are due to silicon dangling bonds on the surface of c-Si and inside the disordered structure of a-Si.

The typical passivation technique is the hydrogenation, as the H is a light element that can easily diffuse between interstitials of silicon without perturbing the lattice structure until saturating vacancy of the missing Si-X bond.

Observing the c-Si structure, it was noted [Hig90] that <100> oriented surfaces have 2 dangling bonds per unit cell, while <111> surfaces have just 1 dangling bond per unit cell resulting easier to passivate: the ideal monohydride termination is more favourable and requires less formation energy than more complex hydrogenated bonds [DWo10].

The a-Si:H films in SHJ have a double aspect: they are semi-permeable membrane to increase majority charge diffusion and are also passivating layers to avoid the recombination in the vacancies of silicon dangling bonds.

Anyway the output results (I-V, FF, η) are affected as well from the doping of the layers and, as was observed by DeWolf [DWo12], a doped a-Si:H layer causes drastic passivation losses, because the doping increases the defect density in the Urbach tails of the a-Si density of states (see chapter 3). The solution to this problem was proposed by Sanyo [Tan92], producing the first HIT cell (Heterojunction with Intrinsic Thin layer): a few nanometers intrinsic a-Si film is deposited between the absorber and the doped

a-Si, improving the passivation quality (in terms of effective carrier lifetime [DWo12]) and the efficiency. The intrinsic layer is usually deposited on rear and front side (as shown in the sketch of cell, figure 2.3).

One disadvantage of amorphous silicon is the poor thermal stability due to H effusion [DWo07] and the increase of crystallites in the amorphous layer close to the interface [Kon07]. For this reason, in the present work alternatives to the a-Si:H passivation layers are studied in order to reduce those high temperature degrading effects: in particular suboxide and subacarbide alloys of amorphous silicon will be deposited, since a low ratio of atomic heterogeneity (1-10 % of Si-O, Si-C bonds) is believed to improve the thermal response of the single thin film, without affecting the above mentioned good qualities of a-Si:H; for informations regarding a-SiO_x:H and a-SiC_y:H, the reader is referred to the next chapter, section 3.2.

2.2.3 Transparent conductive oxide

The doped amorphous silicon layers do not provide sufficient conductivity to transport charge to the device terminals (metal fingers) in the lateral directions. Hence a *transparent conductive oxide* is deposited above the doped a-Si:H, prior to metal printing. The TCO has a high bandgap and is highly degenerated (n^{++}), leading to high conductivity and transparency. Since more charge carriers lead to higher parasitic absorption, the optimization of two quantities is a result of a trade off.

The thickness of this layer is chosen to minimize reflection which is the case for ≈ 70-80 nm. Sputtered indium tin oxide is the material largely used for SHJ device, due to its high mobility and high transparency values.

2.2.4 Metallization

Screen printing is the predominantly used metallization process in c-Si PV. For standard homojunction solar cells the metal is deposited in paste form, with ≈ 20% of organic solvent and ≈ 80% of solid containing the metal itself and the glass frit (the latter is necessary to open the dielectric layer and create the contact with c-Si). These pastes are forced through a screen on the substrate by the action of a squeegee: the typically used metals are Ag for n^+ surfaces and Al for p^+ surfaces. Then the printed electrodes are dried at 200°C and subsequently fired up to 800°C, to evaporate the organic content and establish the contact.

The high-temperature firing step of standard screen printing can cause H effusion from a-Si:H and losses of its passivation properties. Therefore, considering SHJ solar cells, different low temperature metallization processes are investigated, in order to avoid the thermal degradation. The screen printing in this case is applied as well: polymer based pastes (without glass frit) of silver or copper (for TCO surfaces) are printed and then annealed at around 200 °C. The low-temperature *sintering* leads to more resistive electrodes and a reduced conductivity as compared to standard pastes for c-Si homojunction cells. Alternatives used in the labscale *R&D* to the screen printing are the sputtered/thermal evaporated metal stacks, like Ti/Pd/Ag (good contact) or Cr/Ag (good adhesion on TCO, but safety risky for chromium toxicity). In PVD

metallization pure metals are used (more conductive than pastes) and the contacts can be defined by photolithography or shadow mask.

Recently, alternative copper-based metal plating is investigated. The silver is highly conductive but also highly expensive. The Cu is available for roughly 1% of the price of the Ag, and seems to be an attractive candidate for the metallization process. Recently Hernandez built a Cu-based SHJ, obtaining a record efficiency of 22.1% [Her2012].

An other interesting metallization scheme is currently investigated with a metal alloy CuNi [Mon13]: at 450 °C, a silicide forms out in the interface of Ni/c-Si, leading to a high degree of mechanical adhesion between electrodes and substrate. The Ni also serves as a diffusion barrier to the copper. This could be implemented in a hybrid heterostructure (designed with an amorphous silicon emitter in the back and a diffused front contact with dielectric passivation) [Biv12], but therefore thermal stability has to be improved.

The metal contacts of a solar cell have a typical thickness in the range 10 to 20 μm.

2.3 Absorption losses in a SHJ solar cell

As specified in the introduction, a c-Si cell can have a theoretical upper efficiency limit of $\eta = 29.43\%$ (as recently calculated [Ric13]). This parameter is due to the number of the absorbed photons and the number of photo-generated charge carriers that arrive to the electrodes.

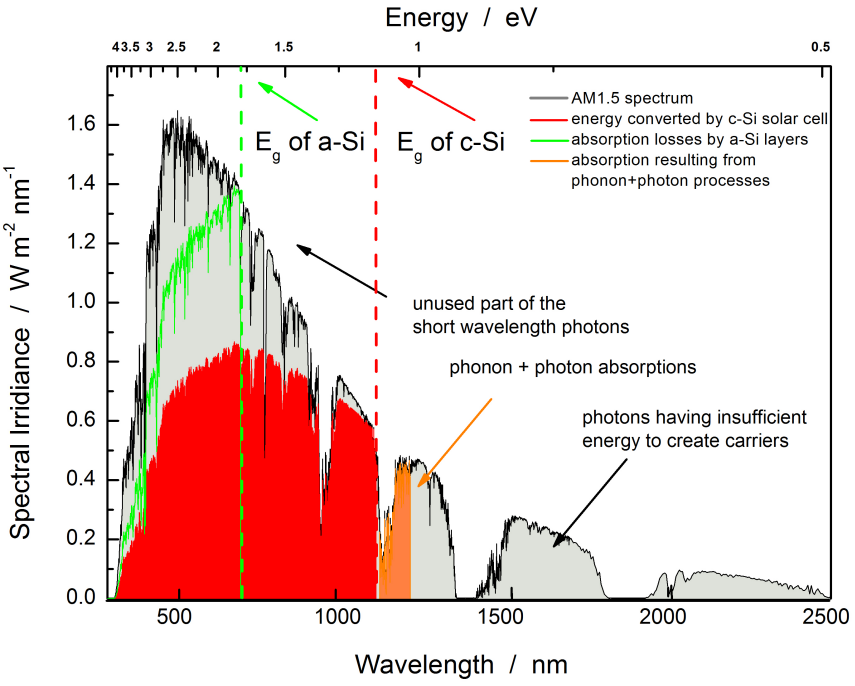

Figure 2.4: Solar spectrum AM1.5, showing the absorption ranges of c-Si and a-Si

As the heterojunction is a multilayer-structure, and the a-Si and the TCO are semiconductors with a specific energy gap, there can be the so called *parasitic absorptions*: photons not absorbed by the c-Si wafer reduce drastically the short-circuit density J_{sc}.

A compromise to reduce the parasitic absorption is reducing the thickness of the a-Si layers, but leaving them thick enough to passivate and collect charge carriers (less than 15 nm). The thickness is related to the absorption by the Lambert-Beer relation:

$$T = \frac{I_t}{I_0} = exp(-\alpha d) \tag{2.1}$$

where I_t and I_0 are the intensity of the radiation, respectively, transmitted and incident; α is the absorption coefficient, T is the Transmittance and d is the thickness of the absorbing layer.

The figure 2.4 represents in grey the solar spectrum at air mass 1.5 (AM1.5): it indicates the average irradiation arriving to the earth, taking into account the absorption in the atmosphere in European latitudes. In red and green the absorption ranges of c-Si and a-Si are shown, denoting the specific energies (or wavelengths) at which the photon density losses can occur.

CHAPTER 3

Properties of Amorphous Silicon and its Alloys

Thin film silicon exists in different structural phases: amorphous, micro-crystalline, poly-crystalline and single crystalline. In this chapter the network concept and the electronic structure of a-Si, the rule of passivating H, the sub-oxides and the sub-carbides alloys studied in this thesis will be presented.

3.1 Hydrogenated amorphous silicon

3.1.1 Structural properties

The amorphous silicon is a typical tetrahedrally bonded amorphous solid, where the phase structure lacks of long-range order (LRO), the common index of crystalline lattice periodicity, but maintains short-range order (SRO) due to nearest neighbours of a single Si atom.

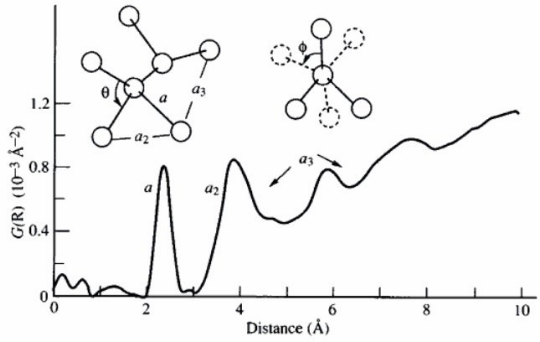

Figure 3.1: RDF by X-rays diffraction of a-Si:H, from [Str91]

In figure 3.1 the radial atomic distribution function (RDF) of a-Si:H can be seen: the RDF measures the probability of finding a particle at a distance of R away from a given reference particle; it is usually expressed as

$$RDF = G(R) = 4\pi R^2 \rho dR \tag{3.1}$$

where ρ is the average number density of particles. The presence of SRO in a-Si is confirmed by the ordered sequence and shape of the first three peaks corresponding to the 3 nearest neighbours.

The SRO can be defined as well in the small deviations that characterize the bond length and the bond angle of Si-Si network (shown also in the picture): considering the diamond structure with bond length 2.33 Å and bond angle 109.5°, the amorphous lattice shows a fluctuation from the crystalline parameters of ±10 % and ±5 %, respectively. The diameter d_{SR} of SRO region is related to the disorder parameter α by [Kra72]:

$$d_{SR} = \frac{a}{2\alpha} \tag{3.2}$$

where a is next-neighbour interatomic distance, defined by the lattice constant of diamond structure $a = \sqrt{3}a_0/4$.

As Zachariasen calculated for glass structure and silicates in 1930s [Zac32], the amorphous silicon can be modelled using the continuous random network (CRN), where the LRO is not respected by the random chaotic distortions of bond lengths and angles. An ideal coordination number C calculated with numerical methods is 2.45 [PhysRut] but, as shown by many experiments in the last decades, the real C is much lower [Phs79]. A four-fold CRN model is a strong approximation and the real material has a more complex structure. There are dangling bonds (see next paragraph), atomic miscoordination defects, voids (of tens to hundreds of angstroms in diameter) and crystalline grains (paracrystallites) that cannot be excluded from the analysis of this material and that influence the general, non-ideal, properties.

3.1.2 Si dangling bonds, band diagram and DOS

The propagation of long range disorder (LRD), due to progressive compounding of small deviations, corresponds to accumulation of structural stress: the consequent network relaxing causes bond breakings and the appearance of dangling bonds in the lattice.

This kind of defects have an amphoteric behaviour: they can be neutral or related to a charge presence (accommodation of a second electron or electron missing), with the corresponding charge state $Q = 0, \pm 1$. Indeed their presence causes charge recombinations and degrades the electronic properties of amorphous silicon based devices.

To build the electronic structure of the a-Si layer the presence of the dangling bonds should not be neglected, because they originate defect states deep in the band gap. These are due to a crucial correlation between defects and electronic density of states (DOS). Usually the density of silicon dangling bonds $N_d^Q(E)$, with associated charge state Q, are identified as a gaussian distribution centred around E_d (defect state) with width σ_d:

$$N_d^Q(E) = N_{0d}^Q exp\left(-\frac{(E - E_d^Q)^2}{2\sigma_d}\right) \tag{3.3}$$

How this density influences the electronic structure can be found in literature in more detail ([Stu89], [vSa11]).

As shown in figure 3.2 the gaussian curve is inside the energy gap, making part of the *localized states*. An other important aspect that distinguishes amorphous and

crystalline silicon is that valence and conduction band do not decrease sharply to zero, but exponentially: this gradual attenuations of the band edges are the commonly called Urbach tails. This can be seen in the more detailed logarithmic plot.

The tails represent the degree of disorder, as they are originated from the LRO of the amorphous structure: the fluctuations of binding angles and atomic distances in a-Si, and the strain of the network allow an exponential distribution of energy states that are absent in c-Si. The parameter to define them is the Urbach energy E_U, as the decay of DOS in the valence band can be written as $N(E) \propto exp(-E/E_U)$. The band tails have been found in many disordered materials, the first were impure AgBr crystals [Urb53]. In a-Si:H grown by PECVD the Urbach tails for the valence band and the conduction band are, respectively, 45-80 meV and 25 meV: the first one is directly connected to the structural disorder, the second one is dominated by the thermal disorder. As can be found in literature (e.g. [Pow93], [Sch11]) the Urbach energy is associated to the density of strained Si-Si bonds, i.e. the weak silicon bonds that can be inter-converted into dangling bonds. The amount of the disorder defines the range of energy values associated at several dangling bond states. The defects formation energy corresponds to particular conditions that minimize the free energy of the layer system; such conditions depend on the DB charge state Q and the Fermi-energy associated to the material. Therefore the Urbach energy can be correlated to the passivation properties of H in a-Si:H (see next paragraph).

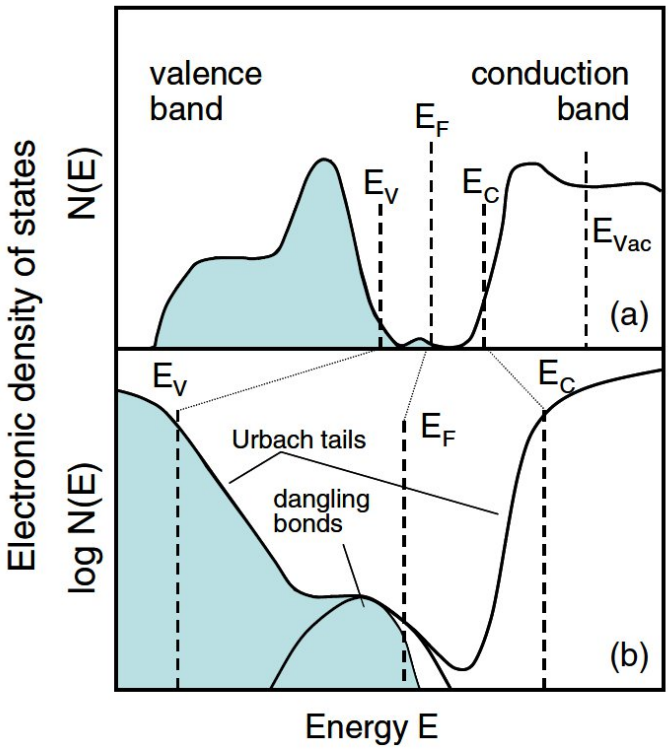

Figure 3.2: DOS of a-Si in linear (a) and logarithmic (b) plot [DWo12]

Until now only the DOS representation was considered because the real electronic structure, i.e. E vs $\vec{k}$ band dispersion, is difficult to be modelled for amorphous semiconductors. The absence of long-range order makes the Bloch theorem inapplicable, because crystalline momentum is undefined in this case [Pie72]: the lattice potential

looses its regular periodicity resulting in a permanent scattering of the electrons from one Bloch state to another. An interesting result of electronic simulation is reported in figure 3.3, where the band structure of a-Si is modelled using the Bethe lattice, that contains all possible tetrahedrally coordinated structures, and a spectrum of complexes energies [Kra72]. The solid lines report the real part of the energy and the shaded areas denote the regions with the double of the imaginary part centred around the real part: it can be seen that, in this model, for the maximum of the valence band the SRO is dominant, while the conduction band is more affected from the disorder potential. The order parameter is $\alpha = 0.05$ (see equation 3.2).

Although in the amorphous case there is no distinction between direct and indirect energy gap, it is possible to extrapolate a value of the gap, that is allowed due to the preservation of short-range order (tetrahedral coordination) [Pie72].

The optical properties of a-Si layers will be analysed in chapter 5.

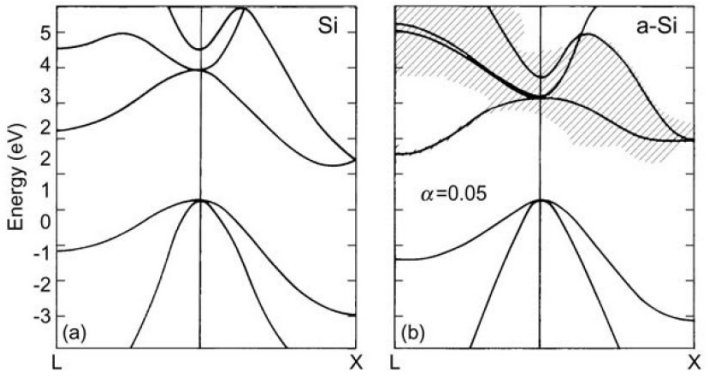

Figure 3.3: Band structure of c-Si and a-Si by [Kra72] and [Kol04]

3.1.3 Role of diffusing and passivating hydrogen

The specific layer studied in this work is a-Si:H, that means amorphous silicon passivated by incorporation of H (see also next chapter about PECVD). As mentioned in the previous chapter, the H saturates the Si dangling bonds in the amorphous structure, but especially at the interface of the stack c-Si/a-Si. The presence of H atoms reduces the density of states at the center of the gap and as well in the band tails from $10^{19}\ cm^{-3}$ (pure a-Si) to $10^{16}\ cm^{-3}$. Since the defects operate as charge recombination centres this improves the optoelectronic properties of the heterojunction.

The H content that can be found in a-Si:H layer is in the range $5 \div 30\%$, as reported in literature [Gas11], [Sme07]. The H also plays a key role in the Staebler-Wronski effect, that is the lifetime degradation of a-Si layers due to light exposure [Kol04], [Sta77]. There are many different historical models to explain this metastable phenomenon; one of the most favoured picture is that photo-excited electrons and holes recombine at weak Si-Si bond locations, and the non-radiative energy release is enough to break the bond and create new bulk defects. It takes 10^7 photons to create 1 DB. It was observed that this situation can be restored by the process of thermal annealing [Kol04], which causes the H inside the amorphous network to diffuse interstitially and recover the DB. Reactions involving Si, H and vacancies are easily activated, because, making a comparison between the amount of atoms and recombination centres, we can

observe that the density of SWE defects is around $10^{17}\ cm^{-3}$ that is a small fraction of $10^{23}\ cm^{-3}$ Si-Si bonds and $5 \times 10^{21}\ cm^{-3}$ Si-H bonds.

The hydrogen diffusion, despite the SWE, is crucial for all the passivation mechanism. Up to temperatures of 300 $°C$, the motion of H atoms can be activated. These are in a-Si interstitials, clustered or occurring as H_2 molecules. (For more info about the structural configuration of H in a-Si, see paragraph 5.1). This dynamic process can be described by a diffusion coefficient:

$$D_H = D_0 exp(-E_A/k_B T) \tag{3.4}$$

where E_A is the energy to activate the diffusion. However the real nature of this mechanism is still subject of scientific discussion.

3.2 Si-rich amorphous SiO_x:H and SiC_y:H

In this thesis amorphous SiO_x:H and SiC_y:H, with low incorporation of oxygen and carbon are studied. Although the density of silicon atoms is around 80 %, the formation of comparably few Si-O or Si-C bonds can cause distortions, voids in the amorphous network, affecting the structural, but also the electro-optical properties of amorphous silicon. From literature they are known to be more temperature stable and the higher optical band-gap leads to more photo-generated carriers in the absorber.

The table 3.1 shows the atomic and molecular properties of the Si-X bonds in the investigated layers:

Table 3.1: Values of atomic and molecular properties of a-SiX:H from [Wikipedia], [MSU]

Specie	**At. radius** Å	**El-negativity** eV	**Bond length** Å	**Bond energy** $kcal \cdot mol^{-1}$
Si	1.11	1.90	Si-Si : 2.35	52
H	0.31	2.20	Si-H : 1.48	75
O	0.66	3.44	Si-O : 1.62	110
C	0.70	2.55	Si-C : 1.87	76

It has to be noted that in this study the bonds O-H and C-H are assumed to be absent in the material: the low content of oxygen and carbon ($\langle 10$ %) allows to neglect them.

Due to the difference of the tabulated values, one can see that by increasing the density of the heteronuclear bonds, the disorder of the amorphous network increases. Thus epitaxial growth is less likely as observed by Fujiwara [Fuj07b]. The incorporation of O and C strongly depends on the deposition conditions and it is difficult to figure out: theoretical models were proposed with the standard *random bonding model* (RBM, see [Phi72] and [Efs92]) to simulate these non-crystalline alloys, using the same approach to simulate glassy materials. Figure 3.4 shows a model of the amorphous structure of a-SiX:H.

Anyway in our case the Si-rich a-Si alloys will not exhibit large variations, from the optimal properties of a-Si:H. The purpose is to increase the stability of the amorphous network when exposed to thermal solicitations. From the table above, the bond energy increases for Si-C and Si-O, hence the principal expectation is that an alloy Si-X constituting the passivation layer has a more compact structure than a-Si:H .

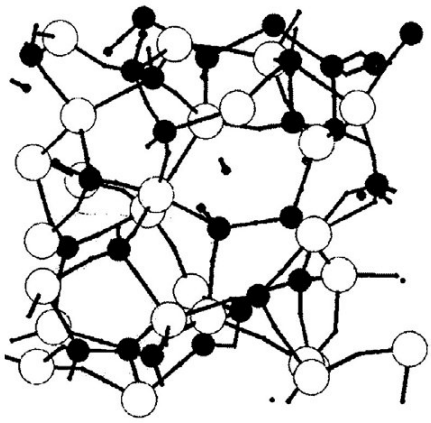

Figure 3.4: One possible amorphous silicon (white) and carbon (black) network with incorporated hydrogen (small black dots) a-SiC:H, from [Jan06]

Also the optical behaviour is influenced from the Ox and Cy. In the following picture the amorphous network can be interpreted as a molecule with a large number of atoms. The density of states is dependent on the highest occupied molecular orbital (HOMO) and the lowest unoccupied molecular orbital (LUMO); quantities correlated respectively to the valence band maximum and the conduction band minimum. It was observed ([Tom], [Suw11]) that the valence band of the final electronic structure is formed by the Si-Si localized bonding states, while the conduction band is formed by the (non-localized) anti-bonding states of Si-Si and Si-X (O or C) bonds: these last ones are found to have higher energies, therefore an increase in the energy gap is expected when incorporating oxygen and carbon in a-Si:H.

How the molecular orbitals are related to the valence and conduction bands is shown in figure 3.5.

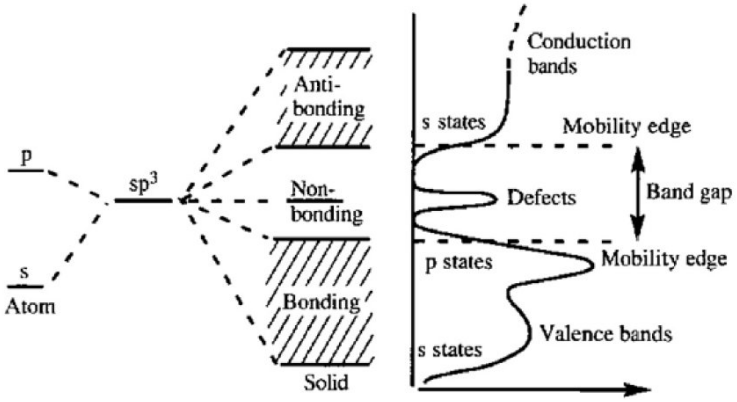

Figure 3.5: Molecular orbitals and schematic of the resulting density of states for hydrogenated amorphous silicon; from [Str91]

CHAPTER 4

Deposition Process

In this chapter the deposition process is exposed. At the beginning the cleaning of the wafer is outlined, than the PECVD reactor for a-Si growth is analysed in detail (physical mechanism and technical implementation). In addition the process parameters for this work are shown.

4.1 Wafer cleaning procedure

The c-Si wafer surface is continuously exposed to chemical contaminants and external particles adhesion that can degrade the deposition of the layers on top and the general electrical properties of the final structure. The wafer cleaning procedure is an established technique that started in 1950s for manufacturing integrated circuits (IC); the purpose of the chemical removal is not to attack the bulk structure.

A wet-chemical cleaning process widely used is the RCA Standard Clean [Rei08] that consists of two consecutively applied hot solutions (both at 65°C), 10 min each: SC-1 and SC-2.

The SC-1 solution consists of a mixture of H_2O:H_2O_2:NH_4OH with ranges from $5:1:1$ to $7:2:1$: this was designed to remove organic contaminants and elements of periodic group IB and IIB (especially metals). The SC-2 solution ranges from $6:1:1$ to $8:2:1$ parts by volume of H_2O:H_2O_2:HCl : this is needed to remove surface alkali residues and metal hydroxides [Rei08].

The air exposure affects the surface of the wafer by creating an oxide layer thick $\approx 1-1.5\ nm$ [Rei08]. For this reason the last process of the RCA clean is the HF-dip, that leaves the surface with silicon-hydrogen bonds (or H-terminated) and slows down the growth of native oxide [Yab86]. This treatment helps the deposition of a-Si:H and reduce significantly the density of surface dangling bonds [Ang08]. In this work the HF was 1 % diluted in water and the dip time was 120 s, enough to achieve a hydrophobic surface as an indicator of H-termination.

4.2 PECVD

The plasma enhanced chemical vapour deposition (PECVD) is a technique most commonly used to fabricate thin film solar cells based on a-Si:H and μc-Si:H. The use of plasma enables deposition reactions to take place at RT which would otherwise require 1000 °C or more. These reactors typically consist of two parallel plates for capacitively coupled plasmas (acting as electrodes), one on the bottom and one on the top of a vacuum chamber, where reactive gases are inserted (the precursors of the deposition). To obtain a-Si:H usually a mixture of H_2 and SiH_4 is used. The top plate is powered and the bottom plate, where the substrate for the deposition stands, is grounded. Exposing the electrodes to a RF power excitation frequency (13.56 MHz), a plasma burns inside: the accelerated electrons ($T \approx 10^5\ K,\ E \approx 20\ eV$) collide with gas molecules dissociating them in free radicals, atoms, positive and negative ions, and electrons ([Schu11], [Kus87]). This first step is dominated by electron kinetics and plasma chemistry. The created species ($Si_nH_m^{\pm}$) interact with the growing film surface. This is followed by the conversion of the surface growth into a bulk solid. For this change the hydrogen dynamics and the surface kinetics determine the process: different reactions occur as H elimination (coming from the HF dip), adsorption (physisorption or chemisorption, consists in diffusion of H by hopping), incorporation, interconnection (breaking of Si-Si bonds and H acting as substitutional) ([Rob00], [Mat04]). However, the conversion of the surface layer to the bulk does determine the final makeup of the amorphous network and thus drawing conclusions from deposition reactions conditions to final film is limited [Rob00]. Due to plasma damage [Dem12] or metal pastes, an annealing step is necessary after the amorphous silicon deposition, as it leads the layer to a relaxation of the disordered network towards equilibrium and improves the passivation [DWo08].

4.2.1 Deposition by *Clustertool System*

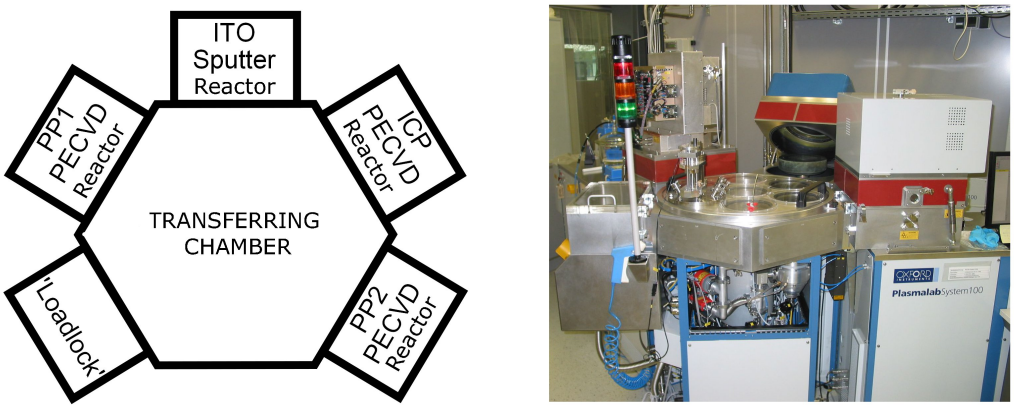

Figure 4.1: Sketch of Clustertool Chambers (a) and picture of the System (b)

In this work of thesis the deposition of a-Si:H and a-SiOx:H layers was made by the Clustertool *System* 100 *Pro* of *Oxford Instruments*. As shown in the pictures of

figure 4.1, the entire Clustertool contains different vacuum chambers for the deposition process. The Loadlock is the chamber that communicates with the external environment, where the substrate carrier and the wafer for the deposition can be placed. The transferring chamber has a roboter arm that moves the carrier wafer with the sample in the preferred deposition chamber. Chamber 1 and Camber 4 have the parallel plate (PP) used for amorphous Silicon, and both are connected with a capacitatively generator of 13.56 MHz. Chamber 1 is used for the deposition of the p doped layer (a-Si:H(p)) and Chamber 4 for the i/n layer (a-Si:H(i) or a-Si:H(n)). Chamber 2 is used for the sputtering of ITO and Chamber 3 has a reactor with a coupled inductive plasma (ICP) for i/n depositions. Each chamber is connected to a vacuum pump for the plasma process and a turbomolecular pump to achieve low pressure prior to the process start.

To initialize a deposition by the software (of Oxford Instruments) the creation of a recipe is necessary. In this the following parameters can be inserted: t time of deposition, P power frequency, H height of the table representing the lower electrode, p pressure of the chamber, T temperature of deposition (it is the temperature of the plate containing substrate and sample) and obviously the quantity of molecular gases (given in *sccm*) inserted for the process. For the doped layers B_2H_6 and PH_3 (mixed with H_2 gas) were used respectively for p and n. The time of deposition, for the expected thickness, was estimated experimentally by making different depositions at the beginning and extrapolating the slopes from the relation d(thickness) vs t (time). Before the start of the deposition, it was necessary to make a process of 30 min, a *Predeposition*, to coat the chamber walls and the carrier wafer, and avoid interactions with any residual metal particle in the chamber atmosphere.

Table 4.1: Standard deposition parameters of (i)a-SiO_x:H, n-doped and p-doped a-Si:H

Sample	$\mathbf{T}_{dep}$ °C	$\mathbf{H}_2$ *sccm*	$\mathbf{SiH}_4$ *sccm*	$\mathbf{CO}_2$ *sccm*	$\mathbf{B_2H_6}$ *sccm*	$\mathbf{P_2H_3}$ *sccm*	**p** *mtorr*	**P** *W*
i	200	30	2.8	0 ÷ 0.74	0	0	500	50
p	200	23	2.8	0	7.5	0	500	50
n	200	17	2.8	0	0	14	500	50

To incorporate oxygen the Chamber 4 was used and the molecular gas CO_2, variating the quantity between 0 to 0.74 *sccm*. In the table 4.1 the standard parameters used for the deposition of (i)a-SiO_x and (p) or (n) a-Si:H are shown.

Table 4.2: Standard deposition parameters of (i)a-SiC_y:H

Sample	$\mathbf{T}_{dep}$ °C	$\mathbf{H}_2$ *sccm*	$\mathbf{SiH}_4$ *sccm*	$\mathbf{CH}_4$ *sccm*	**p** *mtorr*	**P** *W*
i	300	100	30	0 ÷ 30	230	10

To incorporate carbon and deposit a-SiC:H layers an other deposition chamber was used: the system $AK400M$ of *Roth* and *Rau*, that has 2 different excitation sources for the plasma: the RF power (13.56 MHz) and a microwave excitation (2.45 GHz). The employed gas for carbon incorporation was CH_4, variating the quantity between 0 to 30 *sccm*. In the table 4.2 the standard parameters used for the deposition of (i)a-SiC_y:H are shown.

CHAPTER 5

Characterization Tools and Assumptions to Evaluate Data

In this chapter the characterization techniques used for this thesis are overviewed. In the first sections the analysis focuses on optical instruments (FT-IR and SE) and all the structural informations that can be detected by them. In the last, to observe the charge carriers' properties, the electrical tools, as QSSPC and SunsVoc, are outlined. At each instrument's paragraph, all the theoretical analysis and the assumptions made to evaluate the data and extrapolate the final conclusions are exposed.

5.1 Fourier transform infrared spectrosopy

5.1.1 Introduction

The Fourier transform infrared spectroscopy [Gri86] is an absorption technique that measures the vibrational properties of the atomic bonds inside the thin layer, with oscillation ranging in 10^{11}-10^{12} Hz. Characteristic modes can be identified depending on the freedom degrees, the symmetry or the anti-symmetry of the system that are activated from infrared energy.

The transmission spectrum of a sample shows the quantity of radiation that is absorbed by the investigated layer. The *Transmittance* is defined by:

$$T = \frac{I}{I_0} \tag{5.1}$$

Where I is the intensity transmitted through the sample and I_0 is the initial intensity of the IR source. In IR spectroscopy, the common unit of measurement is not the *wavelength* λ but the *wavenumber* ω, expressed in cm^{-1}. The output parameter generated by an FT-IR spectrometer is the *Absorbance*, defined by:

$$A = log\left(\frac{1}{T}\right) \tag{5.2}$$

Knowing the thickness d of the sample, allows to obtain the spectrum representing the absorption coefficient α:

$$\alpha = \frac{A \cdot ln(10)}{d} \tag{5.3}$$

The equation 5.3 is obtained from (5.2) and the Lambert-Beer law.

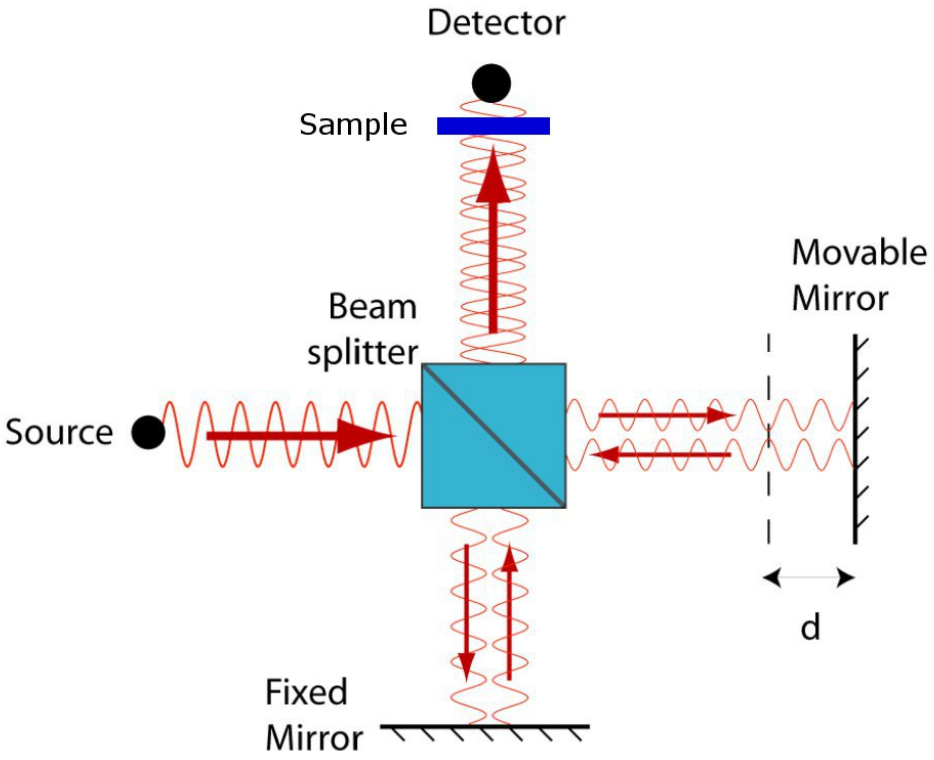

Figure 5.1: The Michelson interferometer.

The working principle of the FT-IR is based on the Michelson interferometer which is shown in the figure 5.1 the electromagnetic wave created by a polychromatic IR source propagates collimated to a beam-splitter, i.e. a special semi-reflecting plate. At this point the radiation is separated in two different orthogonal beams, that have the same intensity. The orthogonally reflected beam and the transmitted are then again reflected by, respectively, a fixed mirror and a translating mirror: going back to the beam splitter, the two beams re-conjunct and interfere. As the translating mirror creates the difference in the optical path of the partially transmitted beam, the two interfering waves have a phase shift (or retardation) that can cause a constructive or destructive interference (maxima or 0 intensity). The final output signal, captured by the detector, is called an *interferogram* and represents $I'(\delta)$, the intensity of the polychromatic wave function of the phase shift. Sometimes the interferogram is also reported in function of the time $I'(t)$, considering that each single phase shift is due to each single translation of the mirror at a time t. After detection, the signal can be elaborated by the software that calculates the Fourier Transformation of the overall interferogram, obtaining the intensity at each wavenumber $I(\omega)$:

$$I(\omega) = \int_{-\infty}^{+\infty} d\delta I'(\delta) cos(2\pi\omega\delta). \tag{5.4}$$

Capturing the signal with and without the sample (that is placed in front of the detector) one obtains $I(\omega)$ and $I_0(\omega)$, and calculates the Absorbance, as seen in the equations 5.1 and 5.2.

The Spectra of this work are obtained by the IFS-113v Fourier spectrometer from Bruker, that operates in a wavenumber range from 400 to 4000 cm^{-1} (the souce is a globar). The resolution of the entire setup can be between 0.03 and 8 cm^{-1}: for the experiments of this work it was set to 6 cm^{-1} for wafers having thickness $\approx$ 400 μm and 8 cm^{-1} for wafers having thickness $\approx$ 200 μm; these values were chosen in order to reduce the instrument artifacts and the so called *fringes*, resulting from multiple reflections within the c-Si substrate.

5.1.2 Data acquisition: corrections of the spectra

To analyse the spectra of amorphous Si thin films it was necessary to measure a reference sample, normally a pure FZ-silicon wafer, in order to subtract the absorbance of the substrate A_{sub} from the absorbance A_{tot} of the total system (substrate + thin film) using:

$$A_{a-Si} = A_{tot} - A_{sub} \tag{5.5}$$

obtaining the only contribution due to the few nanometers layer. Then, using equation 5.3 it is possible to calculate α_{a-Si}.

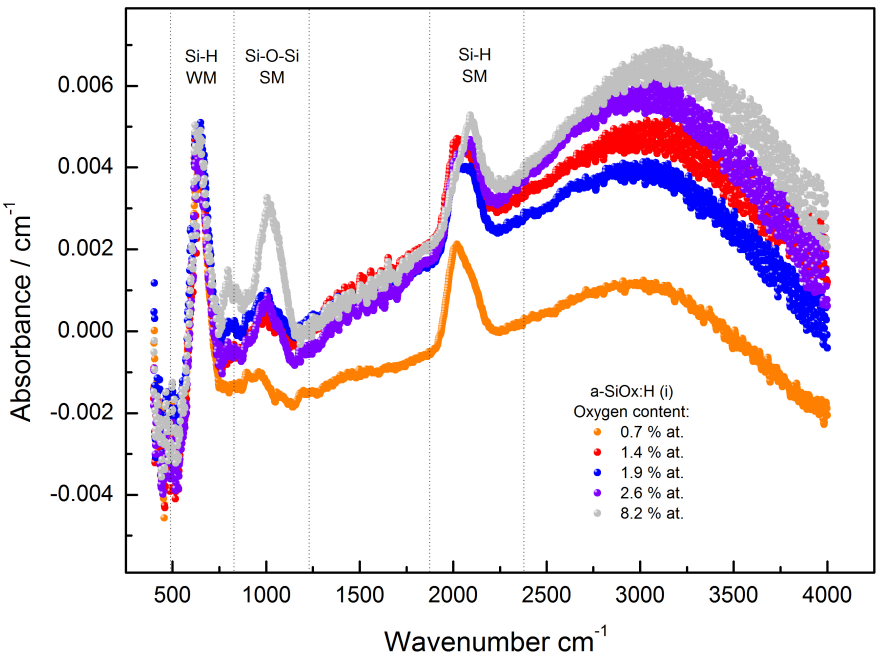

Figure 5.2: Acquired absorbance spectra of a-SiOx:H samples, with the abundant deviations of the baseline. The dots identify the regions of the vibrational modes

The subtraction of the substrate absorbance is made to remove the c-Si bands, mostly phonon vibrations. In the optimal case the refence sample has the same surface as the

a-Si samples and the same doping. If not, the output signal of the IR absorptions in the single a-Si layer still reveals baseline deviations mainly due to the superficial roughness of the measured thin film (high wavenumbers) and the higher doping of the sample substrate (low wavenumbers). The latter is normally visible with a doping starting from 10^{16} cm^{-3} or more.

The baseline deviations can be avoided by always using a reference coming from the same wafer as was done in this work.

Figure 5.2 shows the subtracted signals of several a-SiO_x:H samples: the spectra deflections are evident as the data points of the non-absorbing regions are some in the negative scale, others widely upper the 0.

Also, in the graph the typical three single vibrational modes are identified: Si-H *wagging mode*, Si-O-Si *bending mode* and Si-H *bending mode* (for further information the reader is referred to next paragraph 5.1.3. As it is impossible to simulate how the roughness and the other factors influence the overall spectrum, the way to adjust the data from this not irrelevant artifact is to work on the single vibrational peak: as showed in figure 5.3 the data of the specific range are subtracted by a line simulating the non-desired deflection (see the artifact and the correction, respectively red and black points in the mentioned graph). To avoid an arbitrary manipulation of the spectra, the signal background (region without absorption) is assumed to be always at the same plane position. This procedure was used for all the measurements of the a-Si samples.

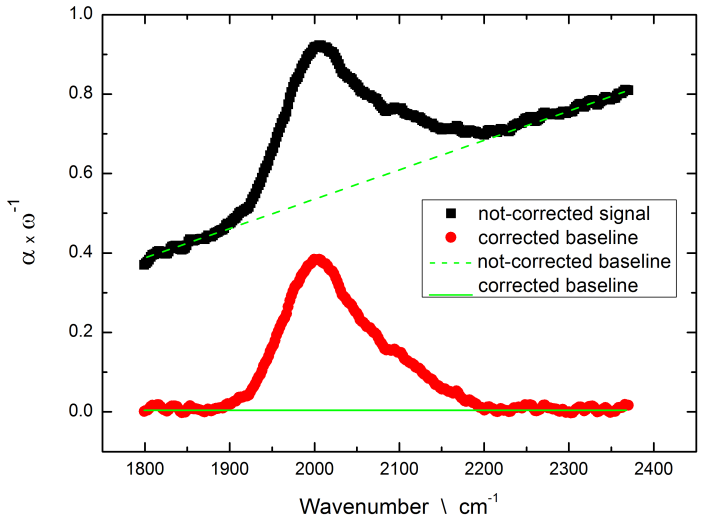

Figure 5.3: Example of a baseline correction.

Furthermore the multiple reflections other 2 important corrections were necessary to evaluate the spectra:

- the direct correction of the α points with the empirical factor

$$\alpha = \alpha_{a-Si}/(1.72 - K\omega d) \tag{5.6}$$

where d is the thickness of the sample and $K = 0.0011$. Due to the changes of optical path length, the refractive index and the thickness of the film, the

calculation of the absorption coefficient and the evaluation of the peaks with the BCC method (see paragraph 5.1.4) lead to underestimation or overestimation of the spectra, even when the baseline is determined correctly, and makes this correction necessary, as reported in [Lan92].

- the fringes correction: for samples having a thickness around 200 μm, the internal reflections cause many fringes in the acquired signal, reducing the resolution of the peaks; hence it was necessary to subtract them directly from the interferogram signal (the acquired data before the Fourier transformation) using the software Opus-NT from *Bruker Instruments*.

5.1.3 Vibrational modes and respective spectra of a-Si:H, a-SiOx:H and a-SiCy:H

The molecular vibrational modes are usually classified in two different types: *stretching modes*, when the IR absorption corresponds to a periodic variation of the interatomic distance, and *bending modes*, when the oscillation influences the bond angle.

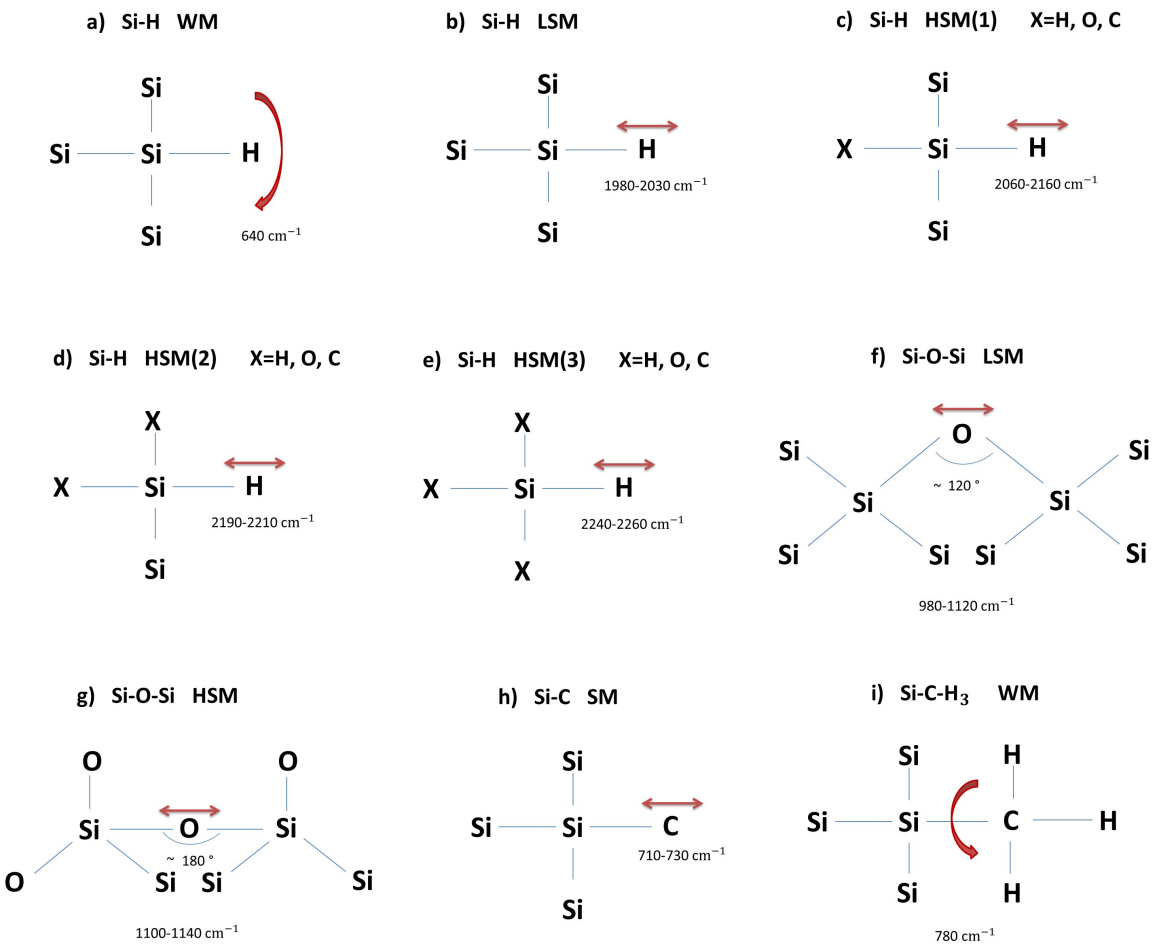

Figure 5.4: Vibrational modes of Si-H, Si-O-Si, Si-C

The *stretching mode* can be distinguished in symmetric (when the atoms oscillate simultaneously) or asymmetric (when the atoms oscillate alternately); the *bending* can oscillate in different reference planes: when oscillating in a parallel plane to the molecule it is called *scissoring*, if symmetric, or *rocking*, in the asymmetric case. When oscillating in an orthogonal plane of the molecule the modes are said, respectively *wagging* and *twisting*.

In a-Si:H the Si-H_x have three characteristic absorptions [Sme07]: the wagging mode at 640 cm^{-1}, a bending or scissors doublet at 840-890 cm^{-1} (identified as Si-H_2), and 4 stretching modes in the range 1980÷2260 cm^{-1}: the low stretching mode (LSM) at 1980-2030 cm^{-1} is assigned to Si-H vibrations in vacancies of the amorphous network; the three high stretching mode HSM_1, HSM_2, HSM_3 oscillate in the respective ranges 2060-2160 cm^{-1}, 2190-2210 cm^{-1} and 2240-260 cm^{-1}. These last ones are difficult to identify [Bro11]; the HSM can be assigned to di-hydrides or tri-hydrides oscillating in inner voids ($HSM_1 \rightarrow SiH_2$, HSM_2, $HSM_3 \rightarrow SiH_3$) as well as to a shift of the mono-hydride caused by some back-bonded O_x or C_y atom, that modify the electrical surrounding having higher electronegativity (see chapter 3).

The silicon-oxides bonds can be detected at 860-870 cm^{-1} identified as a bending mode, at 980-1020 cm^{-1} as the asymmetric stretching bonds Si-O-Si and at 1100-1140 cm^{-1} the HSM O_2-Si-O-Si-O_2 [Ifi10].

The silicon-carbide mode is observed at 720 cm^{-1} as stretching Si-C, at 780 cm^{-1} as Si-C-H_3 wagging, at 1200-1400 cm^{-1} as Si-C-H bending and at 2800-3000 cm^{-1} as Si-C-H_n stretching [Suw11]. In figure 5.4 the modes that are analysed for our samples are resumed.

Considering a-Si:H properties it can be said that if the LSM dominates the HSM this can be related to low defect density inside the layer. However, since our samples are a-Si alloys, this can not be always observed as there are frequency shifts due to theatomic surrounding rather than a passivation of lower quality.

5.1.4 Assumptions for data evaluation

a. Application of the BCC method

The absorption peaks of the FT-IR spectra are a measure of N_ω, the volume density of the oscillating bonds in the atomic layer. The peak center ω_0 identifies the activated mode. Brodsky, Cardona and Cuomo [BCC77] developed a theory (known as *BCC method*) to quantify the proportionality between N_ω and I_{ω_0}, the integral of the studied peak that is given by:

$$I_{\omega_0} = \int \frac{\alpha(\omega)}{\omega} d\omega. \tag{5.7}$$

Considering a system with a dilute assembly of harmonic oscillators in the amorphous Si network, that consist of two atoms with effective charge $\pm e^*$ and reduced mass μ, in

the same way as in a Lorentz oscillator (see next section 5.2.3 about optical models), the dielectric function in the IR band vibration, can be written as:

$$\Delta\epsilon = \frac{4\pi N_\omega e^{*2}/\mu}{\omega_0^2 - \omega^2 - i\gamma\omega} \tag{5.8}$$

where γ is the damping factor of the oscillation. Integrating $\omega\Delta\epsilon$ over the absorption band of interest and applying the quantum-mechanic sum rule one obtains the final formula:

$$N_\omega = \frac{\mu}{2\pi^2 e^{*2}} \int \omega Im\Delta\epsilon d\omega = C_{\omega_0} \cdot I_{\omega_0} \quad \text{with} \quad C_{\omega_0} = \frac{cn_\infty \mu\omega_0}{2\pi^2 e^{*2}} \quad . \tag{5.9}$$

In the proportionality constant C_{ω_0}, usually given in cm^{-2}, c is the speed of the light and n_∞ is the *static refractive index*, i.e. the refractive index in the IR range ($n_\infty = n_{IR}$ when $\lambda \to \infty$), that is assumed to be frequency independent (as we are in a low energies range, the system has a constant dispersion that means a constant refractive index).

The investigated IR bands and the absorption constants used in this work are referred to: the *Si-H* wagging mode (WM), the *Si-H* low stretching mode (LSM), the *X-Si-H*, X_2-*Si-H*, X_3-*Si-H* high stretching modes (respectively HSM_1, HSM_2 and HSM_3, with $X = H$ or O) and the *Si-O-Si* stretching mode (see the previous paragraph). They were calculated theoretically and calibrated experimentally (with instruments like SIMS) by many authors: see for more informations [Car83], [Car80], [Pved], [Luc78], [Luc83], [Luc86], [Ino95], [Ein12] and [Bro11]. The table 5.1 shows and lists the global results obtained by this procedures: it can be observed that C_{ω_0} has a complex dependence due to the variations of the refractive index, the effective charge and the peak frequency; so its value is found to be in a certain range.

Table 5.1: Values of absorption constant C_{ω_0} at any specific mode

$\mathbf{C_{\omega_0}}$	**Mode**	**Position** / cm^{-1}	**Range** / cm^{-2}	**Reference**
C_{Si-H}	WM	≈ 640	$(1.6 \div 2.1) \times 10^{19}$	[Sme07]
C_{Si-H}	LSM	$1980 \div 2030$	$(2.2 \div 14.0) \times 10^{19}$	[Sme07]
C_{X-Si-H}	HSM(1)	$2060 \div 2160$	$(9.1 \div 14.0) \times 10^{19}$	[Sme07]
C_{X_2-Si-H}	HSM(2)	$2190 \div 2210$	$(9.1 \div 14.0) \times 10^{19}$	[Bro11]
C_{X_3-Si-H}	HSM(3)	$2240 \div 2260$	$(9.1 \div 14.0) \times 10^{19}$	[Bro11]
$C_{Si-O-Si}$	SM	$1000 \div 1200$	$(1.2 \div 1.6) \times 10^{19}$	[Ino95], [Ein12]
C_{Si-C}	SM	$710 \div 730$	$(2.1 \div 3.0) \times 10^{19}$	[Har10], [vSw94]

In this work the C_{ω_0} was directly calculated for the *Si-H* modes, as done by Smets in [Sme07], taking the formula from equation 5.9: ω_0 was obtained from the deconvolution of the spectra; for n_∞ the last point measured by the spectroscopic ellipsometer at

$\lambda = 9945.6$ Å (or at $\omega = 10054.7\ cm^{-1}$) was taken; the effective charge of the dipole *Si-H* was assumed constant and calculated by the Sanderson's bonding model with the values of the partial charge δ_{Si} and δ_H by [Ino95], [Cus94]:

$$e^* = 2(\delta_{Si} - \delta_H) = 0.384\ . \tag{5.10}$$

Unfortunately, for Si-O and Si-C bonds it was not possible to calculate the C_{ω_0}, as the electronegativity of Ox (or Cy) influences the respective effective charges, adding more fluctuations on the electrical surrounding of the molecules. For this reason, the values of the absorption constants were taken from literature: $C_{Si-O-Si} = 1.48 \times 10^{19}$ and $C_{Si-C} = 2.13 \times 10^{19}$ from [Ino95] and [Har10], respectively.

b. Sub-stoichiometric contents calculation

The bonds density, obtained by FT-IR spectra, can be considered as a measure of the atomic density, establishing:

$$N_{Si-H} = N_H\ , \qquad N_{Si-O-Si} = N_O \text{ and } \qquad N_{Si-C} = N_C\ . \tag{5.11}$$

These relations are valid just in the case if only one kind of vibrational mode is considered, i.e. it is possible to identify an atomic density in the layer when the studied bonds are activated at one specific infrared energy. For example, as observed in [Sme07], the following relationship holds:

$$N_H(\text{WM}) = N_H(\text{LSM}) + N_H(\text{HSM}) \tag{5.12}$$

The aim of the FT-IR analysis is to obtain structural informations, especially about the atomic concentration of the studied layers, that are: a-Si:H, a-SiOx:H and a-SiCy:H. The percentages of the atomic species can be obtained using:

$$C_H = \frac{N_H}{N_H + N_{Si} + N_X} \qquad C_{Si} = \frac{N_{Si}}{N_H + N_{Si} + N_X} \qquad C_X = \frac{N_X}{N_H + N_{Si} + N_X} \tag{5.13}$$

where $X = O, C$. In this work Si-rich a-SiX:H layers are studied, so the silicon is the dominant specie. However infrared spectroscopy does not detect homo-atomic bonds, as Si-Si, thereby the N_{Si} necessary for the equation 5.13 cannot be obtained experimentally.

In literature many authors assume $N_{Si} = 5 \times 10^{22}\ cm^{-3}$, as in pure c-Si (see [Ein12]). Although the normal amorphous silicon was observed [Cus94] to be slightly (1.8%) less dense than the crystalline, the abundant dilution in H_2 and the incorporation of few oxygen and carbon atoms during the PECVD process reduces the silicon percentage by 15-25%. To address this aspect and to be able to calculate the sub-stoichiometric concentrations of all the species, the Lorentz-Lorenz equation was used [Lort880], [Lor880]:

$$\frac{n_\infty^2 - 1}{n_\infty^2 + 2} = \frac{4\pi}{3} \sum_i N_{os(i)} \alpha_{p(i)} \tag{5.14}$$

This equation relates the static refractive index with the sum of N_{os} individual oscillators (or molecules) having a specific polarizability α_p, that is also assumed constant

in all the IR range. Equation 5.14 can be adapted to the a-SiX:H layer, using the analogous procedure of [vdH91]:

$$\frac{n_\infty^2 - 1}{n_\infty^2 + 2} = \frac{4\pi}{3}(N_{Si-Si}\alpha_{Si-Si} + N_{Si-H}\alpha_{Si-H} + N_{Si-X}\alpha_{Si-X}) \tag{5.15}$$

In this equation the relationship of equation 5.11 is still valid, hence N_H and N_O are given by spectroscopic analysis. N_C is taken from SIMS measurements of the PhD thesis of Suwito [Suw11]. The $N_{Si-Si} \approx 2 \cdot N_{Si}$. The polarizability of the Si-Si bond can be calculated using equation 5.14 for amorphous Si, with $n_\infty = 3.6$ and $N_{Si} = 5 \times 10^{22}\ cm^{-3}$:

$$\alpha_{Si-Si} = 1.91 \times 10^{-24}\ cm^3\ . \tag{5.16}$$

The bond polarizability of Si-H oscillator is calculated from the polarizability of the SiH_4 molecule [vdH91]:

$$\alpha_{Si-H} = \frac{1}{4}\alpha_{SiH_4} = 1.36 \times 10^{-24}\ cm^3\ . \tag{5.17}$$

Applying a similar procedure, the polarizability of Si-O-Si bonds is deduced calculating the L-L relation for the $a\text{-}SiO_2$: in this material there is only one kind of oscillators (no Si-Si bonds exist [Enig]), therefore $N_{O-Si-O} = N_{Si(in\ a-SiO_2)} = 2.5 \times 10^{22}\ cm^{-3}$ and the $n_\infty = 1.47$ (value taken at $\lambda = 800\ nm$) [Ino95]. Inserting all the values in eq. 5.15 it can be obtained:

$$\alpha_{Si-O} = \frac{1}{2}\alpha_{SiO_2} = 1.33 \times 10^{-24}\ cm^3\ . \tag{5.18}$$

In the same way the polarizability of Si-C was calculated considering a pure silicon Carbide material. Knowing the refractive index $n_\infty^{SiC} = 2.55$, the molecular mass density $\rho_{SiC} = 3.21\ g \cdot cm^{-3}$ and the molecular mass $m_{SiC} = 40.097\ g/mol$ one can arrive to the molecular density N_{SiC} and hence to the bond density $N_{Si-C} = 2 \cdot N_{SiC}$. Therefore, applying the L-L relation (eq. 5.15) to the SiC, the polarizability can be achieved:

$$\alpha_{Si-C} = 1.60 \times 10^{-24}\ cm^3\ . \tag{5.19}$$

Procured all the parameters, equation 5.15 can be solved in function of N_{Si-Si}. As mentioned above it is possible to write

$$N_{Si} = \frac{N_{Si-Si}}{2} \tag{5.20}$$

because, considering the unit cell of the diamond lattice of Si crystal, represented in figure 5.5, there is one Si atom at the centre and 4 atoms at the edges (each one of these counts as $\frac{1}{4}$ because is shared by other three atoms external to the unit cell), hence the number of total atoms is

$$Num_{Si}^{unit-cell} = 1 + 4 \times \frac{1}{4} = 2 \tag{5.21}$$

while the bonds of the tetrahedral configuration (SRO) are $Num_{Si-Si}^{unit-cell} = 4$. The same procedure can be done with the densities. At this point the estimation of the atomic contents in the layer results possible.

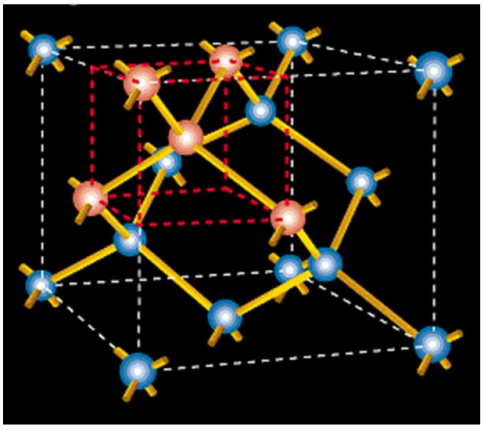

Figure 5.5: In blue the diamond lattice of Si crystal. In red the unit cell.

As shown in [vdH91], the density of Si-Si bonds can contain 1 or 2 terms that reduce the silicon incorporation. In our sample it could be written:

$$N_{Si-Si} = 2 \cdot (N_{cSi} - \delta N_H - \gamma N_X) \tag{5.22}$$

where the gamma and delta represent the incorporation parameters of H and X (O or C), respectively; they cause a lower density of Si in a-SiX:H, and show if the specific incorporation occurs in a mono-vacancy, in a di-vacancy or in a tri-vacancy respectively in the cases when γ (or δ) $= \frac{1}{4}, \frac{2}{6}, \frac{3}{8}$.

A last note: since the density calculated for a-Si is lower than the one assumed for c-Si by most authors, the resulting atomic percentage results higher than reported by others for the same content.

c. Voids content estimation

Following the considerations made by Smets (see [Sme07]), the density of Si-rich ($N_{Si} > 80\%$) a-Si:H films is mostly determined from the silicon atoms: therefore it is possible to consider the reduced silicon incorporation (due to hydrogen, and in alloys due to oxygen or carbon - i.e. other atomic species during the layer growth) as an estimation of the voids content inside the amorphous structure. Looking at the lengths and the energies of Si-X bonds in table 3.1, it seems reliable to make this assumption, as the deposition of an alloy system creates inevitably distortions in the final structure.

In the present work the N_{Si} in a-Si is calculated using the Lorentz-Lorenz relation from eq. 5.15 combined with eq. 5.20: as already mentioned, for the solution of this expression the N_H, N_O (or N_C) coming from the FT-IR spectra were used (the results will be shown in chapter 6). Considering the standard c-Si density $N_{Si}^{c-Si} = 5.0 \times 10^{22}\ cm^{-3}$, it is possible to estimate the voids concentration of the studied a-Si alloys, with this calculated normalizing the reduced density in the amorphous layer:

$$\#\text{ of internal voids} \propto 1 - \frac{N_{Si}}{N_{Si}^{cSi}} = 1 - \frac{\rho}{\rho_{cSi}} \tag{5.23}$$

where N_{Si} and ρ are respectively the Si atomic density and the Si mass density in the amorphous layer, while N_{Si}^{cSi} and ρ_{cSi} are the corresponding Si atomic density and the Si mass density in the crystalline layer.

5.2 Spectral ellipsometry

5.2.1 Introduction

Spectral ellipsometry [Tom05],[Fuj07] is an optical measurement technique used to determine indirectly the thickness and the optical constants of thin layers. This spectroscopic method characterizes the changes in a polychromatic light with a known state of polarization (usually circularly polarized) that becomes elliptically polarized after the reflection on a sample.

Using a source from the visible/ultraviolet region to microwaves or radio waves, the matter behaves as a continuum. The passage of a light wave in a medium is linked to the induced motion of the electric charges of electrons and atomic nuclei, constituting macroscopic electric currents: so the light wave can be described with the vector of its electric-field intensity, $\vec{E}(\vec{r},t)$, analysing the spatial and the temporal dependence in a uniform, isotropic medium by the wave equation

$$\left[\nabla^2 - \frac{\epsilon(\omega)}{c^2}\frac{\partial^2}{\partial t^2}\right]\vec{E}(\vec{r},t) = 0, \tag{5.24}$$

where ω is the angular frequency of the light wave, c is the light velocity in vacuum and $\epsilon(\omega) = \epsilon_1 + i\epsilon_2$ is the complex dielectric function. The real component of $\epsilon(\omega)$, $\epsilon_1(\omega)$, quantifies the ionic and the electronic polarizability of the solid exposed to an external electric field: this phenomenon causes the dispersion of the light wave in the medium. The imaginary component $\epsilon_2(\omega)$ reveals, in the case of not transparent materials, the attenuation of the light intensity when the radiation provokes energetic transitions (ionic in the IR, electronic in the visible-UV) and its spectra show absorption peaks. This quantity will be explained in detail in paragraph 5.2.3.

A polarized wave has the peculiarity that the electric field exerted on charges or dipoles in matter is oriented along preferential directions. The elliptic polarization is the most general polarization state of a monochromatic light wave and from a quantum mechanical point of view it can be seen as a superposition of two linearly polarized waves. The relative phase δ of the vibrations along the x- and y-direction indicates the particular state of polarization: when $\delta = 0$ or $\delta = \pi$ it is a linear polarization, and when $\delta = \pm\frac{\pi}{2}$ it is a circular polarization. The quantum states of polarization are described by Jones and Stokes matricial calculations [Jon41], [Fuj07].

5.2.2 Instrumental apparatus and ellipsometry principles

The ellipsometer used for this thesis is the Wollam M-2000. The system configuration is shown in figure 5.6a, it is a typical polarizer-compensator-sample-analyzer (PCSA) configuration. The light source is a quartz tungsten halogen lamp. The beam passes through a fixed polariser (a calcite Glan-Taylor polariser) and a continuously rotating compensator (a retarder) before hitting the sample: so the incident beam results as two linearly polarized beams (s-wave and p-wave) with a relative phase difference δ_1. The outgoing reflected beams are polarized by the fixed analyzer and result with a phase difference δ_2. The detector is a back-thinned silicon CCD array.

The ellipsometer measures two quantities, in the energies range $1.26 \div 5.05\ eV$:

- the phase difference induced by the reflection: $\Delta = \delta_1 - \delta_2\ [0 \div 360°]$
- the ratio of the amplitude diminutions, calculated from the squared Fresnel reflection coefficients of the parallel and the perpendicular waves, $R_s = |r_s|^2$ and $R_p = |r_p|^2$: $tan(\Psi) = \dfrac{|R_p|}{|R_s|}\ [0 \div 90°]$.

These two quantities are connected by the fundamental equation of ellipsometry:

$$\frac{R_p}{R_s} = \rho = tan(\psi)e^{j\Delta} \tag{5.25}$$

The figure 5.6(b) show the angle ψ between the s-waves and the p-waves, and the respective fresnel coefficients $r_{p,s}$.

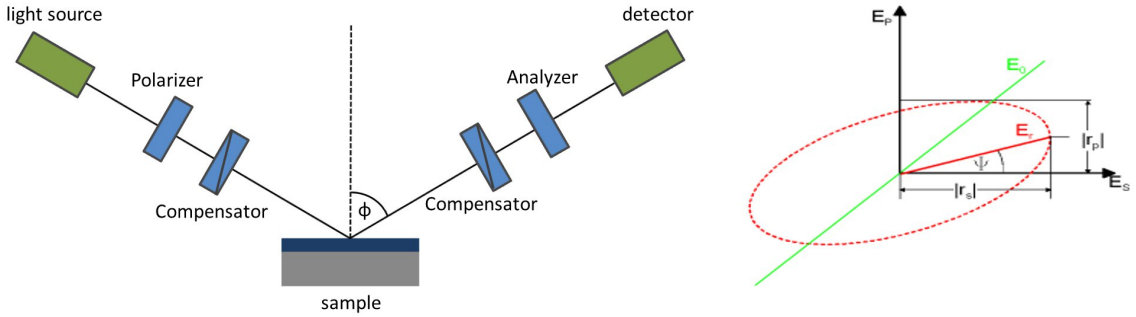

Figure 5.6: (a) Spectroscopic ellipsometer setup; (b) elliptical polarization of p- and s-waves, note the angle ψ and the coefficients $|r_s|$ and $|r_p|$, from [Mei10]

As mentioned in the introduction, the ellipsometer gives informations on the optical quantities of the investigated material. From the Ψ and Δ values a dielectric function can be calculated from an optical model that assumes a perfectly flat substrate with infinite thickness [Fuj07]. This is the so called *pseudo*dielectric function:

$$\langle\epsilon\rangle = \langle\epsilon_1\rangle + i \cdot \langle\epsilon_2\rangle = \langle N\rangle = \epsilon_a \left[\left(\frac{1-\rho}{1+\rho} \right)^2 sin^2\Phi_a + cos^2\Phi_a \right] tan^2\Phi_a \tag{5.26}$$

where $\langle N\rangle$ represents the pseudocomplex refractive index, ϵ_a is the ambirent dielectric function (≈ 1 in the air), Φ_a is the azimuthal incidence angle. It has to be pointed out that $\langle\epsilon\rangle$ is a derived, not measured quantity, hence the terminology *pseudo*dielectric function [Asp83].

5.2.3 Optical models

The software used to evaluate data is WVase32. Anyway the data from a SE measurement is not useful by itself, but must be compared and fitted with an appropriate model in order to extract the informations about the thickness and the optical functions of the layer. There are several different models depending on the material, the transparency and the absorbing regions of the electromagnetic spectrum [Fuj07].

a. The Kramers-Kronig relation

Actually the Kramers-Kronig relation is not an effective model, but it is implemented in several optical theories. It is used to correlate the real and the imaginary part of a (partially analytic) complex function. In terms of optics it can allow to calculate the dispersion parameter of the light (n) from absorption measurements (k) and viceversa. Here the real part of the dielectric function ϵ_1, expressed with the imaginary component ϵ_2 [Jel94] is:

$$\epsilon_1 = \epsilon_1(\infty) + \frac{2}{\pi} P \int_{Eg}^{\infty} \frac{\xi \epsilon_2(\xi)}{\xi^2 - E^2} d\xi \tag{5.27}$$

Where ϵ_∞ is the real part of the dielectric constant at infinity, P the Cauchy principal value.

b. The Lorentz Model

One of the oldest dielectric function models [Tom05] is the Lorentz model: it is based on the polarization of an electron induced from the AC electric field of an electromagnetic wave ($E = E_0 exp(i\omega t)$). The classical assumption is that the electron oscillates (as a spring attached to the nucleus) in a viscous fluid, with Newton's second law:

$$m_e \frac{d^2x}{dt^2} = -m_e \Gamma \frac{dx}{dt} - m_e \omega_0^2 x - eE_0 exp(i\omega t) \tag{5.28}$$

where m_e is the electron mass, e is the electron charge, Γ is the damping coefficient of the electron cloud motion, due to the viscous force, and ω_0 is the resonant frequency of the spring. Calculating the polarization $P = -eN_e x(t)$ with the electron density N_e and solving the equation 5.28, it is possible to obtain [Fuj07]

$$\epsilon = 1 + \frac{e^2 N_e}{\epsilon_0 m_e} \frac{1}{(\omega_0^2 - \omega^2) + i\Gamma\omega} \tag{5.29}$$

It is interesting to note that the dissipating factor Γ represents radiated energy losses for free atoms [Woo72].

c. The Tauc-Lorentz model

The Tauc-Lorentz model was proposed by Jellison and Modine [Jel94] to investigate the imaginary dielectric function in amorphous semiconductors. It is a combination of the Lorentz model with the Tauc expression for the region above the band gap [Tau66], which assumes parabolic energy bands and and a constant momentum matrix element:

$$\epsilon_2 = A_{Tauc}(E - E_g)^2 / E^2 \tag{5.30}$$

where A_{Tauc} is a fitting parameter. Multiplying equation 5.30 with the imaginary part of eq. 5.29, the final result is:

$$\epsilon_2(E) = \left[\frac{A E_0 \Gamma (E - E_g)^2}{(E^2 - E_0^2)^2 + \Gamma^2 E^2} \cdot \frac{1}{E} \right], \qquad E > E_g, \tag{5.31}$$

$$\epsilon_2(E) = 0 \qquad E \leq E_g \tag{5.32}$$

Normally the Lorentz model gives the shapes of ϵ_2 peaks completely symmetric, while the Tauc-Lorentz, as in this case, results in asymmetric shapes.

The real part ϵ_1 is calculated by the Kramers-Kronig relations. It has to be noticed that this model just works when there are no defects or intraband absorptions, that can cause the dielectric function to have non-zero values below the E_g.

d. The Cody-Lorentz model

Alternatives (or corrections) to the Tauc-Lorentz model were proposed in the last years [Fer02]. One really notable was shown by Cody *et al.* [Cod84] about a-Si:H, demonstrating that in this case the interband absorption needs a model with parabolic bands and a constant dipole matrix element (instead of a momentum matrix, as considered by Tauc). Furthermore, under the energy gap there is an exponential decrease, the Urbach Tail, due to the structural disorder of amorphous silicon (see chapter 3). The Cody-Lorentz (CL) considers also this aspect:

$$\epsilon_2(E) = \frac{(E-E_g)^2}{E^2}\frac{AE_0\Gamma(E-E_g)^2}{(E^2-E_0^2)^2+\Gamma^2E^2}\cdot\frac{1}{E}, \qquad E > E_g, \tag{5.33}$$

$$\epsilon_2(E) = \frac{E_1}{E}\exp\left[\frac{(E-E_t)}{E_U}\right] \qquad 0 \leq E \leq E_g \tag{5.34}$$

where E_U is the Urbach energy, E_t defines the transition energy between the Urbach and CL absorption range, E_1 is a continuity parameter of ϵ_2. In this case as well the real part of ϵ is determined by the Kramers-Kronig transformation.

5.2.4 Dielectric function: long range disorder and crystallinity of a-SiX:H

As explained above, from the ellipsometer it is possible to extrapolate the thickness of the layers, that helps to calibrate the deposition process and to reproduce homogeneous samples, and also the pseudo-dielectric function of the specific material. In our case the fitting of $\langle\epsilon\rangle$ allowed to investigate structural properties of the a-SiX:H layers. The used models are the Tauc-Lorentz and the Cody-Lorentz.

The imaginary dielectric function is intimately correlated to the lattice structure of any material. Considering at the beginning the crystalline silicon, as was observed by different authors (see [Fuj07], [Lau87]), the ϵ_2 reveals the absorption peaks of the direct energy gap transitions corresponding to the so called *joint states*.

Figure 5.7(a) represents the electronic structure of c-Si in the most common $\vec{K}$ directions of the *Brillouin Zone* $\left(\Gamma\left[k=(0,0,0)\right], X\left[k=\frac{2\pi}{a}(1,0,0)\right], L\left[k=\frac{\pi}{a}(1,1,1)\right]\right)$; all the direct transitions in the critical points are plotted. Each energetic absorption corresponds to a respective structural orientations, inside the diamond lattice of c-Si. In figure 5.7(b) it is shown how all these peaks contribute to the final imaginary dielectric function. These absorptions represent the long range order (LRO) inside the material, because they manifest the presence of the specific crystalline directions. Furthermore, the height of these peaks represent the density of the absorbing oscillators, as far as in the case of the molecular bonds in the FT-IR spectra: but here the oscillators are

the electrons that, excited from the UV/visible light, transit to the conduction band under particular restrictions, due to the Bloch theorem, of allowed and not allowed energies at each wave vector position ($\vec{K}$). The broadness of ϵ_2 peaks is related to the statistical distribution of these oscillators and is determined by the lorentzian Γ factor: this parameter, as seen above, is related to the energy losses in the atomic surrounding; the higher the dissipation, the higher is the distribution of the absorption at different energies, indicating deviations from the homogeneous crystalline orientations.

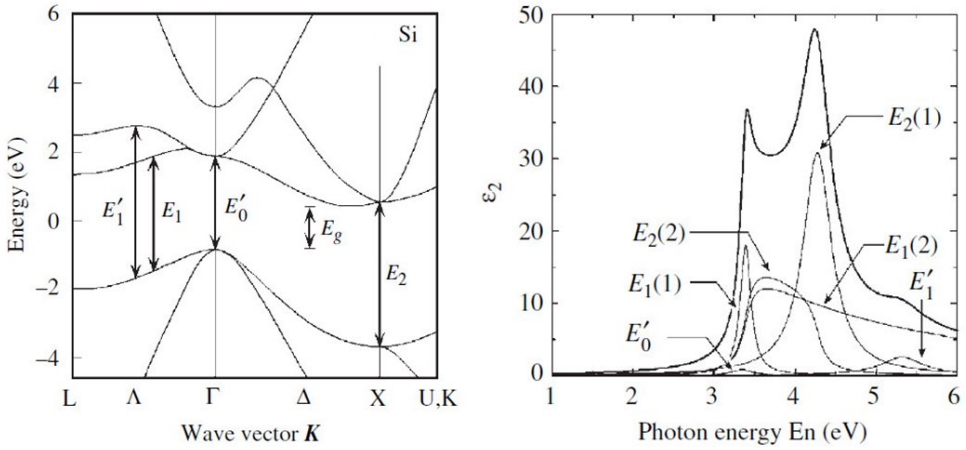

Figure 5.7: (a) Electronic structure of c-Si, with represented the direct band gap transitions; (b) imaginary dielectric function of c-Si, from [Fuj07]

With these reasons, the ϵ_2 peaks were abundantly used in literature to observe the density of crystallites and to evaluate samples of poly-Si or μ-Si and recently also in a-Si:H ([Pie72], [Bor97], [Col00], [Lev03], [Wak98]).

Considering now the amorphous silicon, the lack of LRO determines a significantly smaller absorption peak and an increased broadness of the imaginary dielectric function: adopting the same criterion, the height of the ϵ_2 peak can be related to the amount of the LRO, as an indicator of the crystalline (or amorphous) state of the layers. As was seen in literature, the epitaxial growth of a-Si:H, or the presence of crystalline grains, affects the electronic properties of this materials ([Kon07]). Hence the shape of the dielectric function can help to detect the crystalline amount in the PECVD deposited layers.

An other way to evaluate the structural disorder of aSi:H layers is to extract the Urbach energy, recurring to the CL model. Below the optical band gap, the absorption coefficient can be written as

$$\alpha = \alpha_0 exp\left(\frac{E - E_g}{E_U}\right). \tag{5.35}$$

Fitting this exponential decrease to 0 allows to obtain the Urbach parameter that also defines the slope of the electronic band tails (see paragraph 3.1.2) and hence the amount of long range disorder (LRD).

5.2.5 Data analyses: fit procedure and mean standard error

To analyse the experimental results it is necessary to create a multi-layer model, and at each layer are assigned n and k values that come from the optical model (see previous paragraphs) implemented for that material. For our samples, a standard three-layers model was used to estimate the thickness of the a-Si thin films, as shown in the picture 5.8(a): at the bottom the c-Si *substrate* with $d_{sub} \approx 200 \div 400\ \mu m$, and known n and k values; at the center the *bulk* representing the studied a-SiX:H layer with the optical parameters to determine; at the top the *surface* layer with $d_{surf} < 1\ nm$ and $k = 0$ (in the entire spectral range), needed to improve the fitting procedure. For this last one the typical used layer is a roughness model or an oxide model: anyway in our samples, as most of the measurements were executed at ambient air (that means easy oxidation of the a-Si surface), the SiO_2 layer gave the best fit results and therefore was assumed for the global ellipsometric analysis.

To obtain the optical constants the three layers-model was improved inserting an interface between the *substrate* and the *bulk*, see figure 5.8(b): the interface is realized with the *intermix* model of the WVase software, that consists of 50% of the layer below and 50% of the one on the top. The interface layer gives a better fit and it is useful to observe, in case of annealing experiments, the thermally induced a-Si crystallization between amorphous bulk and crystalline substrate [Los01].

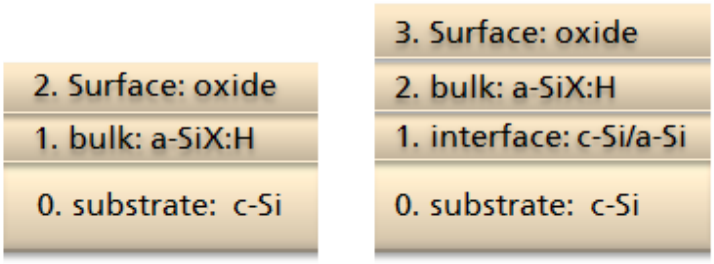

Figure 5.8: (a) three-layers model adopted for a-SiX:H samples; (b) insertion of the *interface* layer

The model just described was mostly used to evaluate samples with just (i)a-SiX:H layer. To analyse the stack (p)a-Si:H / (i)a-SiX:H / c-Si the same model with 2 equal *bulks* was applied, assuming that the intrinsic has $d_{(i)aSi} = 15\ nm$, the standard thickness of our samples.

The parameter that defines the goodness of a fit is the *mean standard error* (MSE), defined as:

$$MSE = \sqrt{\frac{1}{2N - M} + \sum_{i=1}^{n}[(\frac{\Psi_i^{mod} - \Psi_i^{exp}}{\sigma_{\Psi,i}^{exp}}) + (\frac{\Delta_i^{mod} - \Delta_i^{exp}}{\sigma_{\Delta,i}^{exp}})]} \tag{5.36}$$

where N is the number of (Ψ,Δ) pairs, M is number of variable parameters in the model and σ_i is the standard deviation on each experimental data point. The minimization of this quantity corresponds to the best similarity between model-generated values and experimental data.

5.3 Quasi steady-state photoconductance

5.3.1 Introduction

The quasi steady-state photoconductance [Sin96] is a measurement technique that quantifies the excess minority charges Δn produced in a semiconductor (or heterojunction, as in our case) and observes their recombination rate and therefore their lifetime (see equation 1.9) .

The time-dependency of the excess charge can be studied using the continuity equation:

$$\frac{\partial \Delta n(x,t)}{\partial t} = g_{ph}(x,t) - \frac{\Delta n(x,t)}{\tau_b(\Delta n)} + D_n \frac{\partial^2 \Delta n(x,t)}{\partial x^2} \tag{5.37}$$

where the excess charge density is written as a function of the time t and the distance x from the illuminated surface, g_{ph} is the photo-generation rate, τ_b is the bulk lifetime of the sample and D_n is the charge diffusion constant. Integrating equation 5.37 on the overall thickness W of the sample and solving it with boundaries conditions given by the surface recombination velocities (SRV) of the front and the rear sides (S_{rear}, S_{front}), the effective lifetime of the new generated charge carriers [Suw11] can be extracted

$$\tau_{eff}(\Delta n) = \frac{\Delta n(t)}{g_{ph}(t) - \dfrac{d\Delta n(t)}{dt}}. \tag{5.38}$$

Eq. 5.38 expresses a general case: when $d\Delta n(t) \to 0$ represents the steady-state of the system, and when $g_{ph} \to 0$ represents the transient solution [Nag99].

Assuming that the photogeneration is spatially uniform and the SRVs are low and approximately identical ($S_{rear} = S_{front} = S_{eff}$), the effective SRV can be related to the effective lifetime by:

$$\frac{1}{\tau_{eff}} \approx \frac{1}{\tau_b} + \frac{2S_{eff}}{W}. \tag{5.39}$$

Also, the QSSPC measurement can provide a current-voltage characteristic: the short-circuit current is obtained by the irradiance; the open-circuit voltage, referred as the separation of the quasi-Fermi levels, is implied by the excess of carrier density. The value of an *implied open-circuit Voltage* iV_{oc} can be calculated, using equation 1.1, for a solar cell made on a n-type wafer with dopant density N_D [Sin96]:

$$iV_{oc} = \frac{kT}{q} ln \left[\frac{\Delta p(N_D + \Delta n)}{n_i^2} + 1 \right]. \tag{5.40}$$

From this equation is clear that the implicit voltage depends on the p-n product at the junction.

5.3.2 Instrument apparatus

The instrument used in this work is the WCT-120 Photoconductance Tool from Sinton Consulting Inc. As represented in the sketch of figure 5.9, the lifetime measurement is realized using a flash lamp, a coil alimented by a RF circuit and a reference solar cell that measures the incident light intensity. The sample is placed on the top of the coil, and the excess charge carriers density can be extracted from the induced photoconductance $\Delta\sigma$:

$$\Delta\sigma = q\Delta n(t)(\mu_n + \mu_p) \cdot W \tag{5.41}$$

where μ_n and μ_p are the electron and the hole mobilities, respectively.

The $\Delta\sigma$ is measured via the voltage variation in the oscillating circuit. To calculate the generation rate an optical factor f takes into account the light absorption. This quantity can vary by the injection level of the samples (that affects the amount of absorbed light), by:

$$g_{ph}(t) = \frac{I(t) \cdot f \cdot N_{ph}^{1sun}}{W} \tag{5.42}$$

where *I(t)* is the illumination intensity and N_{ph}^{1sun} the density of photons in solar light with an irradiance of 1 sun. The factor used in this work was 0.81 for texturized samples and 0.70 for the planar samples. For the QSSPC measurements the a-Si was deposited on 4" silicon FZ wafers, with resistivity ρ = 1-5 $\Omega \cdot cm$. The injection level at which the lifetime was evaluated in our experiments is $\Delta n = 10^{15}\ cm^{-3}$.

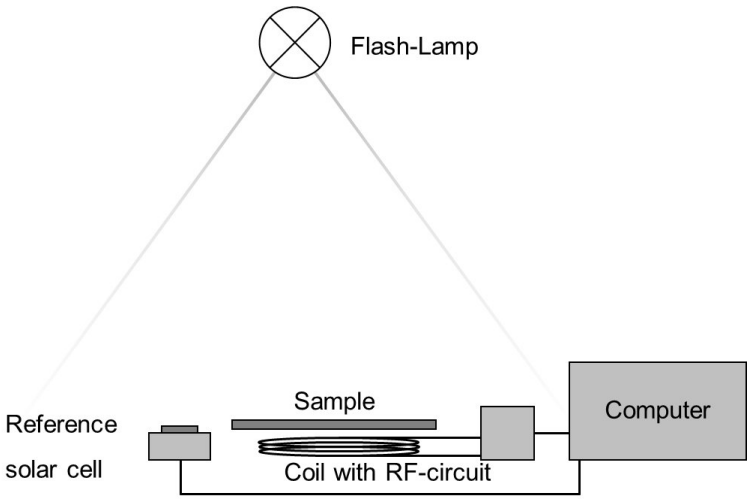

Figure 5.9: QSSPC setup

5.4 SunsVoc

SunsVoc is a technique that measures directly the Voc as a function of the light intensity, typically from a few suns to just below 0.1 suns, and can produce a pseudo I-V characteristics, as shown in figure 5.10.

In the measurement setup the sample is placed on the top of a metallic plate and connected with a conductive tip from the front side to the overall circuit. A xenon flash lamp illuminates the sample with exponentially decaying intensity that is detected from a reference cell. The open-circuit voltage is measured between the emitter and the backside. Considering that the short circuit current density is linearly proportional to the intensity of the light by $I = c \cdot J_{sc}$, the implied terminal current J_{imp} (corresponding to the short-circuit current of a 'real' IV curve) can be obtained by:

$$J_{imp} = J_{sc}(1 - I). \tag{5.43}$$

The pseudo-IV curve is the result of combining the voltage measurements with the implied current. Calculating this 'pseudo' output allows to determine the optimal operating point, which in a successive step leads to extrapolate a *Pseudo Fill Factor* (PFF).

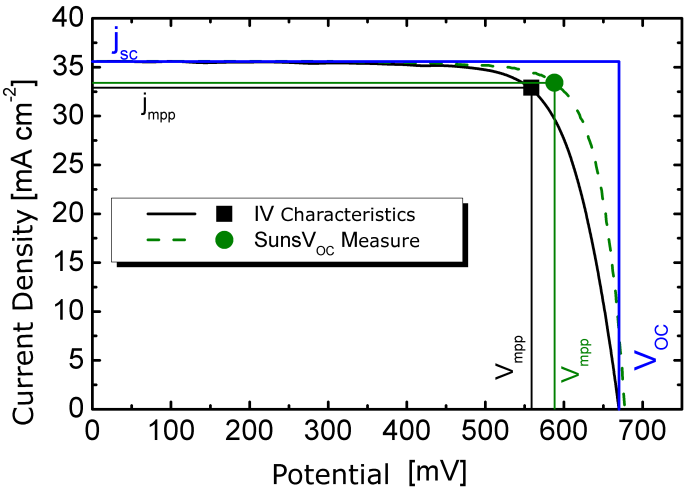

Figure 5.10: Pseudo I-V characteristics

There are small offset currents not expected (the system is in *open circuit*), but anyway the final result is not affected as no series resistances are measured.

Also, this measurement tool allows to predict the solar cell characteristics before the metallization process, as for SHJ samples, it is sufficient to have the p-i-N-i-n configuration (c-Si passivated by amorphous Si) plus the TCO on front and rear sides: these last layers are necessary due the low lateral conductivity and the low charge carrier density of a-Si.

The big advantage of this technique in heterojunction solar cells is an easy and fast characterization of the electrical properties that allow to develop an improved global structure, without completing the precursor with metallization.

CHAPTER 6

Experimental Results

The present chapter contains the experimental results and related discussions conducted in this thesis. The physical properties of the sub-oxides and sub-carbides a-Si thin films are characterized: at the beginning the study is focused on the quantitative incorporation of oxygen and carbon atoms occurring in amorphous silicon layers and the hereby structural and optical modifications; then, in order to observe and correlate the hydrogen effusion, the crystallization and the degradation of the electronic properties (lifetime of photo-generated charge carriers and open-circuit voltage), the results of isochronal annealing measurements are shown. All the experiments are developed with the aim to understand how the structure of a-Si alloys can result more stable when exposed to thermal stress, and which beneficial effect has an implementation of these specific layers in a silicon heterojunction solar cell. The last section briefly analyses the systematic errors coming from the assumptions made to evaluate the data and the uncertainties related to the deposition process and the characterization measurements.

6.1 Structural study of suboxide and subcarbide amorphous silicon layers

6.1.1 Deposition

The PECV deposition of amorphous silicon depends on the chamber geometry and conditions, the process parameters and the specific substrate wafer. For further details on the used deposition machine and the optimized chosen parameters, the reader is referred to chapter 4. In this work float-zone n-type wafers, with thickness $d_{wafer} \approx 200\ \mu$m, were used as c-Si substrates: table 6.1 shows the specific variations utilized for a-Si deposition. <111> surfaces were chosen in order to compare the behaviour both with the texturized wafers that have <111> pyramidal facets, and planar <100> surfaces.

The thickness of the characterized a-Si samples was set to $d_{a-Si} \approx 12$ nm for QSSPC

measurements, and for FT-IR and SE two different batches were used with $d_{a-Si} \approx 15$ and 12 nm. It has to be noted that when producing a SHJ solar cell the *intrinsic* layer has a thickness d_{a-Si} of 5-10 nm; however the thickness evaluated in this thesis is chosen in order to have a signal strong enough from the optical tools, especially FT-IR.

The growth rate on pyramidal surfaces (the texturized wafers) is slower than on planar; therefore the deposition time on this kind of substrate was multiplied by a factor of 1.6, estimated measuring their thickness by SEM (scanning electron microscope) cross-section measurements.

Table 6.1: FZ wafers used for a-SiX:H deposition

Manufacturing on double-side	**Orientation**	**Resistivity** Ω·cm
polished	<100>	1.0
polished	<111>	1.7
texturized	-	1.0

The layers investigated in this work are the intrinsic alloy a-SiO_x:H(i), a-SiC_y:H(i) and the stack with standard p-doped layer a-SiO_x:H(i)/a-Si:H(p), a-SiC_y:H(i)/a-Si:H(p); all the designed sample are depicted in figure 6.1.

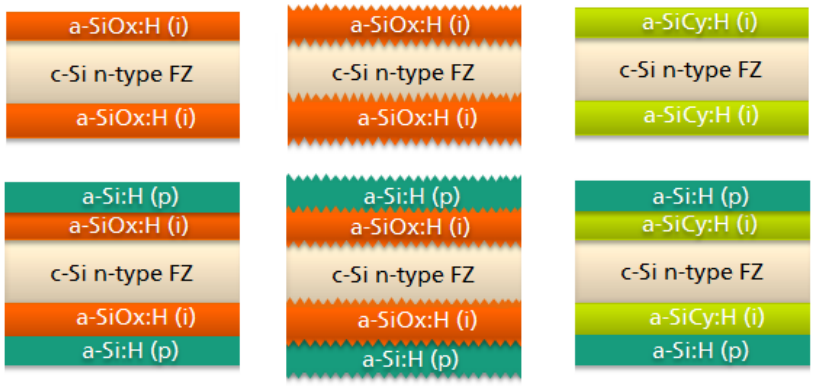

Figure 6.1: Sketch (not in real scale) of the a-Si samples investigated in this work

6.1.2 Bonding configuration of a-Si alloys

a. Static refractive index of a-SiO_x:H and a-SiC_y:H

The *static refractive index* n_∞ represents the dispersion of a low energy radiation (like IR) passing through a specific material. This quantity is fundamental for the calculation of the bonding, and atomic density inside the thin film, using equation 5.9. In this work the refractive index is measured as function of the wavelength by the spectroscopic ellipsometer (using the fit of optical models, see paragraph 5.2). The n_∞, that corresponds to a constant value when $\lambda \to \infty$, was extrapolated choosing the point measured with lowest energy by the SE, that is when $\lambda = 994.56\ nm$ or, in wavenumbers, $\omega = 10054.7\ cm^{-1}$.

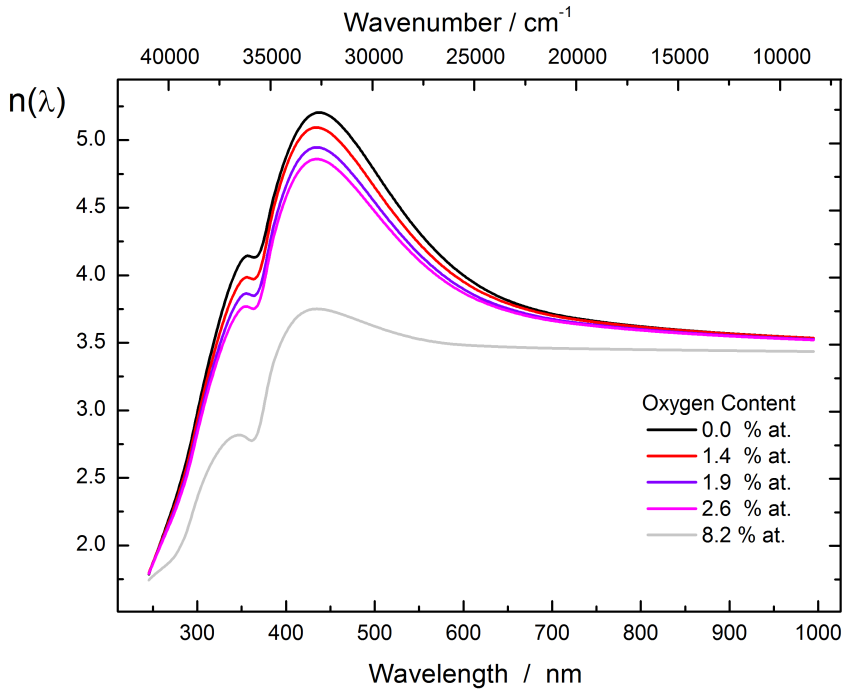

Figure 6.2: Refractive index of a-SiO_x:H, measured by SE

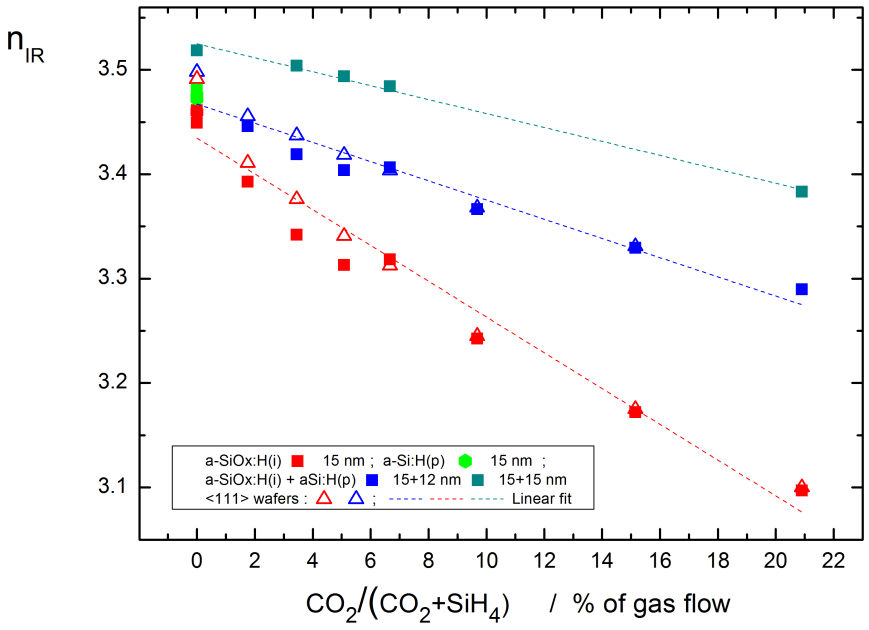

Figure 6.3: Static refractive index of a-SiO_x:H, measured by SE

Figure 6.2 shows n(λ) for a-SiO_x:H : it is evident that the incorporation of oxygen reduces the wavelength dispersion of the amorphous silicon. Also, at high λ, the constant value tendency is shown. For a-SiC_y:H, analogous results were observed, but for the sake of clarity these are not shown in figure 6.2.

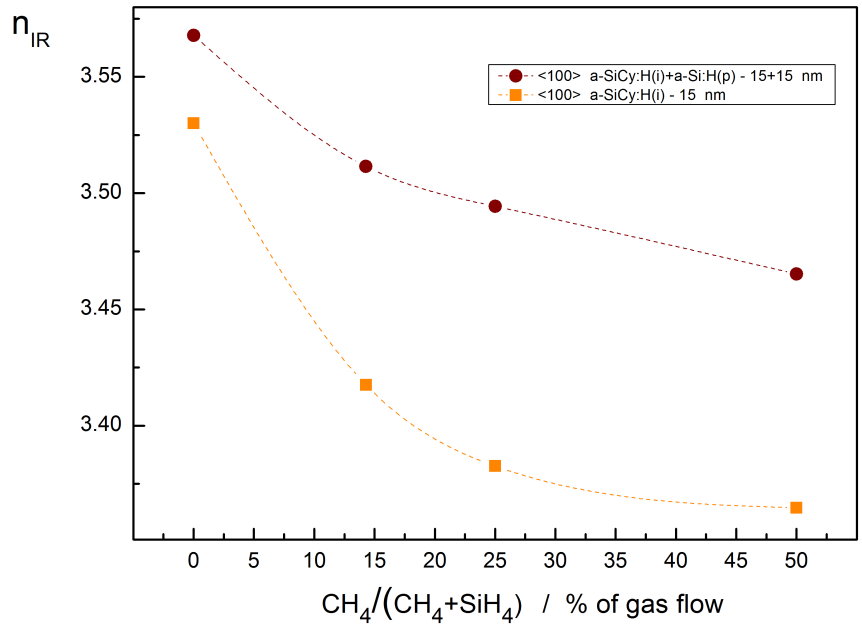

Figure 6.4: Static refractive index of a-SiC$_y$:H by SE, the line is a guide to the eye

Figures 6.3 and 6.4 represent the n_∞ of a-SiO$_x$:H and a-SiC$_y$:H, respectively, as function of the gas flow percentage ($CO_2/(CO_2+SiH_4)$ and $CH_4/(CH_4+SiH_4)$). Considering the first graph, it can be observed that the IR dispersion linearly decreases (for samples having same thickness) increasing the CO_2, clearly indicating a change in the film composition. The crystal orientation (<100> and <111>) and the doping (see the green point symbolizing the a-Si:H(p)) of each single layer do not influence the refractive index, as the results are similar; conversely, the stack (i)+(p) shows the same trend of the intrinsic but with more increased refractive index: this result could be explained by the different thickness of the stack (among the double), but also by a different structural configuration. To study the phenomenon of the influence of the thickness, samples with $d \approx 30\ nm$ in the three cases (i, p and i+p) were deposited (with 9 % of CO_2 gas flow for the *intrinsic* layer): it can be observed in table 6.2 that for thick samples the influence of oxygen is higher, as the O$_x$ quantity affects the dipolar and the dispersive properties of the layer; the doping is more relevant as well at 30 nm, increasing the refractive index, while the stack at $d \approx 15 + 15\ nm$ has a combined effect of the oxygen inside the intrinsic and the boron of the doped layer. It is known that the refractive index is correlated with the material density [Jan97]; the O$_x$ atoms inside the amorphous network can cause a less dense material (glass, for example, has $n \approx 1.6$) and the figure 6.3 suggests that the p-doped samples and stack have a higher global density as compared to the one of the single *intrinsic* layers. More results about this aspect will be investigated from FT-IR spectra.

The figure 6.4 shows analogous results incorporating Cy in a-Si:H layers. It can be noted that in this case the decrease is not linear and the n_∞ goes to 3.36 for 50% of methane gas flow ratio. Most probably the carbon incorporation (less electronegative than oxygen) has a different behaviour with the atomic arranging inside the amorphous

structure. Also, it has to be noted that the much lower power density in the deposition machine *AK400M*, as compared to the *Clustertool*, leads to lower incorporation.

Table 6.2: n_{IR} for samples with i-layer deposited using 9 % of CO_2 flow ratio

d / nm	$n_\infty(i)$	$n_\infty(p)$	$n_\infty(i+p)$
15	3.24	3.47	-
30	3.14	3.58	-
15 + 15	-	-	3.46

b. IR analysis of a-SiO$_x$:H : hydrogen density

The n_∞ is needed to calculate the atomic density and percentage concentration, evaluating the absorption peaks from FT-IR measurements, all of which will be explained in the following.

The H content is the parameter investigated at first as, even incorporating suboxides and sub-carbides alloys, the hydrogen is the most important passivating species [Ein12], mostly accumulated at the interface c-Si/a-Si, and has a crucial role for the reduction of Si dangling bonds (see chapter 3).

Table 6.3: Frequencies of Si-H stretching modes for a-SiX:H

Mode	ω_0 / cm^{-1}	Type
LSM	2005	(i),(p),$(i+p)$
HSM(1)	2085	(i),(p)
HSM(1)	2090	$(i+p)$
HSM(2)	2160	(i),$(i+p)$
HSM(3)	2230	(i),$(i+p)$

Figure 6.5 represents the Si-H stretching modes of a-SiO$_x$:H, at each variation of CO_2 flux. To analyse them, gaussian deconvolution was necessary with the following fit parameters: the area of the peak I_H, the FWHM (full width at half maximum) and the height of the 0 scale (useful to remove the signal noise). The frequencies of each stretching mode are not fit parameters but are chosen from the average value obtained comparing all the samples: the set values are reported in Table 6.3 (all the values are consistent with the ranges shown in table 5.1). This method to choose the FT-IR peak frequencies was already used in literature [Ein12]; the motivation for it is that the maximum excitation position of the IR oscillators (the molecular Si-H bonds) is always reasonably constant and allows an easier comparison between different samples.

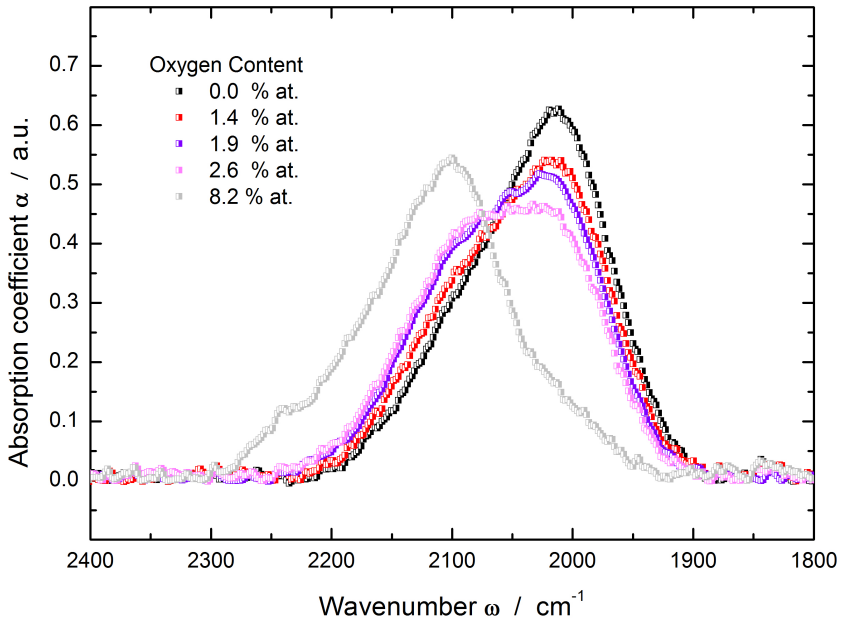

Figure 6.5: Si-H stretching modes for a-SiO_x:H

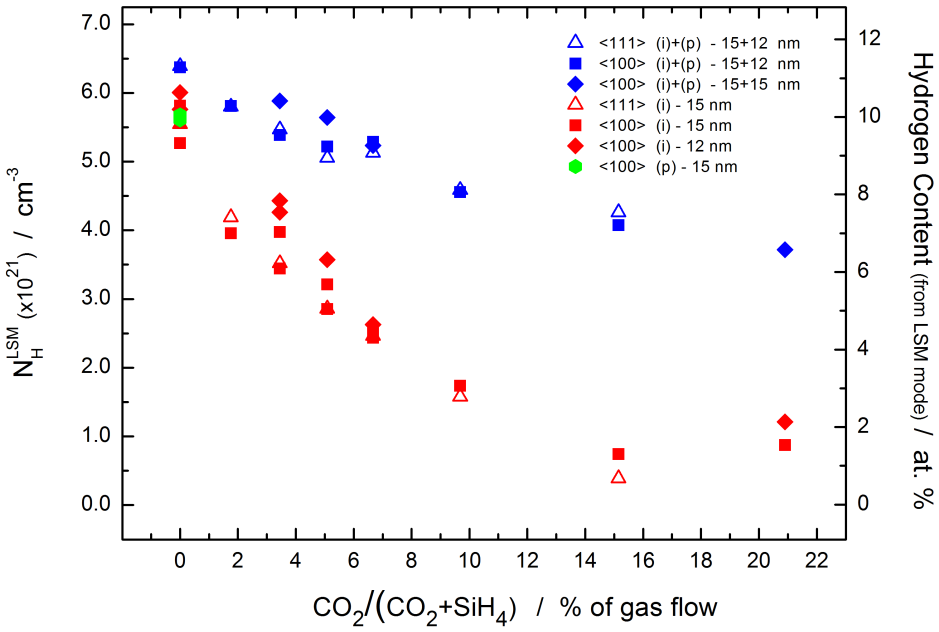

Figure 6.6: H density from low stretching mode for a-SiO_x:H

As exposed in paragraph 5.1, the Si-H stretching modes are essentially of two kinds: the *low-stretching mode* referred to standard Si-H oscillating bond and the *high stretching mode*, when the excitation frequency of Si-H is shifted due to changes of the structural and molecular surrounding of the specific bond. Especially, the first HSM

($\approx 2090\ cm^{-1}$) was always difficult to identify as di-hydride (Si-H_2) or as bond with back-bonded oxygen (or carbon) [Bro11]. Anyway in our samples the HSM(1) is highly evident and increases by adding CO_2 or CH_4 gas flow at the deposition process; furthermore, the mean total hydrogen content (of all the samples) was measured as $C_H = 15 \pm 1$ %, slightly above the range of *voids-dominated layer*: therefore, using the analysis of Smets [Sme07], it can be assumed (and will be verified later) that di-hydride are a negligible fraction at the voids surface in a-Si:H films grown with the examined process. The HSM(2) and the HSM(3) were observed just with the maximum CO_2 flux (20.9% of gas flow), hence can be identified as shifts due to multi-oxygen back-bonds.

The H density from the low stretching mode is plotted in figure 6.6. As suggested from the spectrum of figure 6.5 the oxygen reduces the presence of this vibrational mode mostly in a linear way up to a CO_2 ratio = 15 %. From a starting density, for normal a-Si:H, around $6.0 \times 10^{21}\ cm^{-3}$, till decaying of 1 order of magnitude at high oxygen incorporation. An interesting result is that the *i* and the *p* a-Si:H incorporate approximately the same density of hydrogen, while the stack (i+p) seems to contain slightly more H (around $6.5 \times 10^{21}\ cm^{-3}$). This result is contradictory with the study of DeWolf [DWo07], that observed less H density for the stack as some H has effused from the intrinsic during the deposition of the (p) layer. However in our case the deposition of the (p) layers (at the table set temperature of 200 °C) does not seem to contribute to H effusion, possibly due to lower actual sample temperature; and the result of an higher H density in the stack, confirmed also from the measured higher refractive index, could be explained considering that, during the deposition of the doped layer on the (i), an hydrogenation could constitute the interface between the 2 a-Si:H films.

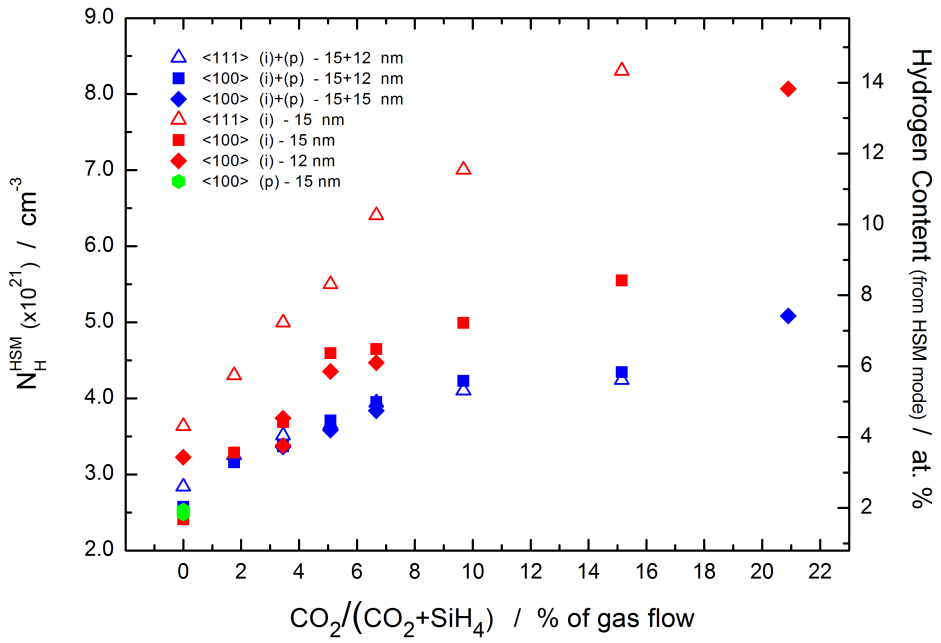

Figure 6.7: H density from high stretching mode for a-SiO_x:H

However, including O_x in the *i* layer, it is straightforward that the LSM of the stack remains at higher H density, as there is a contribution of the LSM belonging to the *p* that are not perturbed (or shifted) by the CO_2.

The frequency shift of the HSM mode, induced by the more electronegative oxygen is observed in figure 6.7, representing the N_H^{HSM} as a function of the CO_2 gas flow. This increase of the high stretching mode can be explained with an increased void density as well, caused by O_x incorporation. The stack in this case has a coherent behaviour with the graph of figure 6.6, as the increase is lower due to the constant low density HSM of the *p* layer on the top. It is interesting to note that in this vibrational mode the crystal orientation seems to influence the H accumulated in the *intrinsic* case: the <111> wafer has a slightly higher H content than the <100>. This result is contradictory with the results reported by Descoeudres [Des11], who observed identical IR spectra for <100> and <111>.

c. IR analysis of a-SiO$_x$:H : oxygen content

To calculate the oxygen content in a-SiO$_x$:H layers the deconvolution procedure was used on the Si-O-Si stretching mode, with the same approach of Si-H, but in this case the peak frequency is a fit parameter.

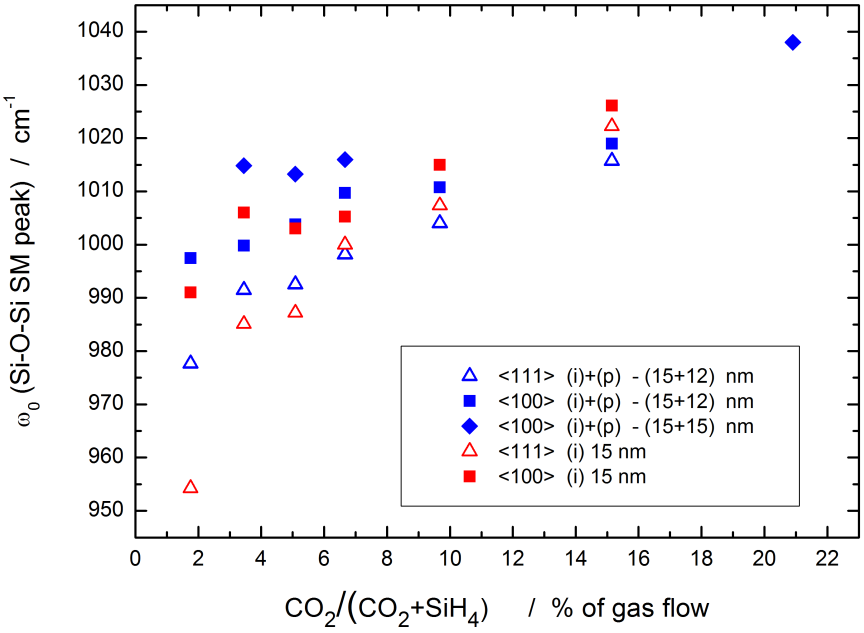

Figure 6.8: Frequency shift of Si-O-Si SM

Studying a-SiO$_x$ layers deposited on <100> oriented surfaces, Einsele recently observed that by increasing the CO_2 flux in the PECVD chamber the peak frequency ω_O and the area of the integrated absorption I_O increase as well [Ein12]. Our samples confirm these results: the figure 6.8 shows the frequency ω_0 vs the CO_2 flux ratio and indicates clearly the shift of the peak position. Also, it is interesting to evidence the behaviour of <111> oriented surfaces, that have a lower excitation mode, more clear at low values of

CO_2. This could mean that the crystal orientation of the wafer on which the a-Si grows might influence the incorporation of the oxygen. This global shift is explained by the strong polarizing effect of oxygen atoms inside the amorphous structure of tetrahedral Si bonds: increasing the CO_2 the probability of neighbouring Si-O-Si bonds influencing each other increases, modifying the dipolar surrounding, as observed for Si-H stretching mode.

The area of Si-O-Si peak I_O was observed to grow linearly with the CO_2 flux ratio, and its value was used in equation 5.9 to calculate the oxygen density N_O, shown in figure 6.9. In this case the less N_O measured for the stack can be attributed to the different thickness, and so the volume, of the *i+p* case respect to the *i*. However the linear growth presents more fluctuations when CO_2 ratio is ≤ 7 %: at this range the oxygen incorporation seems more difficult to control. A last note: some sample grown without CO_2 had an I_O or $N_O \neq 0$, that can be caused from a surface oxide layer on a-Si due to air oxidation after the deposition or some molecules or O_x atoms in the reactor chamber from prior processes with CO_2 that provoked oxygen incorporation (around 2-3 $\times 10^{20}$ cm^{-3}). For considerations about this aspect the reader is referred to paragraph 6.4.1 .

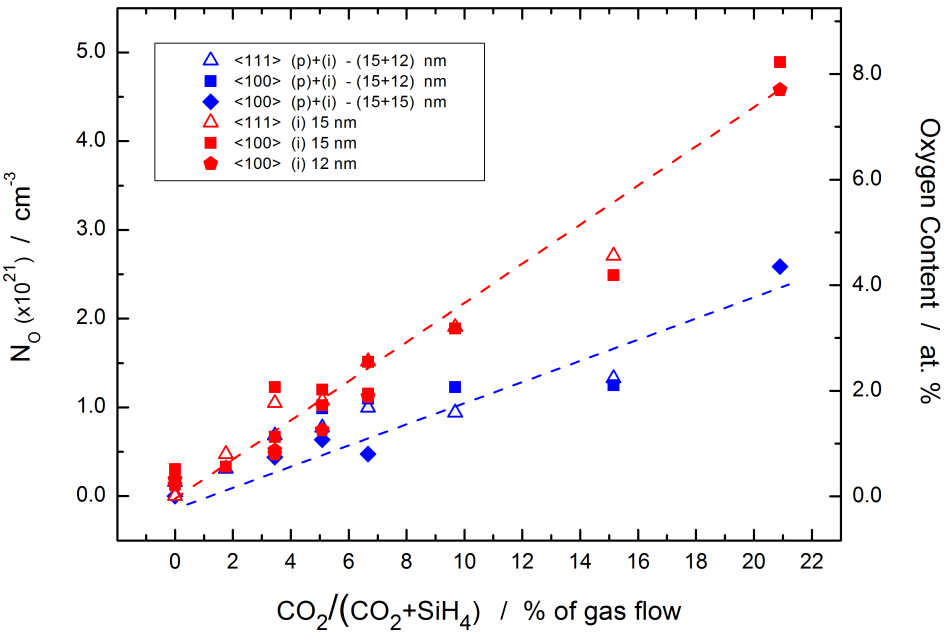

Figure 6.9: Oxygen incorporated from Si-O-Si SM, variating CO_2 gas flow

d. IR analysis of a-SiO_x:H : internal voids concentration

As suggested from the refractive index, the sub-oxide a-SiO_x:H alloy is a less dense layer than a-Si:H: therefore, recalling the assumptions of the sub-paragraph 5.1.4c, incorporating oxygen a smaller amount of silicon is incorporated in the atomic network. Using equation 5.23 it is possible to estimate the internal voids concentration of the a-Si layers. The formula of eq. 5.23 is obtained solving the Lorentz-Lorenz relation of

eq. 5.15 (and eq. 5.20) for N_{Si}. This calculation was done using: N_H, N_O coming from the FT-IR spectra, n_{IR} coming from ellipsometer measurements. Hence the decrease of the silicon density can suggest an increase on the porosity of the deposited layer.

Figure 6.11 shows how the number of voids is increasing with increasing CO_2 flux during the deposition. When the concentration is more than 10 %, i.e. at CO_2 flux ratio > 14 %, we expect a porous structure of the layer. It can be noted that the voids content for the stack is higher than the (i) layers: this result comes from the above observed high H density between a-Si:H(i) and a-Si:H(p), that could be correlated with interface nano-sized voids, and the low refractive index of the overall stack. Studying the normal stack, De Wolf [DWo07] considered the degradation due to the higher DB density respect to the (i) due to the shift of the Fermi level (this will be analysed in more detail in 6.2), and the H effusion from *surface interconnected voids*. The result of figure 6.11 suggests that this higher amount of voids could be located between the two a-Si layers, as we already suspected to have more H incorporation. An other note: as shown in figure 6.10, when a-Si(p) is grown on a-Si(i) its thickness is smaller as compared to grown on c-Si; so instead of growing the *doped layer*, at the beginning it could occur an hydrogenation on the *intrinsic* surface.

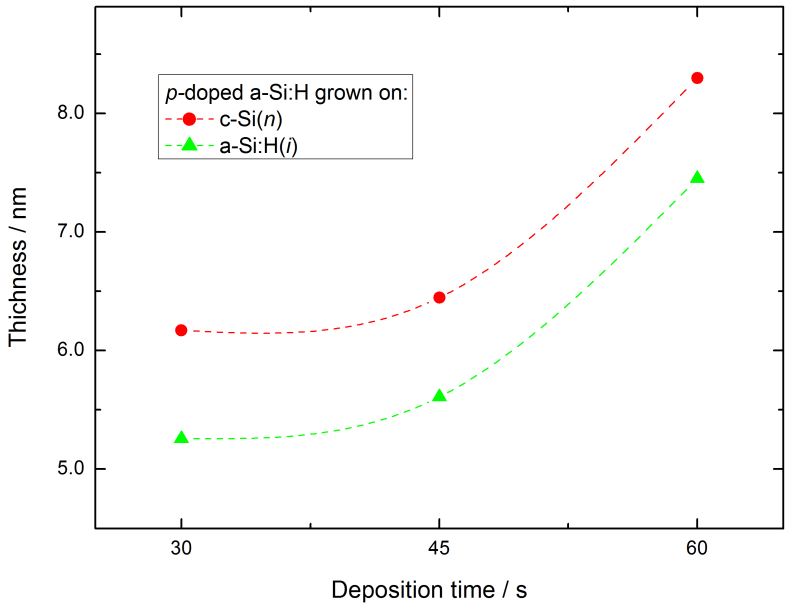

Figure 6.10: *p*-doped a-Si:H grown on a-Si:H(*i*) and on c-Si

In figure 6.12 the voids are represented as function of the hydrogen positioned at the high stretching mode. This relationship was found by Smets [Sme07] to identify the composition of the amorphous silicon layer. For layers dominated by vacancies an exponential relationship is observed, whereas a linear behaviour characterizes a *void-dominated* layer.

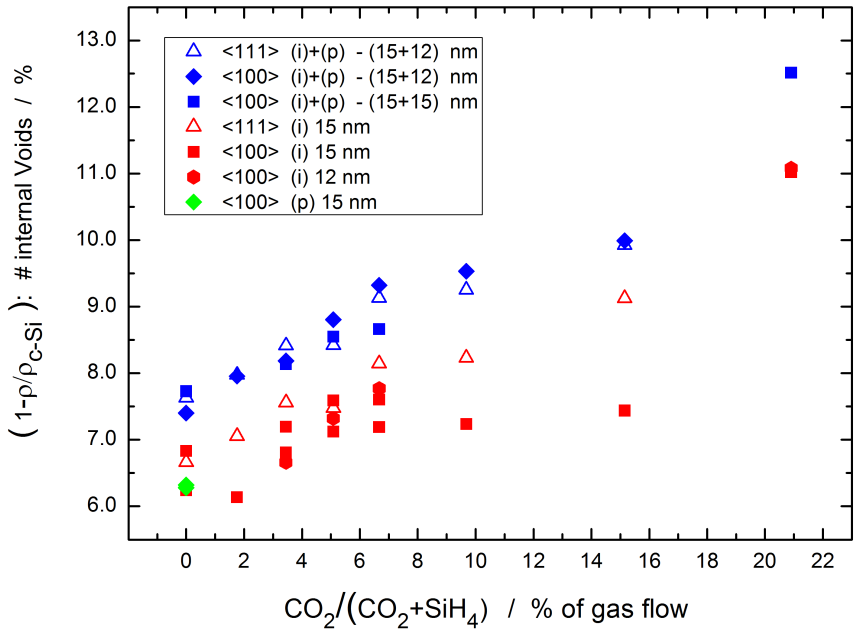

Figure 6.11: Voids induced by CO_2 in a-SiO_x:H deposition

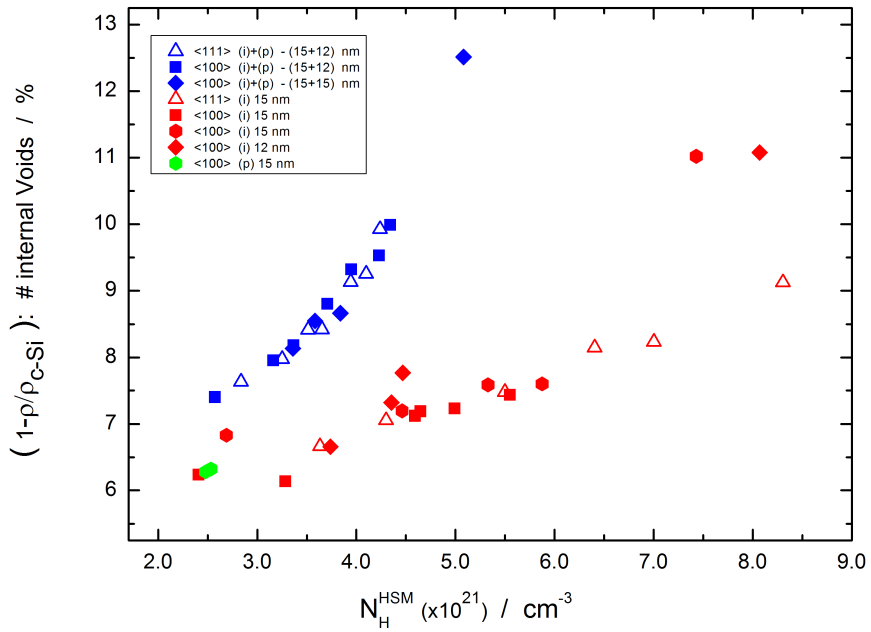

Figure 6.12: Concentration of voids in dependence of the HSM, the linear behaviour is an indicator for a-Si consisting of voids

The data for (i) and the (i+p) samples point to a linear trend, corresponding to the *void-dominated* composition. Thus the Si-H HSM can be considered as oscillating bonds inside the voids induced by oxygen. Anyway the deviations from linearity can

be attributed to the O_x induced-HSM: in Smets analysis the consideration was just with a-Si:H films having different N_H^{HSM}, while in our work the alloy can result in a more complex behaviour. It is interesting to note the symmetry between the intrinsic samples and the stack: even the (i+p) systems have lower N_H^{HSM}, reach higher voids content at lower oxygen incorporation of the intrinsic passivation layer underneath, result already observed in figure 6.11. Also, this result confirms the assumption to neglect the presence of di-hydrides in our samples.

e. IR analysis of a-SiC$_y$:H : carbon content

Until now all the analysis was focused on a-SiO$_x$:H layers, with oxygen concentration lower than 10 %. The sub-carbides obtained by inserting CH_4 in the deposition chamber, were also deposited with low ratio CH_4/SiH_4, in order to obtain Si-rich alloys.

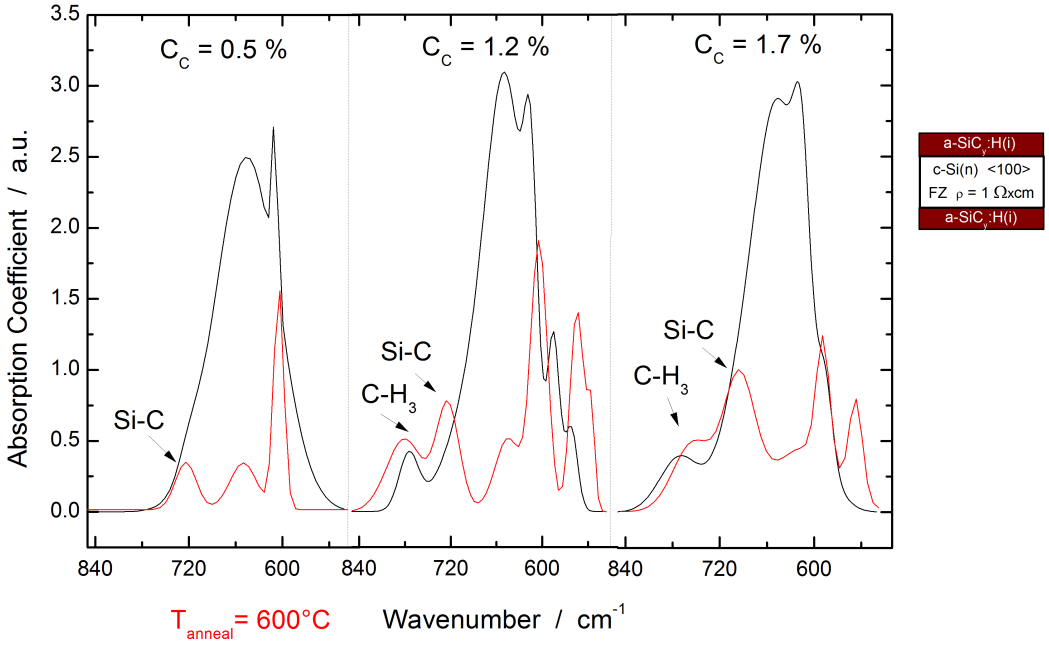

Figure 6.13: Si-C stretching mode revealed by annealing procedure

The carbon content was calculated from the Si-C stretching mode, positioned at 720 cm^{-1}. Difficulties to identify the corresponding FT-IR peak were already exposed by Suwito [Suw11], as this peak is normally superposed by the wide peak of Si-H wagging mode, positioned at 640 cm^{-1}. Therefore, to reveal the Si-C peak, the samples were annealed at $T = 600°C$ for 10 minutes, causing the total effusion of the H atoms collected inside the a-Si:H layers. In figure 6.13 the absorption coefficient is plotted, showing in the black lines the non-distinguishable peaks and in the red lines the acquired signal after the annealing. Strong influences of the heating procedure on the Si-C bonds are not expected, but cannot be excluded. For further analysis it is crucial to observe that after the annealing, for $CH_4 \neq 0$, the C-H_3 wagging mode positioned around $780cm^{-1}$ is identifiable and has not disappeared: this effect is due to an higher stability of the C-H bond, in comparison to the Si-H.

From this analysis it was possible to evaluate the carbon incorporation, integrating the peak at 720 cm^{-1} and using eq. 5.9, with the already mentioned *absorption constant* $C_{Si-C} = 2.13 \times 10^{19}\ cm^{-2}$ [Har10] (for more informations see paragraph 5.1.4a). The results are plotted in figure 6.14, and compared with SIMS measurements made in the work of Suwito [Suw11]. The a-SiC:H samples of Suwito were deposited in the same machine (*AK400M*), and with a thickness around 100 nm. So a good matching between the C incorporation independently calculated by our FT-IR analysis and the one obtained by SIMS can be observed. Neglecting the influence of temperature treatment to drive out the H, the carbon collected at $CH_4 = 0$ most likely is due to some methane adsorbed at the chamber walls that were not cleaned before the deposition.

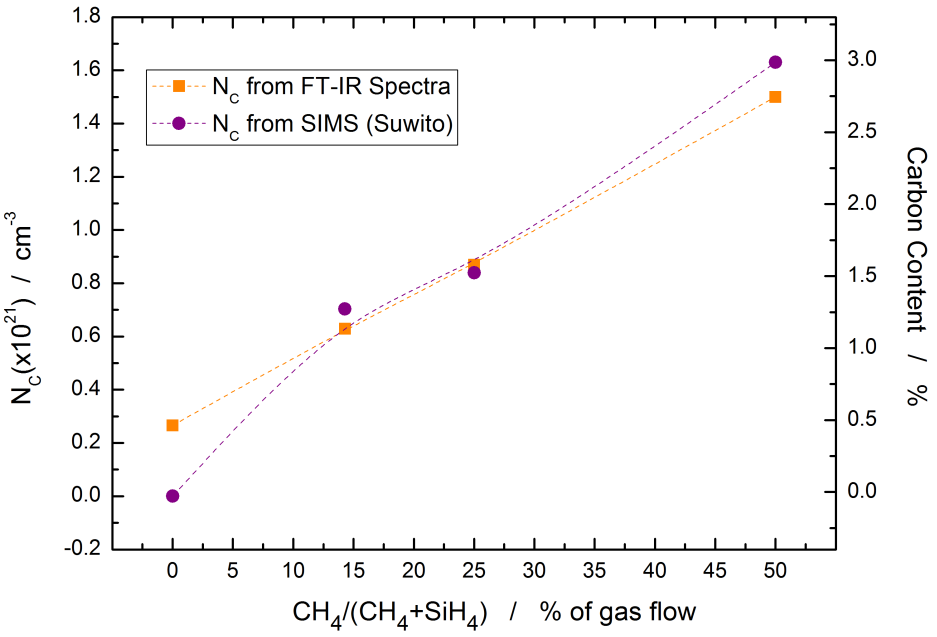

Figure 6.14: Carbon content by Si-C stretching mode, variating CH_4 gas flow ratio, the lines represent a guide to the eye

f. IR analysis of a-SiC$_y$:H : H density and voids concentration

The H incorporation in a-SiC$_y$:H has a different behaviour than in a-SiO$_x$:H, because in this case the gas source is CH_4, hence the inclusion of Carbon corresponds to an higher Hydrogen deposition. Additionally, a different reactor with a different process was used.

In figure 6.15-left the N_H of LSM and HSM are represented. The decrease of LSM and increase of HSM is also observed here, but it has to be noted that the total H density of the a-Si:H deposited in the *AK400M* is lower than the H density of a-Si:H deposited in the *Clustertool*: this comes from the difference of both the deposition machines and the deposition processes.

In figure 6.15-right the voids concentration is depicted, as function of the N_H^{HSM}, confirming the linear trend as in the previous case. Another relevant detail is that the voids in the a-SiC$_y$:H layers are in a range lower than 7 %, slightly lower than the

a-SiO_x:H: this result can be addressed to the deposition process as well, but anyway suggests that the a-SiC_y:H samples are more stable and less porous.

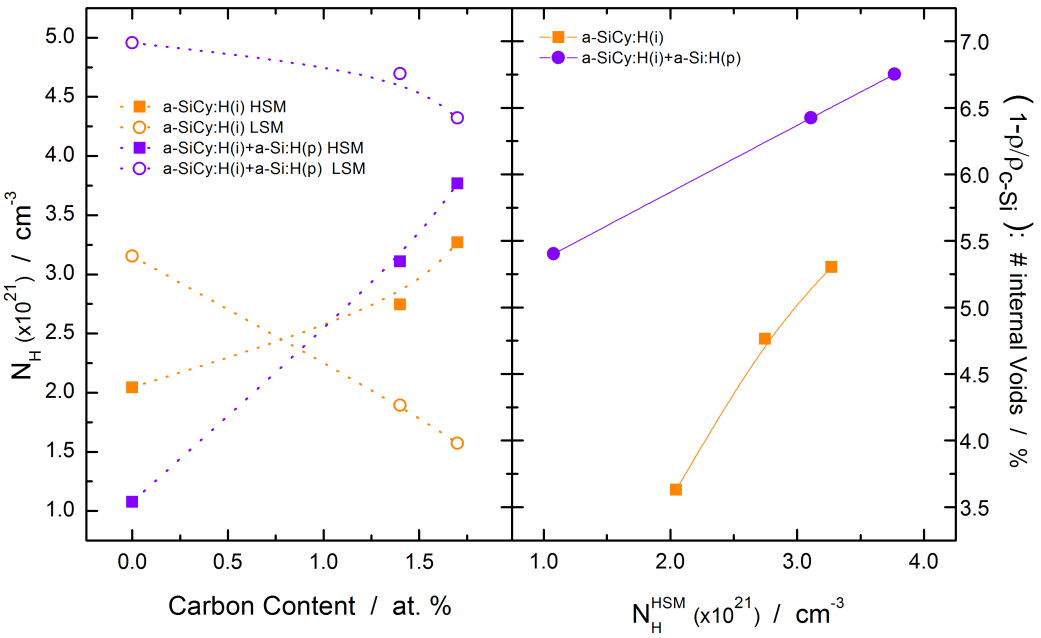

Figure 6.15: SM and voids in a-SiC_y:H films

6.1.3 Amorphous structure and crystallinity

a. Imaginary pseudo-dielectric Function: TL and CL optical models

The imaginary pseudo-dielectric function obtained by Tauc-Lorentz and Cody-Lorentz model reveals that the incorporation of oxygen increases the amorphous structure of the deposited a-Si, reducing the density of internal crystallites mostly present at the interface c-Si/a-Si. The interface is crucial for a-Si:H investigations, as was reported by Kondo [Kon07], because it determines the undesired epitaxial growth, with the related degradation in surface passivation.

Figure 6.16 reports the pseudo-dielectric functions of the respective a-SiO_x:H layers, at each variation of the CO_2 gas flow. With increasing O_x incorporation, the two peaks referring to the crystalline component inside the layer decrease; furthermore at the maximum CO_2 flux the second peak, situated around 3.7 eV and more associated to a long range order, has diminished. The oxygen incorporation increases the number of the many Brillouin configurations, that indicate the amorphous state, resulting in a dielectric function with a broader range. Especially the region under 2.5 eV is more covered, and can have influences on absorption behaviour (this aspect is analysed in next paragraph 6.1.4).

The use of an optical model is strictly related to the quantities to investigate. The Tauc-Lorentz is one of the most used to analyse SE data of amorphous silicon: the

Amplitude of the oscillator and the Γ *Factor*, as far as the energy gap, are the interesting output parameters that result from the fitting procedure. Also, the multi-layer model necessary to interpret the Ψ and Δ experimental values has a fundamental importance in order to reproduce the optical path of the polarized wave. In the case of TL for a-Si thin films, the three-layer model with the insertion of the interface was used (see figure 5.7b). The analysis was focused on the bulk layer of a-SiX:H, to reveal the structural properties with this optical model. This layer was converted in *EMA* layer utilizing the internal voids to improve the fit. The use of *voids EMA layers* was widely discussed in literature, finding supporting and adverse opinions (see [Fuj07], [Los01]). In our case the insertion of % of voids as fit parameter is motivated by the already shown FT-IR result; anyway it has to be pointed out that the voids from FT-IR results and the ones from SE analysis are not exactly the same, as the ellipsometer fitting model is strictly dependent on the optical constants that are set as starting values. In figure 6.17 the main results from TL analysis of a-SiO_x:H (15 nm) on <100> Si oriented wafers are shown: each data point corresponds to the mean value of measurements of 4 samples each oxygen content. Analogous, and not reported, results were obtained with different thickness and different orientation, and from a-SiC_y:H layers as well.

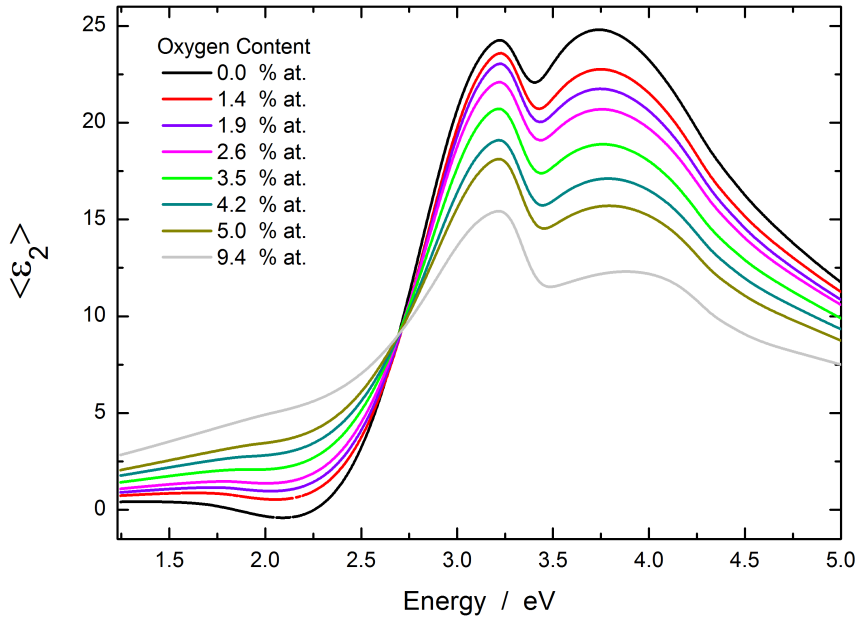

Figure 6.16: Pseudo-dielectric function of a-SiO_x:H layers

In figure 6.17(a) the bulk voids are shown as function of the CO_2 gas flow percentage ratio: it can be noted that in the cases < 5 % (corresponding to an incorporation not higher than 1.4 %) this fit parameter remains 0 because, as just mentioned, the TL model is suitable to fit a-Si:H and does not observe variation with such low oxygen content in the layer. At this point the difference with the FT-IR voids is considerable, as from the IR spectra we observed already 6-7 % for normal a-Si:H. However it is interesting to observe that a similar trend is maintained, confirming the increase of the porosity of the thin film. In figure 6.17(b) the amplitude of the oscillator is represented:

this increase explains the broadening of the imaginary pseudo-dielectric function shown in fig. 6.15. In the last plot, in figure 6.17(c) the Lorentzian Γ *factor* is displayed: this quantity expresses the energy losses inside the bulk due to free atoms, indicating point defects or disordered structure: this mostly linear growth represents the gradual increase of the long range disorder inside the bulk, as more oxygen is added to the alloy.

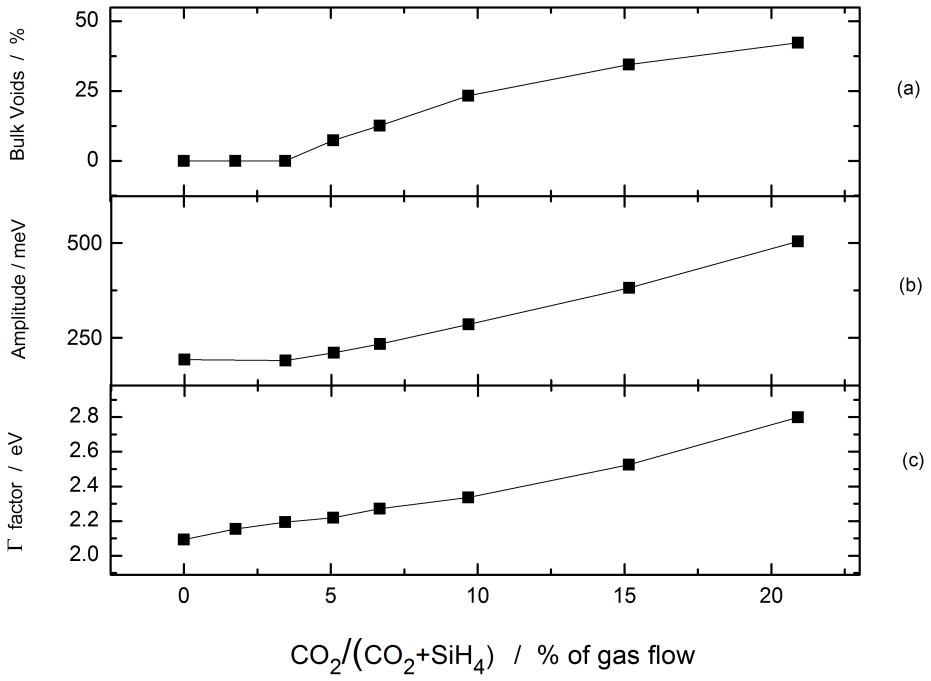

Figure 6.17: Evolution of % of voids, amplitude and Γ factor from TL analysis of a-SiO_x:H(i) layers

Due to the above mentioned shortcomings of the TL model, the suitability of an other one was investigated as well: the Cody-Lorentz model is more accurate than the TL since it also considers the exponential decrease of the DOS inside the gap due to the Urbach tails. The quantities that can be extrapolated are the Urbach energy and the Cody gap. The Urbach energy is shown in figure 6.18, for <100> and <111> oriented samples, and also in this case the final result is the main value of 4 samples: while the 11 nm thick wafers give slightly higher values, the crystal orientation does not seem to influence the trend. The linear increase of the Urbach energy expresses the higher disorder of the alloy system (as noticed by the ϵ_2 of figure 6.16 and by the Γ *factor* of figure 6.17(c)) but it is related to the density of the dangling bonds inside the a-Si network as well (see paragraph 3.1.2 and [Sch11]): therefore this linear trend suggests a different electronic configuration that could cause a different behaviour of the H passivating specie inside the layer (lifetime measurement are analysed in paragraph 6.2.3). Anyway this result was observed also for sub-carbides layers and is confirmed, for a-SiC_y:H, from [Bas10]: from the atomic bonding point of view the disorder is addressed to the increase of the bond angle distortion brought by carbon or oxygen incorporation. Also in this case the linear increase starts when the starting values of the CL model are not more suitable to reproduce the optical behaviour of the thin film, hence after 5 % of the CO_2 gas flow.

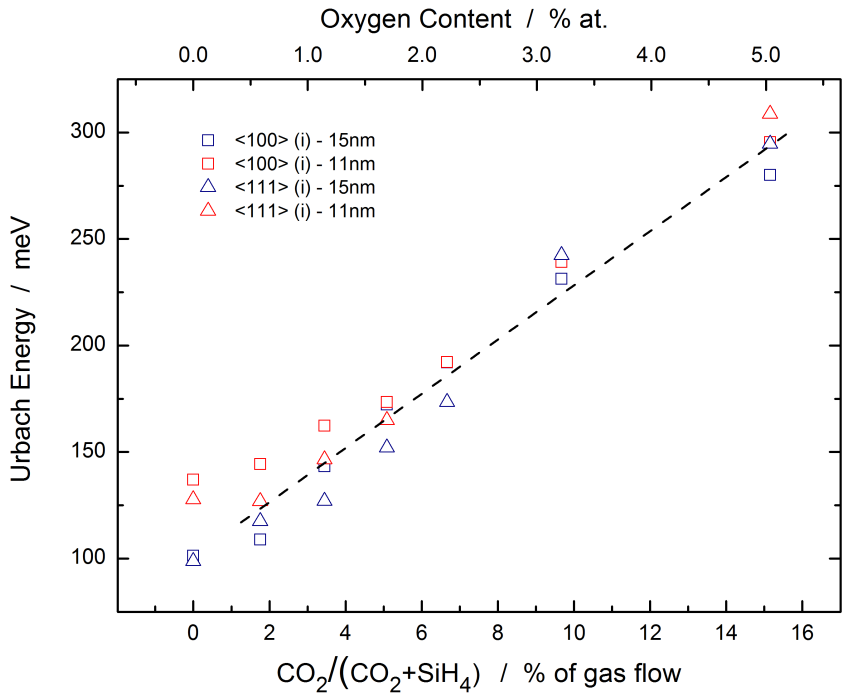

Figure 6.18: Urbach Energy from CL optical model

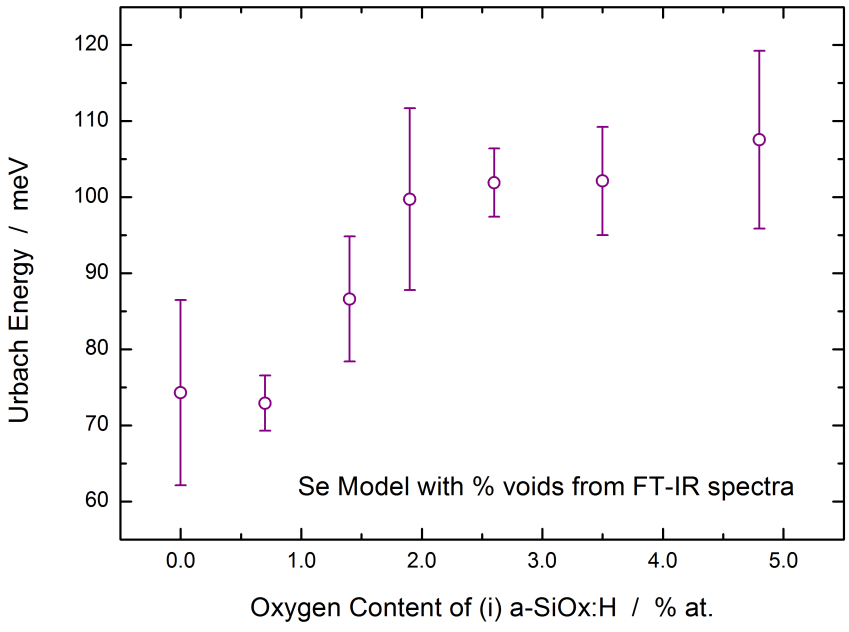

Figure 6.19: Urbach Energy from CL optical model, adding voids % from FT-IR results

These values of Urbach energy are in the same order of magnitude as the ones regarding standard a-SiH, recently measured (using the same model) in [Ge13], but they are almost one order of magnitude higher than the ones measured with photo-electron spectroscopy (PES) from Schulze [Sch11], and anyway much higher than the

typical values reported in literature [Sea98], [Sme07]. In [Ge13] this high discrepancy is addressed to a substrate difference, as Schulze characterized <111> wafers while Ge worked on <100> wafers. In our work we analyzed both of them and, as is shown in figure 6.18, the crystal orientation does not influence the trend of the Urbach energy. Our hypothesis is that the Cody-Lorentz model is not perfectly suitable to simulate perfectly the *pseudo*-dielectric function in the range below the energy gap: this difficulty could come from the solution and the subsequent fit of the Kramers Kronig relations used for the real component $< \epsilon_1 >$. Indeed, as shown by the original paper of Ferlauto [Fer02], several approximations are necessary to solve the Cauchy principal: these approximations could reduce the goodness of the fit. Pointing out this motivation, in the present work a new method is used to evaluate the SE data, always using the CL model. The analysis was reproduced using an *EMA* to model the a-Si substrate, inserting as constant values the percentage of voids obtained from FT-IR, on the layers model in the SE software: using this approach, see figure 6.19, the obtained results are more comparable with the ones of Schulze, suggesting a higher reliability of the U_E estimation. A confirmation of these values comes from [Bas10], where they measured the Urbach energy of a-SiC_y with photothermal deflection spectroscopy, obtaining values ranging between 70-170 meV. In our a-SiO_x:H samples the increase of E_U is observed as well with the oxygen incorporation, even though not linear as the figure 6.18: the trend is similar, and not surprisingly, to the voids plotted in figure 6.11. The error bars represent the *standard deviation*, showing that this indirect measurement is anyway accompanied by a not negligible uncertainty: for this experiment, 4 samples of each oxygen content were measured.

The discussion on the energy gap is reported in paragraph 6.1.4.

b. Average coordination number

The porosity of the amorphous silicon increases with increasing amount of incorporated O or C atoms: this result was evidenced in the previous paragraphs by the decrease of the refractive index, the increasing of voids and the broadening and spread over a wide range of imaginary dielectric function peaks. From optical tools it was possible to extract informations not just about the atomic contents, but also the structural compositions of the amorphous layers.

As reported by Janotta [Jan04], it is possible to quantify the amorphous state of the a-Si sub-oxide studying the average coordination number <r> of atomic bondings in the structural network. Therefore we consider the concept of *plucked network*. a-SiO_x:H is constituted by the two-valent oxygen, four and three-valent silicon atoms; <r> is expressed as ratio of the weighted atomic contents as follows:

$$< r >= \frac{4 \times c_{Si} - 1 \times c_H + 2 \times c_O}{c_{Si} + c_O} \ . \tag{6.1}$$

It has to be noted that this approach does not consider a possible presence of vacancy and defect states, depending on the deposition conditions, therefore it could result in some overestimation [Jan04].

However the plot shown in figure 6.20 can be seen as a structural phase diagram, as the increase of oxygen concentration causes the transition from *amorphous semiconductor* to a *semiconducting glass*. The decrease of the average coordination number

represents this phase transition, gradually approaching to the ideal value of <r>= 2.4 for network glasses. This finally confirms that the manufacturing of an a-Si alloy can lead to a more disordered, more porous and therefore more amorphous deposited layer. In the graph of figure 6.20 it is clear that all our samples take part to the globally linear decrease of this structural dilatation, even remaining quite far away from the *glassy* condition: the lowest <r> reached is around 3.7 . In the left side it is interesting to observe that the stack layers and also the <111> oriented wafers show a reduced coordination number, clearly indicating that these kinds of samples are more influenced from the same deposition conditions, and show a more disordered state. In the previous results it was observed that the <111> surfaces show a lower frequency of the Si-O-Si stretching mode, corresponding to a lower bond angle, hence to a different structural configuration.

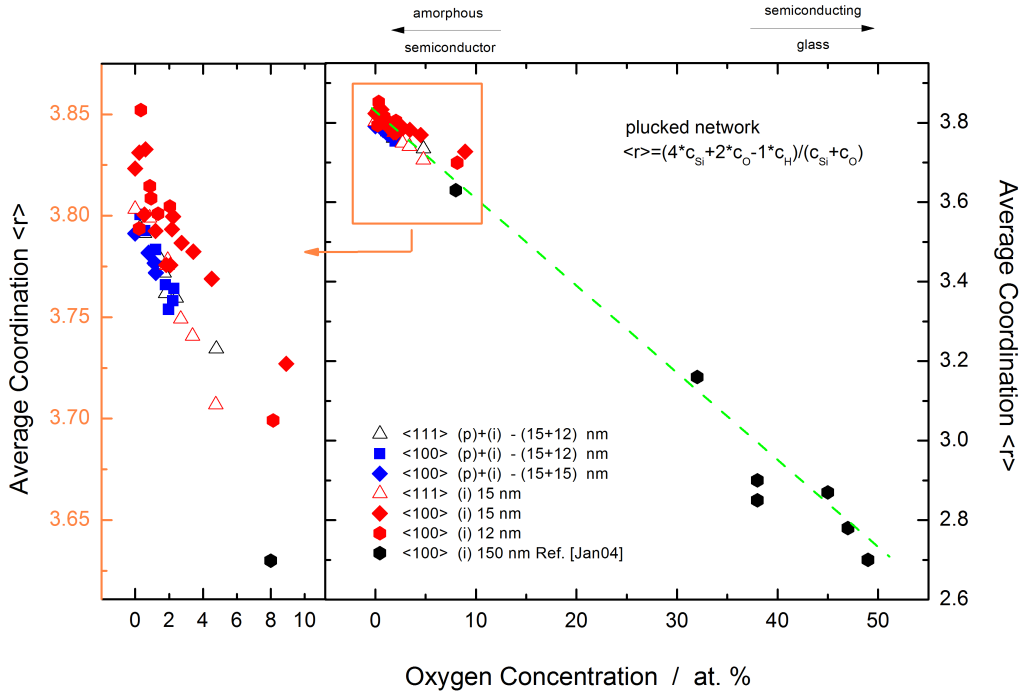

Figure 6.20: Phase Diagram in terms of the average coordination number <r>

Studying the correlation between the Si-O-Si frequency and the Average Coordination number for intrinsic samples of a-SiO_x:H, see figure 6.21, it can be noted that the <111> oriented layers reach clearly lower average coordination numbers: an explanation of this behaviour can be explained considering that as the <111> surfaces have a lower bond angle, i.e. a less dilated structure in the regions where oxygen is incorporated. This configuration could represent an unstable situation as the porosity of the layer increases for the suboxides. Therefore it can be hypothesized that the stability of the porous network is reached if the deformation due to the Si-O-Si wide bond is propagated in this case (on <111> surfaces) on the homo-nuclear Si-Si bonds, distorting more the global structure, incorporating more H (see fig. 6.10) and reducing the N_{Si} (see the voids of the (i) case in fig. 6.10) and so the average coordination number. Finally it can be concluded that the <111> wafers receive a more disordered and complex structure of a-SiO_x:H, even if not confirmed from the Urbach energy (see figure 6.18).

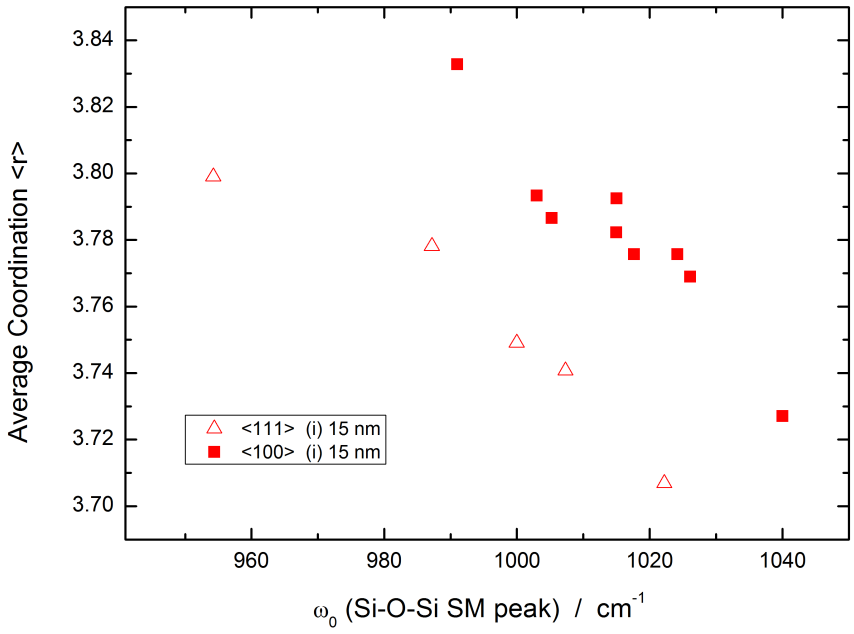

Figure 6.21: Average coordination number <r> as function of the Si-O-Si SM frequency

6.1.4 Tuning of layer transparency

As already outlined, the deposition of amorphous silicon suboxides and subcarbides lead to a less dense material, that causes a different dispersion of the electromagnetic radiation (reduction of the refractive index). When the light passes through the thin film but not leading to charge separation, it can also be absorbed, and this is a crucial point projecting a solar cell, as the *parasitic* absorption losses reduce the final current output and therefore the efficiency. The photons absorption is related with the electronic configuration of the semiconducting layer and its energy gap, which are varied including new atomic species in the deposition process.

In our specific case hydrogen and oxygen (or carbon) increases the band gap creating new molecular anti-bonding states (see chapter 3). To evaluate the energy gap, three different approaches of SE analysis were used:

- from Tauc-Lorentz (TL) model [Jel94], extraction of the energy gap from the *Tauc plot* individuating a distinct linear regime in the graph $\sqrt{\alpha \cdot h\nu}$ vs $\sqrt{h\nu}$ and determining the intersection between the straight line and the 0 axes;
- from TL model, extrapolation of the E_{04} from the absorption spectrum, that corresponds at the energy value when $\alpha = 10000\ cm^{-1}$;
- from Cody-Lorentz (CL) model, extraction of the Cody gap, using the same procedure of the Tauc Plot, but with $\sqrt{\epsilon_2}$ vs $\sqrt{h\nu}$, see [Fuj07b].

In the present analysis the energy gap from the *Tauc plot* was found to be overestimated (values over 2.2 eV) while the extrapolated Cody gap resulted not influenced

by oxygen (or carbon) incorporation because the CL model contains a large number of fit parameters that probably screen a variation of the energy gap: these *artifacts* caused to exclude these two approaches. Anyway the wide use of E_{04} in literature (see for example [Jan04], [Din13], [Ein12]) authorizes the evaluation with this particular optical gap.

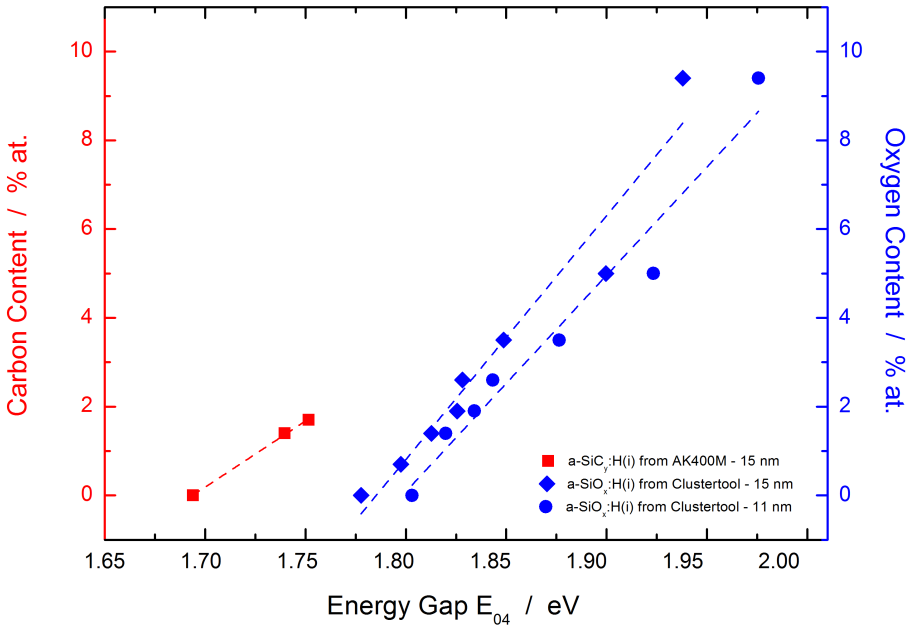

Figure 6.22: Optical gap E_{04} for a-SiC$_y$:H and a-SiO$_x$:H

Figure 6.22 shows the band gap obtained for the examined layers. As already mentioned, the heterogeneity of a specific alloy leads to an increase of the band gap: the oxygen and the carbon incorporation extend slightly linearly the gap of the respective a-SiO$_x$:H and a-SiC$_y$:H. Also, the distance between the two different trends does not surprise: the two batches come from different PECVD machines and from different processes (with a difference in table set temperature $\approx$ 100 K); as observed in the paragraph 6.1.2, a normal process in *AK400M* incorporate almost only half of the hydrogen than the *Clustertool* and the Si-H bonds contribute also to increase the energy gap.

The increase of the energy gap corresponds to a more transparent layer, as the parasitic absorption from the buffer layer is reduced. To analyse this phenomenon in our samples, a simulation of their optical behaviour was done with the free software OPAL. This tool allows to reproduce the optical properties of the front surface of a solar cell, giving as input parameters the thickness of the layers, the n and k values, and to obtain the wavelength-dependent reflection, absorptance and transmittance of each specific film, as described in [McI10] and [McI12]. In our case for the c-Si wafer tabulated values were chosen, while the thickness and the optical constants of the a-Si and ITO layers were extracted from SE analysis. To improve the output result (avoid the high reflectance and observe a concrete improvement in transparency) the front

surfaces were simulated as if they had a random pyramids texture, and furthermore the incoming light had an incident angle of 0°. From the overall spectra the software allows to obtain the current density losses J_{los} and the final J_{sc}. In figure 6.23 the J_{sc} is represented as function of the optical gap: it has to be noted that the short-circuit current density simulated for a c-Si wafer without a-Si passivating layers is $J_{sc} = 40.92\ mA \times cm^{-2}$; therefore the lower values plotted have to be referred to the *parasitic absorption*. This analysis is coherent with the results of Holman [Hol12], as found that only 30% of light absorbed in the intrinsic a-Si:H layer contributes to the short-circuit current.

Anyway the improvement in transparency for the a-SiO_x layer is as follows: by increasing the energy gap of the suboxide alloy less solar photons are absorbed in the buffer layers, hence a bigger amount of charge carriers can be created in the absorber wafer.

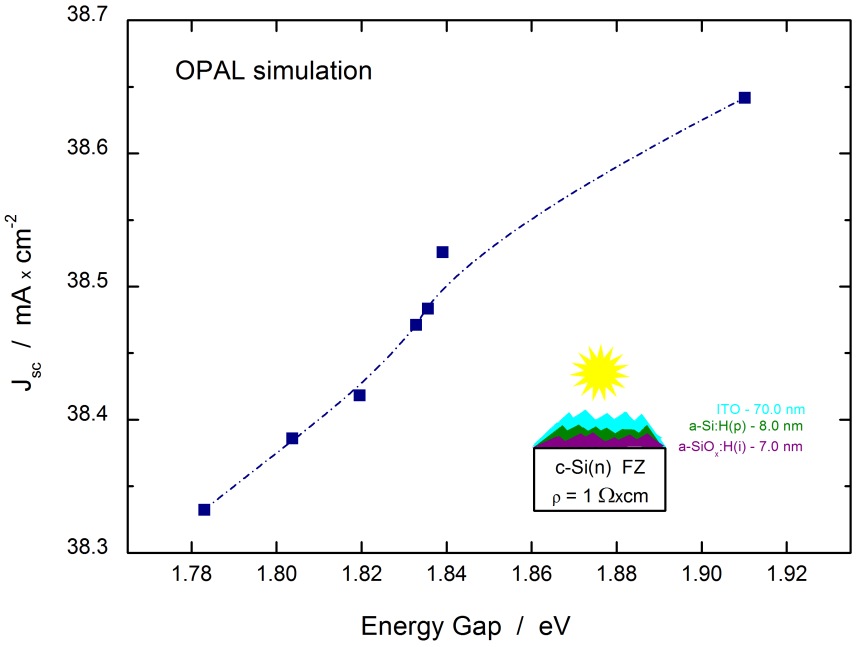

Figure 6.23: Short-circuit current density as function of the optical gap E_{04} for a-SiO_x:H, the line represents a guide to the eye

So it can be concluded that O_x incorporation can decrease parasitic absorption by $\approx$ 0.5 mA for 7 nm a-SiO_x:H, but in the range where it is still well passivating this is limited to maximum 0.3 mA.

A sketch of the simulated structure (with optical data from SE measurements) with respective thickness of each layer is reported together with the plot in figure 6.23.

Summary of the section 6.1

The experimental results of section 6.1, regarding the structural and optical properties of sub-oxide and sub-carbide a-Si layers, are here resumed.

- The *static refractive index* n_{IR} decreases as function of the oxygen or carbon incorporated in the *intrinsic* layer, suggesting that a-SiO$_x$:H and a-SiC$_y$:H represent a less dense layer than a-Si:H (for same thickness).

- The area of the hydrogen FTIR-peak related to the Si-H LSM decreases, while the one related to the Si-H HSM increases, with increasing incorporation of O_x and C_y. This occurred as a function of the CO_2 or CH_4 fluxes used in the deposition, confirming the results observed by Einsele for a-SiO$_x$ [Ein12], due to the high electronegativity of oxygen (or carbon) atoms.

- A new method to calculate the H, O_x and C_y content for a-Si layers from the FT-IR spectra was developed combining the Brodsky Cardona Cuomo analysis [BCC77] and the L-L relation, resumed in equation 5.15 . The H content was estimated directly calculating the absorption constant, using the BCC model: the <111> oriented wafers showed an higher hydrogen incorporation than the <100>, contrasting the results of Descodreus [Des11]. The oxygen content was estimated from the FTIR-peak Si-O-Si SM using the proportionality constant from [Ino95], and was observe to increase mostly linearly with the amount of CO_2 flux set for the deposition. The carbon incorporation was determined from the FTIR-peak Si-C SM using the proportionality constant from [Har10] and [vSw94]: this was possible by driving out the hydrogen by tempering; a good matching was observed with the measured quantities by Suwito using the SIMS [Suw11], supporting the assumption that no C effused during the tempering.

- The frequency shift of the Si-O-Si SM, as more oxygen is incorporated, was observed, revealing a higher mean-bond-angle dilated network and confirming the results of Einsele [Ein12].

- The voids content was calculated using the method of Smets for a-Si:H [Sme07], a almost linear growth is observed as function of the incorporated oxygen or carbon atoms, revealing an increasing of the porosity of the system and confirming what observed with the refractive index. Furthermore, the linear trend shown is characteristic of a *void-dominated* structure.

- The *stack* system of a-SiX(i) + a-Si(p) exhibited an higher hydrogen content, an higher refractive index and higher void percentage: these observations are partially contrasting with the results of De Wolf [DWo07]; a hydrogenation is suspected to occurr between the *i* and the *p* layers, in the so-called *surface interconnected voids*.

- The porosity of the thin film is strictly related to the structural disorder, that was measured extrapolating the Urbach energy parameter from the fit of the Cody-Lorenz model to the SE data. These obtained values are suspected to be overestimated (see figure 6.18), even though being in the same range of the recently measured energies (with the same technique) in [Ge13]. Therefore a

new method to improve the fitting procedure was proposed, that is modelling an *EMA* layer for a-SiO_x with the amounts of voids obtained from FT-IR (see figure 6.19). This procedure gave more reasonable values, showing always an increase of the Urbach energy - i.e. of the *long range disorder* - proportional to the oxygen incorporation.

- A phase diagram in terms of the average coordination number <r> was derived using the same approach of Janotta [Jan04], showing how the oxygen dilates the amorphous network (as <r> with O_x content, the average number of first neighbours atoms is reduced, then voids describe the residual empty space).

- An increase of the energy gap of the alloy layers, representing a more transparent system, was observed. An *Opal* simulation confirmed the higher transparency, with increased J_{sc} proportional to the oxygen incorporated due to reduced *parasitic absorption*.

6.2 Annealing measurements

The high-temperature stability is an important issue for heterojunction solar cells and particularly for amorphous silicon, for reasons already outlined in the first chapters.

To investigate the thermal stability of sub-oxides and sub-carbides a-Si alloys, isochronal annealing measurements (10 minutes each) were performed, increasing the temperature in a range from 180°C until 600°C with 7-8 steps. The samples were exposed to thermal stress using a hotplate at air ambient. After each tempering, the samples were characterized with SE, FT-IR, QSSPC or SunsV_{oc}.

6.2.1 Crystallization

The investigations in the previous paragraph already mentioned that the a-Si growth on crystalline wafer is not sharp, but it consists of an *interface* where the two structures co-exist and the amorphous silicon is partially epitaxial. When heating is stressing the thin film, this region represents the crossing-way for the transition from amorphous state to a crystalline configuration.

In more details, the imaginary dielectric function can be used to reveal this critical transition point stimulated by tempering. During the annealing the atoms constituting the mismatch amorphous/crystalline at the interface are subjected to a structural relax, causing a re-arrangement in a more compact and ordered state. The increasing of LRO distributions affects the height of the ϵ_2 peaks, for the same reasons seen in paragraph 6.1.3.

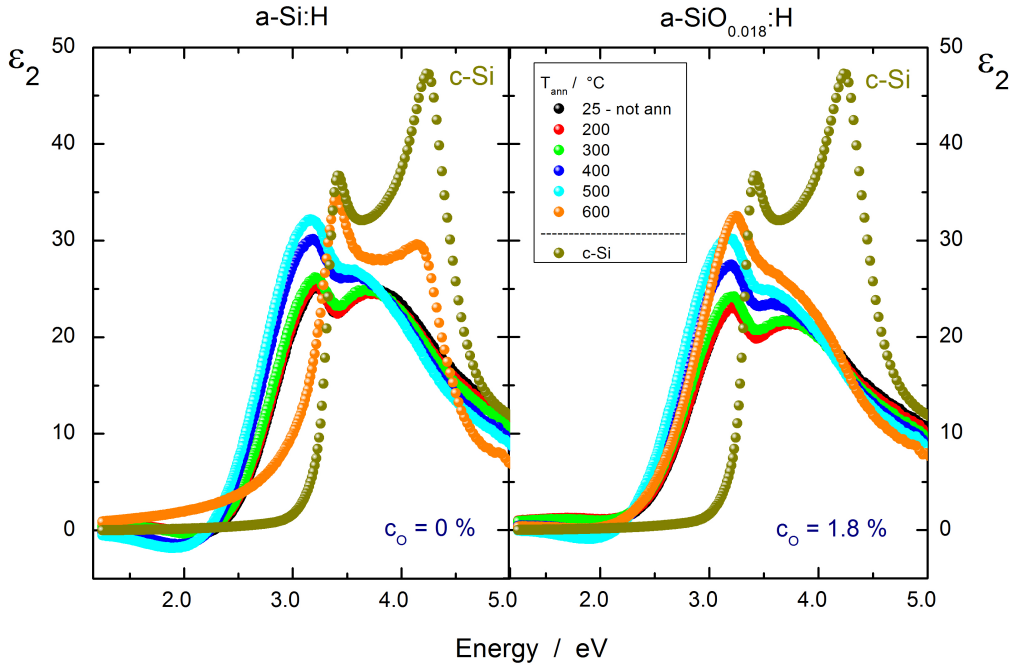

Figure 6.24: ϵ_2 spectra after annealing measurements of a-Si:H and a-$SiO_{0.018}$:H

Figure 6.24 shows the imaginary pseudo-dielectric function, obtained by SE measurements at each annealing step, for two intrinsic samples: a-Si:H and a-$SiO_{0.018}$:H, deposited with CO_2/SiH_4 gas flow ratio of %, resulting in 1.8 at. % of oxygen content. In

both graphs ϵ_2 of c-Si is reported from tabulated values, as crystalline reference. The peak positioned around 3.2 eV increases in height when annealed until 500°C, confirming the reduction of amorphous states, transformed in partial crystallite grains. This increase is also known in literature by [Los01]. The most interesting result appears at 600°C, where the normal a-Si:H clearly crystallizes: in the left part, the orange curve superposes the first peak with the one of the single-crystal reference. Furthermore, the presence of the second peak around 4.2 eV is related to the critical points in the joint density of states at <111> Brillouin Zone direction (see figure 5.6), meaning that a LRO is dominating the structural configuration. This can also be noted from the states decreasing under 3 eV. Conversely, the sample with oxygen does not show such a transition phase, and the 600° peak does not reveal a significant shift, as in this case the thin layer remains amorphous. The retarded crystallization is a consequence of the results discussed in section 6.1.3. It was observed that the oxygen (or carbon) bonding atoms increase the LRD of the amorphous network, resulting in structural voids and a more complex atomic arrangement. The alloy system is therefore more thermodynamically stable, as no collapse or crystallization of the structure is observed. Figure 6.25 confirms this conclusion, showing that all the sub-oxide alloys did not crystallize at 600°C. Similar results, not shown, were obtained for a-SiC$_y$:H layers.

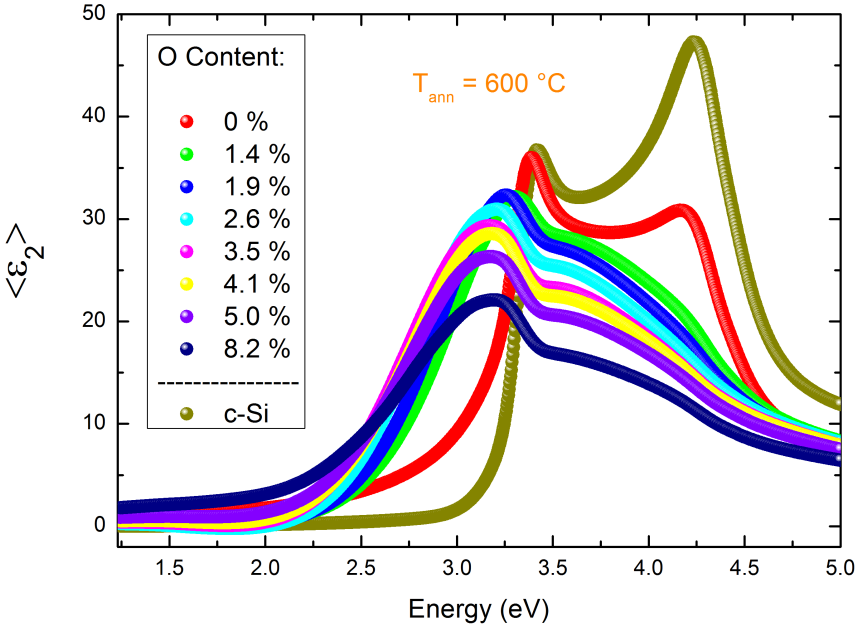

Figure 6.25: ϵ_2 spectra during annealing measurements of a-SiO$_x$:H

Therefore, increasing the oxygen content the a-Si layers have a more disordered configuration, but are also more stable to thermal stress. In figure 6.26 the first peak positions (in blue) and the heights (in red) of the respective dielectric functions, shown in figure 6.25, are plotted : only the sample deposited without CO_2 shows similar values like the crystalline reference after the annealing at 600°C. It is interesting to note that for $C_O \geq 3.5$ *at.* % the peak position is more or less constant, indicating that the disorder is dominating and no 'crystallization shifts' are induced by annealing.

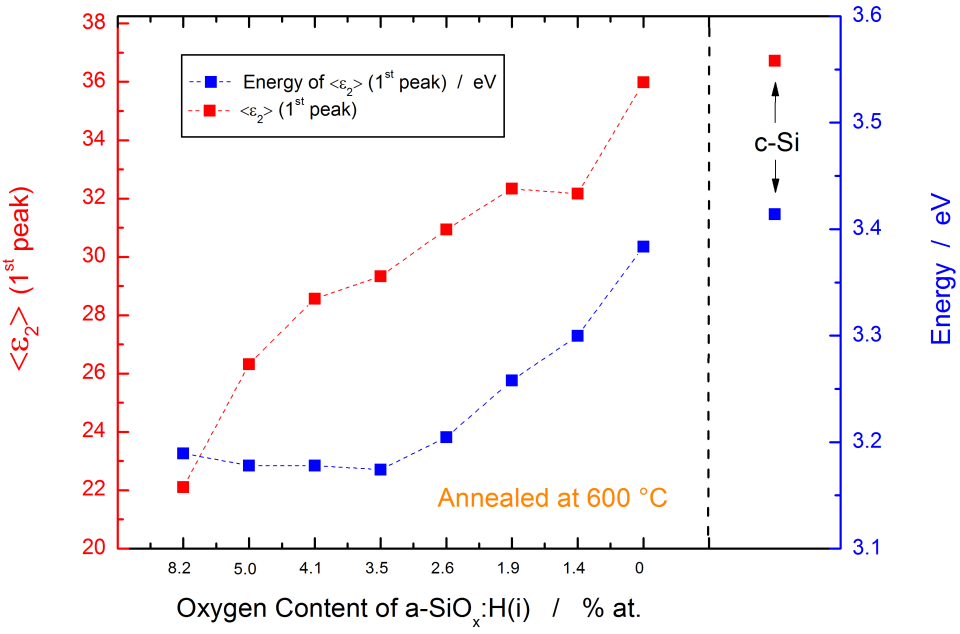

Figure 6.26: ϵ_2 peak energies (in blue) and heights (in red) of a-SiO$_x$:H

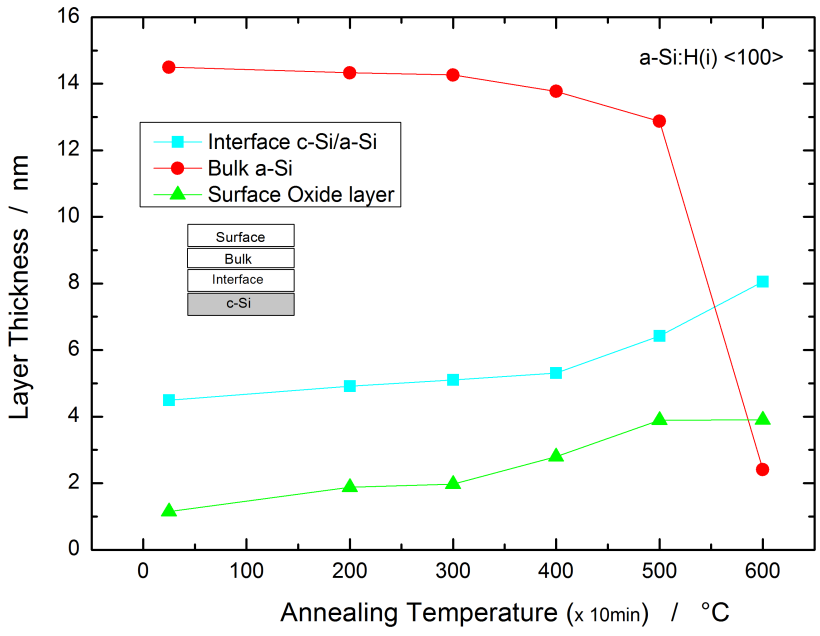

Figure 6.27: Interface, Bulk and Surface layer thickness of a-Si:H under annealing process

The study of the first peak position of the imaginary *pseudo*-dielectric function was made first for a-Si:H and μ-Si:H by Losurdo [Los03]. He observed a crystallization occurring when this value is roughly near to 38.0 . Our measurements, based on suboxide layers, can assume this value as crystallization reference as well.

The dielectric function gives an idea of the structural configuration. To have a more quantitative informations about the crystallization process it can be useful to observe how the measured thickness from SE is changing during the annealing.

Studying the thickness to monitor the crystallization is a technique already used in literature, see for example [Los01]. Figure 6.27 shows the thickness of the *interface*, the *bulk* and the *surface* layers of a-Si:H(i), using the model of figure 5.7b. It can be observed that the interface and the surface layer slightly increase during the several annealing steps: the interface, as already mentioned, represents the structural border with the crystalline wafer and this increases in a crystallization process, while the surface thickness is related to the oxidation due to the fact that the annealing measurement are performed at ambient air (this aspect will be outlined further in paragraph 6.4). Anyway the big drop of the *bulk* layer thickness clearly shows the transition from amorphous to crystalline, revealing a collapse of the thin-film structure.

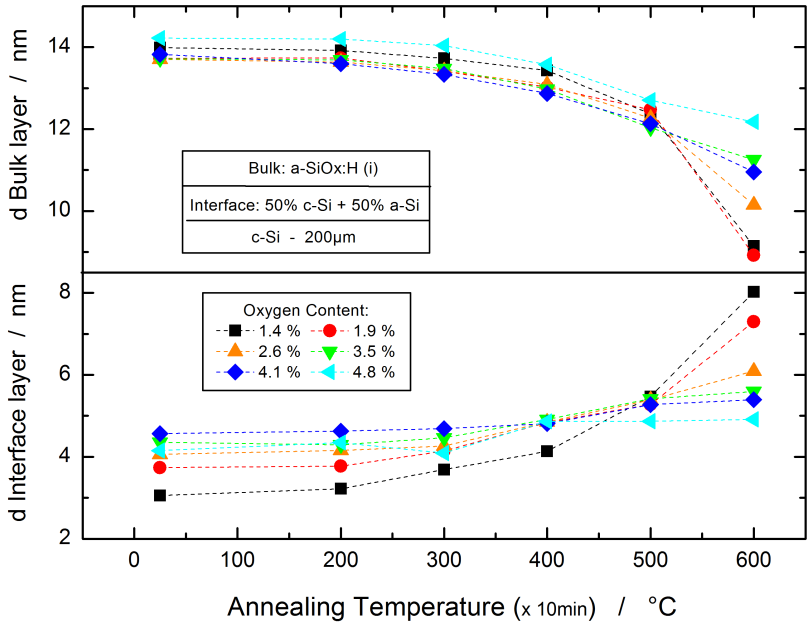

Figure 6.28: Interface and bulk thickness of a-SiO$_x$:H(i) samples under annealing

As expected, the thickness of the *interface* and *bulk* layers of a-SiO$_x$:H, plotted in figure 6.28, do not show the same trend of a-Si without oxygen. In these cases no big collapse is observed, and all the reduction of *bulk* specific thickness are mostly compensated from the increase of the *interface* layer. It is interesting to note that with $C_O = 4.8\%$ just a slight variation of 1-2 nm is observed and the layers are quite stable after thermal exposure.

All these discussions were related to intrinsic samples with <100> oriented wafers. Anyway the crystal orientation does not influence the induced crystallization, as same results were obtained with <111> planar samples.

6.2.2 Hydrogen effusion

Monitoring the hydrogen content using FT-IR spectra after each annealing step, allows to reproduce an H effusion experiment, that was widely used in literature to characterize a-Si:H layers (see for example [Sme07], [DWo07], [Ein12] and [Schu11]). Already at the beginning it is necessary to point out that evaluating the atomic content or the atomic effusion with an optical tool is not the same as using a mass spectrometer, hence the overall results obtained in this thesis have not the purpose to reproduce an exact quantitative estimation, but a general trend representing the variations of the species percentages inside the studied layers. In the following sub-paragraphs the H effusion FT-IR spectra of a-Si:H, a-SiO_x:H and a-SiC_y:H will be shown and discussed.

a. *Intrinsic*, *p-doped* and stack of a-Si:H

As considered in the previous paragraph, starting with the analysis of a-Si:H layers can help to understand the thermal behaviour of the alloys. In figure 6.29 the H effusion from the a-Si:H(i), a-Si(p) and from the stack i+p is shown. The black line represents a calculated mean value between the *intrinsic* and the p-doped layer, compared with the stack behaviour. The most evident result is that the p layer losses more hydrogen at lower temperatures than the *intrinsic* sample. This confirms the measurements of De Wolf in [DWo07]. The doping inside amorphous silicon induces a lower Fermi energy level, that was seen to be responsible of lower energy bonds of Si-H molecules. This weaker bonds (with respect to the *intrinsic* case) explain the fast H effusion, or fast decrease, observed in the doped layer. A further confirmation comes also from the effusion peaks observed by De Wolf, where the maximum hydrogen effusing is observed around 250°C and 400°C for a-Si(p) and a-Si(i), respectively: in our graph (figure 6.29) the big drop of N_H decreases are observed in the same temperature range as well.

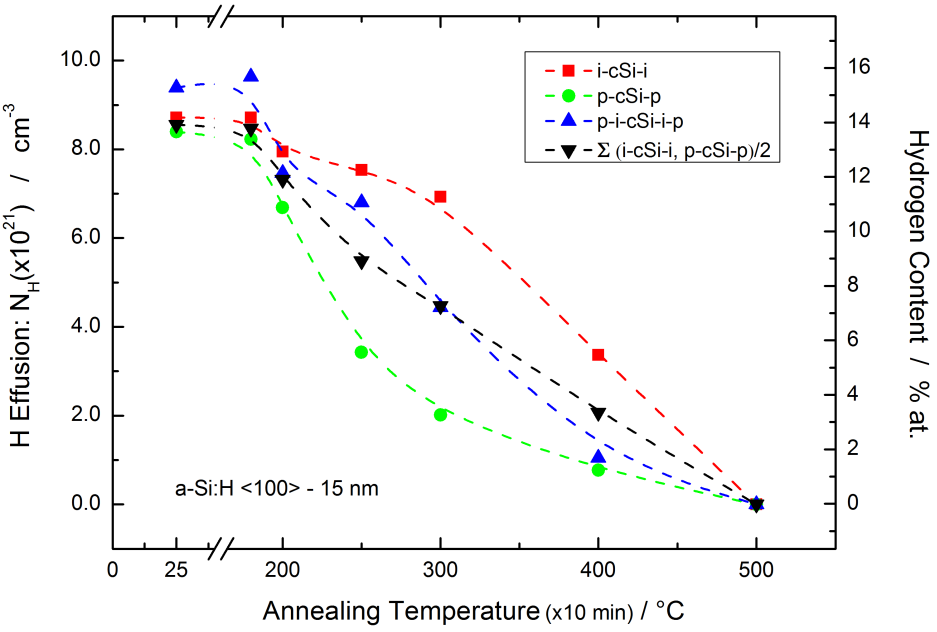

Figure 6.29: H effusion from a-Si:H *intrinsic*, *p-doped* and the stack

The stack shows a weaker H stability than the *intrinsic* case, and seems to have a trend not too far away from the mean value of the two single layers. De Wolf assigned this phenomenon to the shift of the Fermi-level (also in the i layer) induced by the top-deposited doped layer. In this work [DWo07], the H stored in the stack is reported to be smaller if compared to the sum of i and p, due to H effusion during the deposition of the p layer. In our case, we obtain a different result: the H content of the stack system is found to be higher than the single layers, as we have higher density values from the FT-IR measurements. As explained above, we attribute this presence to an hydrogenation between the two a-Si, which mainly occurred during the deposition of the p layer. The H at the i/p interface could be responsible of a general higher number of weak Si-H bonds, that can co-operate with the Fermi level shift, causing large H effusion. This interpretation is confirmed by the refractive index that is lower for the stack, indicating a less dense overall structure, and by the presence of voids. As observed previously a-Si:H (i or p) has a non zero percentage of voids; the *surface interconnected* voids of the *intrinsic* layer could receive the hydrogen atoms from the p post-deposition.

b. *Intrinsic* and stack layers of a-SiO$_x$:H

In the following analysis effusion spectra from i and from i+p samples with a-SiO$_x$:H and a-SiC$_y$:H will be reported. The motivation to study stack structures with alloys-based thin films is to reproduce a more realistic behaviour of a solar cell and to investigate the big influence of the H effusion on the double a-Si system.

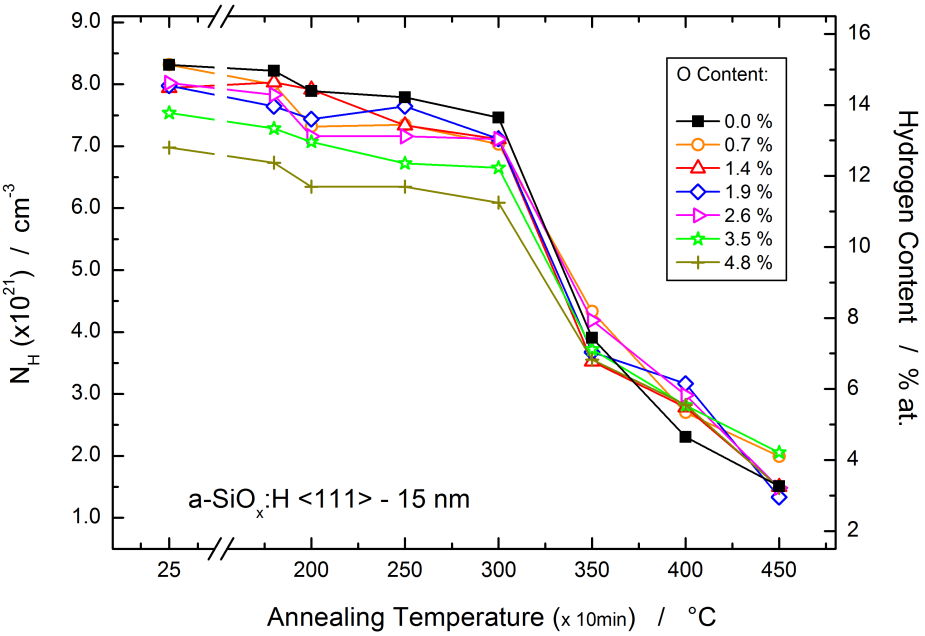

Figure 6.30: H effusion from <111> oriented a-SiO$_x$:H(i) layers

Since p layers lead to a stronger effusion of H compared to n layers as reported by De Wolf [DWo07], only i/p stacks and no i/n are investigated in the following.

The oxygen (or the carbon) inside the *intrinsic* layer to a crystallization ai higher temperatures and since Einsele [Ein12] reported a higher temperature stability for pure i layers, it is investigated how O_x incorporation improves the temperature stability of the stack system i/p.

The H effusion measured by FT-IR of a-SiO$_x$:H samples show similar spectra for <100> and <111> layers. To have a more exhaustive analysis, <111> spectra will be reported as N_H vs $T_{annealing}$, while for the latter case of <100> the HSM and the LSM contributions will be separated into N_H^{HSM}, N_H^{LSM} vs $T_{annealing}$.

Figure 6.30 shows the effusion spectra of <111> *intrinsic* a-SiO$_x$:H. It can be observed that for temperatures ranging under 300°C the values of H density remains quite constant, with a variation not higher than 1%. It is also clear how the oxygen content causes a decrease in the N_H. After 350°C it is possible to observe the big effusion drop, after which the H goes mostly linearly to 0 (with successive tempering steps). Einsele explained this by effusion through *surface interconnected voids* [Ein10a]. An explanation can be addressed to the fact that until 300°C the thermal energy is not enough to activate abundant effusion, and the unique microscopical behaviour is presumably an inter-diffusion of H species moving through structural voids or interstitially inside the a-Si and especially at the interface with the crystalline wafer. The presence of the oxygen seems to have a slight (not strong) improvement in the thermal stability: see for example the case at the 400°C.

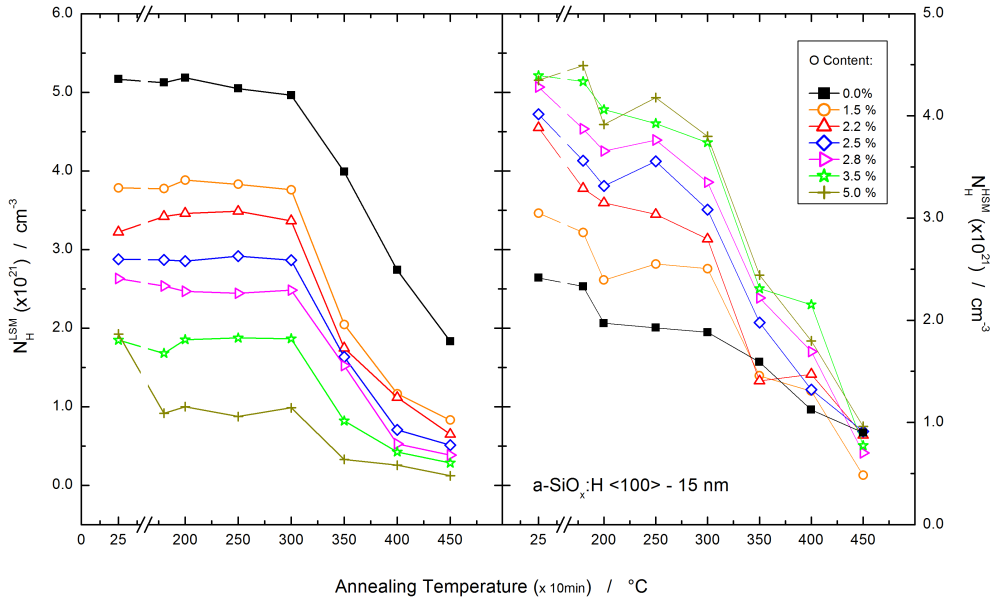

Figure 6.31: H effusion from <100> oriented a-SiO$_x$:H(i) layers, LSM(left) and HSM(right) contributions

The H effusion from <100> wafers, as said, show the same trend; anyway it is interesting to observe the variation of the LSM and the HSM during the annealing. In figure 6.31, until 300°C all a-SiO$_x$:H samples have a mostly constant behaviour while the high stretching mode is clearly more affected from the annealing: the minima and maxima

observed at 200 or 250°C can be related to inter-diffusion inside the voids because, as already observed, the HSM is representing Si-H bonding with oxygen back-bonding or in the closing area (enough to influence the dipolar surrounding). Considering the LSM of the sample with $C_O = 5\%$, the fast decrease at 180°C confirms the high porosity, and hence the easy effusion of the layer. After 300°, also in this graph, a general decreasing is observed. It is relevant that the two plots are quite symmetrical, where the LSM is dominating in samples without or with really low oxygen content, and the contrary happens for the HSM.

In the case of the stack, the effusion spectra show a constant decrease, as low thermal annealing (≈ 200°C) is able to activate the rupture of Si-H weak bonds, induced by the Fermi-level degradation. Also, the inter-diffusion observed in the low-range temperature of annealing, in these samples is totally superimposed from the effusion that is suspected taking place in the interconnected voids between the two a-Si layers.

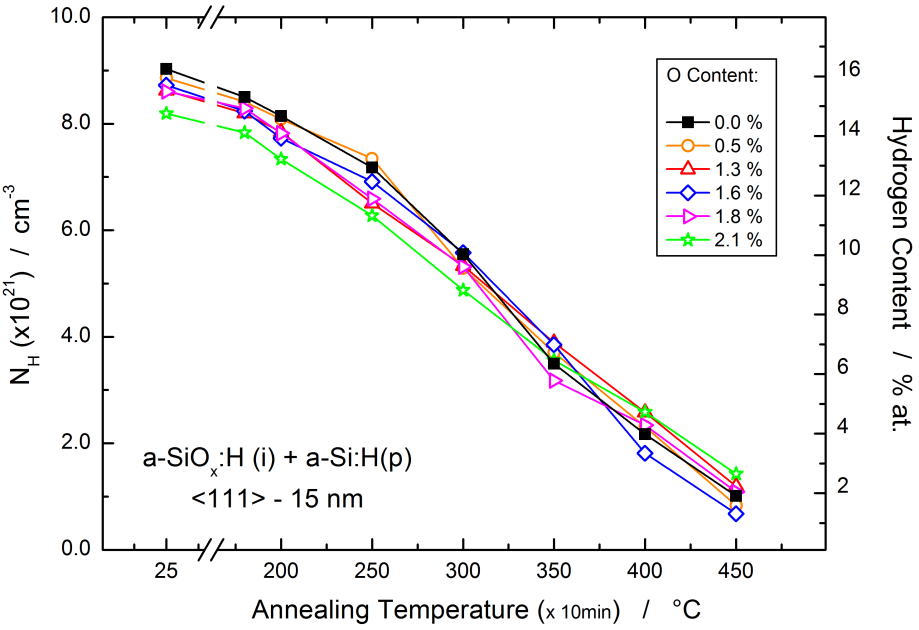

Figure 6.32: H effusion from <111> oriented a-SiO$_x$:H + a-Si:H(p) layers

Figure 6.32 represents a-SiO$_x$:H(i) + a-Si:H(p) on <111> wafers: no big discrepancy in the thermal behaviour is observed between the samples with the *intrinsic* a-Si:H and the sub-oxides alloys.

Figure 6.33 shows the LSM and the HSM effusion for the stack on <100> wafers: the symmetry is also in this case present, but it can clearly be noted that the inter-diffusion is not occurring inside the layers or at the interface with c-Si. A conclusion from these graphs is that the thermal stress induce a breakage of Si-H and the movement of H atoms in all directions. In the case of an *intrinsic* sample at T lower than 350°C, the H has the possibility to diffuse and saturate dangling bonds at the interface a-Si/wafer and remain there. In all the other cases H atoms effuse from the layers, due to high thermal energy transferred to the H^+ ions or/and to the presence of voids that facilitate the kinetics of this evaporation.

Now we make a last consideration about effusion from a-SiO$_x$:H layers: in the paper of Einsele [Ein12], the effusion spectra show quite different peak position of the maximum effusion during the annealing. This is due to the different deposition (our samples have $\approx$ 15% of H, when Einsele has $C_H \approx 10\%$) and the different annealing setup: indeed his procedure is based on a constant heating rate of 20 K/min, while we did experiments with separate annealing steps. Hence a straight comparison is difficult to establish. Anyway the effusion peaks at lower T for samples with more oxygen are mostly not observed in our layers (except the case for $C_O = 5\%$), although our structural considerations confirm that the material is transforming in a more porous state (increase of voids), that should facilitate a faster effusion. In figure 6.31 the sample with 3.5% of oxygen seems to have a faster decrease in the range of 200-300°C, but it is just a slight difference. Most likely, our FT-IR setup is not able to accurately identify such a faster effusion. Also, Einsele shows that these peaks compare after 400°, that is too far away for our case, because at this temperature most of the H detected by our spectra is in the range of 4-5 %.

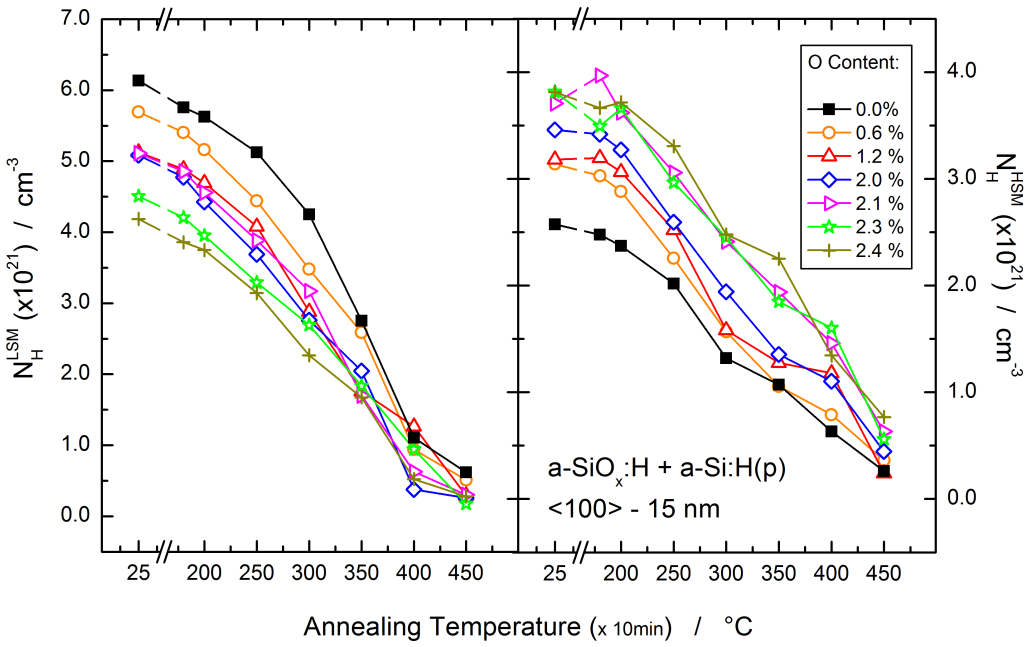

Figure 6.33: H effusion from <100> oriented a-SiO$_x$:H(i)+ a-Si:H(p) layers, LSM(left) and HSM(right) contributions

b. *Intrinsic* and stack layers of a-SiC$_y$:H

The deposition of a-SiC$_y$:H, as already mentioned, takes place in a different machine, the *AK400M*. A different deposition process can have consequences not just on the atomic contents of the thin films, but also on the thermal stability of the thin layers. The H effusion spectra are shown in figures 6.34 and 6.36, for the intrinsic case and for the stack, respectively. The results are compared with the effusion of an a-Si:H layer coming from the *Clustertool* (black line). The less H incorporation for layers deposited in *AK400M* is clear from the different scale positions of the curves. For the *intrinsic*

case it is evident that the H effusion starts after 300-350°C, but no big decrease are observed in the sub-carbides alloys, meaning that the thermal stability is higher for samples coming from this different machine.

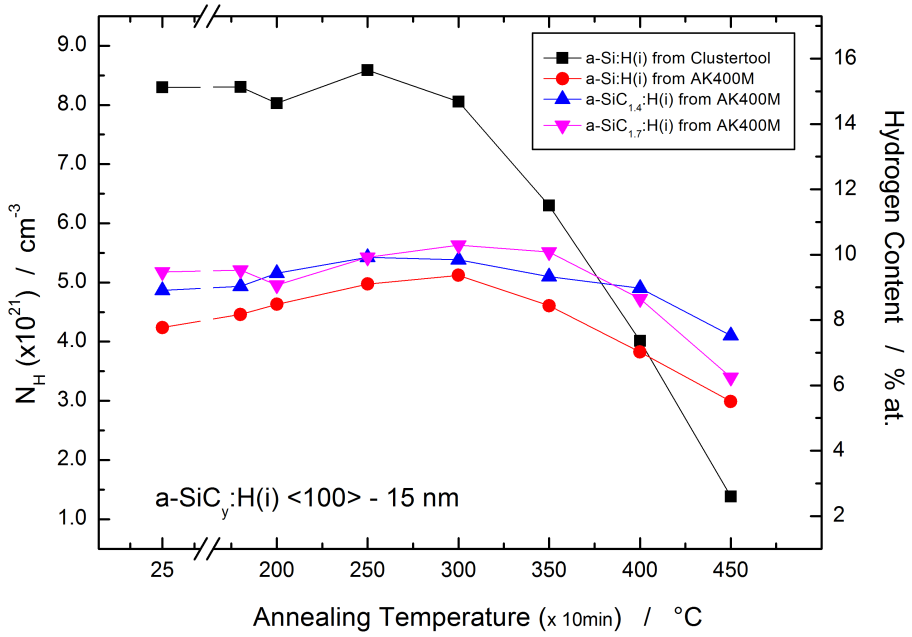

Figure 6.34: H effusion from <100> oriented a-SiC$_y$:H(i) layers

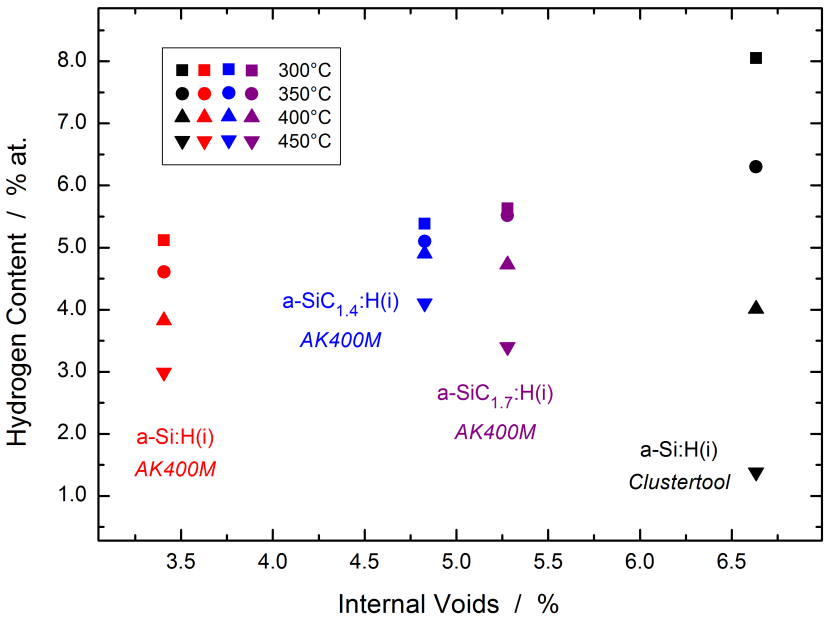

Figure 6.35: H effusion vs voids content for <100> oriented a-SiC$_y$:H(i)layers

Also, the slight increase of the C_H in the steps until 300°C is remarkable, clearly indicating an inter-diffusion of H ions inside the interface, saturating an higher number of dangling bonds. A comparison between H atoms and vacancy defects will be done in the following lifetime paragraph (6.2.4). The process occurring in the *Clustertool* is suspected to create more Si-H weak bonds, that easily break up after 300°C, and at 450°C the a-Si:H black curve definitely shows the higher H content loss.

An explanation for this observation is the different voids content of the samples deposited with *AK400M* and with the *Clustertool*: in figure 6.35 the hydrogen effusion during high T annealing steps is shown (from 300°*C* to 450°*C*) as function of the internal voids. It has to be clarified that no voids estimation, as explained in paragraph 5.1.4c, was made for layers after annealing, because the decrease of the hydrogen could bring the non-physical result of an increase of Si atomic density; therefore the values of voids percentages measured after depositions, already shown in figure 6.11 and 6.15, are assumed to be constant after tempering as well. This assumption is obviously valid in all the steps where no crystallization occurred, as shown in paragraph 6.2.1 .

Looking back at figure 6.35 it seems quite clear that the plasma deposition due to the *Clustertool* creates a more porous amorphous thin film that has a direct influence in the weakness of the Si-H bonds and of the hydrogen losses during the annealing.

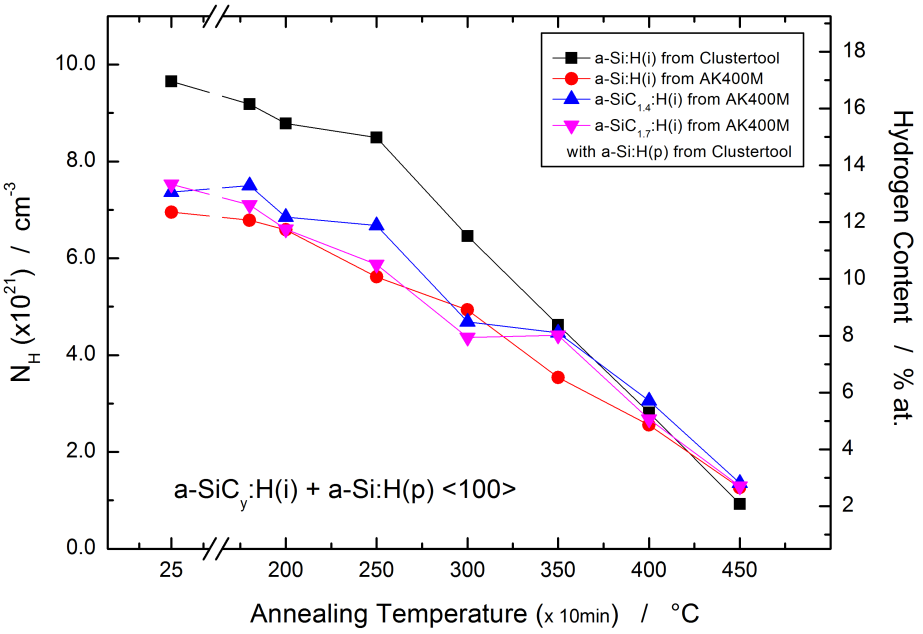

Figure 6.36: H effusion from <100> oriented a-SiC$_y$:H(i) + a-Si:H(p) layers

The sample with the stack (i+p) have the *p* layer coming from the *Clustertool* as well. It is interesting to note that, although the higher thermal stability of the sub-carbides alloys *intrinsic* layers, the shift of the Fermi-level occurs also in these samples and the general trend is quite similar to the stack coming from the *Clustertool*. Therefore, combining layers from different machines, figure 6.36 clearly confirms that the shifting of the Fermi-level position increase the Si-H weak bonds in all the considered system, leading to a constantly increasing effusion.

To conclude this sub-paragraph, considering just the three samples from the *AK400M*, also in this case the carbon has a slight improvement in the thermal curve, not easily distinguishable as the path of the different layers is quite similar; anyway in figure 6.36 it can be observed that the constant decrease shown from normal a-Si:H (red curve) is not exactly reproduced from the other 2 samples (a-SiC$_y$:H), that conversely show a slower H decrease, always inside the limits of our characterization set-up.

6.2.3 QSSPC measurements: lifetime and iV$_{oc}$

The hydrogen inter-diffusion and effusion suggests that the passivation of the amorphous silicon has several changes during the annealing (as was outlined in chapter 2, the H is the passivating specie). Especially, at high T, due to the abundant effusion, a strong degradation is suspected to take place: this phenomena will be investigated with the life-time measurements.

1. *Intrinsic* layers of a-SiO$_x$:H

The life-time behaviour of the sub-oxide *intrinsic* layers, as function of the annealing temperature, is shown in figure 6.37, for wafers with <100> orientation.

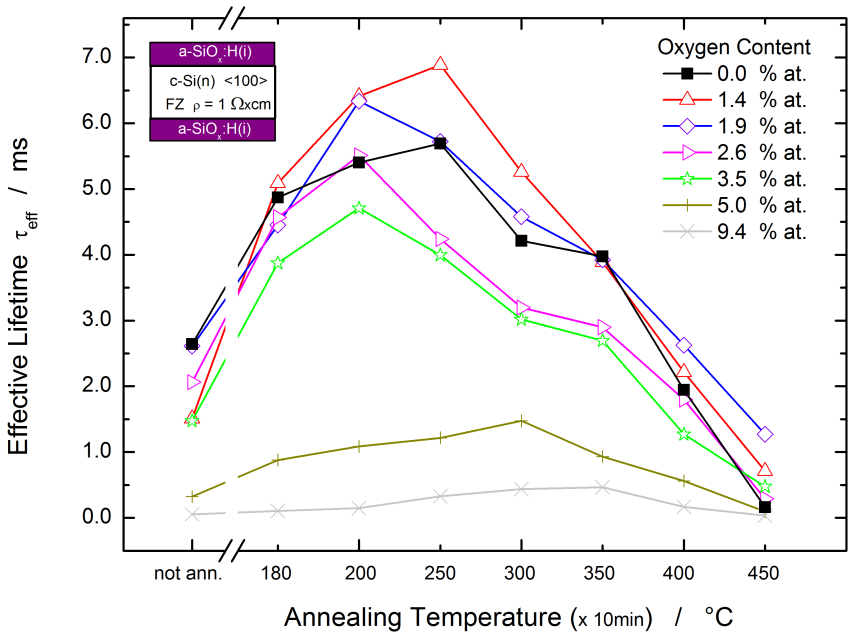

Figure 6.37: Lifetime of a-SiO$_x$:H(i) layers on <100> wafers

The general parabolic trend confirms the results obtained by Mueller in [Muel10] and by Einsele in [Ein12].

Until 200-250°C, the inter-diffusion of the H (partially observed with the FT-IR) causes a restoration of the non-saturated DBs at the interface with the crystalline silicon. This is a confirmation that, after the Si-H rupture, the H goes in all the possible (radial) directions; and also, at this range of tempering the effused quantity would be

neglected in comparison with the inter-diffused amount, that increases the lifetime of the photo-generated charge carriers. At 300°C, the effusion becomes dominant, as predicted by FT-IR spectra (see figure 6.31), and hence the loss of passivation is resulting in a constant decrease. As observed by Einsele, a high amount of oxygen degrades the material, due to the large porosity of the layers: the voids (seen in the structural investigation) increase the density of DBs inside the a-Si and also favours the thermal effusion. It is quite clear that in the samples with $C_O \geq 5\%$, the inter-diffusion slightly takes place until 300°C, but evidently the density of defects to saturate is definitely higher in comparison with the H stored in the layer. An other aspect, is that under 2% of Si-O molecules the highest results of life-time were reached due to the presence of the oxygen, indicating that such a low oxygen content can favour the saturating inter-diffusion. An other reliable hypothesis is that small amounts of oxygen can suppress the epitaxial growth at the interface [Fuj07b] and still do not increase the defect density too much. Samples with 2.6% and 3.5% show a lower tendency respect to the normal a-Si:H (black curve). Again, these overall results seem consistent with the effusion spectra of figure 6.31: good passivation is observed when the amount of incorporated oxygen does not affect too much the LSM (related to passivation). When the HSM becomes highly dominant, and hence the distribution of Si-H molecules are more affects in the dipolar surrounding from the oxygen atoms, lower lifetime results are observed. This analysis is confirmed by Einsele [Ein12], although the different C_O percentages related to the effective lifetime observed by us are most likely depending on the different deposition process.

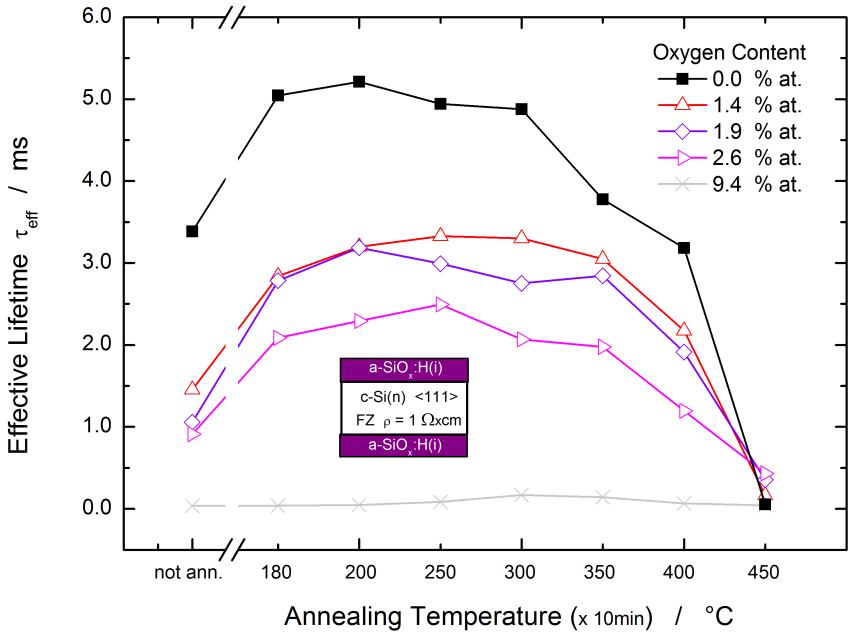

Figure 6.38: Lifetime of a-SiO_x:H(i) layers on <111> wafers

Finally, it can clearly be seen that at 400°C and even more at 450°C the normal a-Si:H has a higher degradation in comparison with the samples having low oxygen content.

Figure 6.38 shows the lifetime results for a-SiO_x:H layers deposited on <111> oriented surfaces. The crystal orientation clearly affects the passivation in samples with

incorporated oxygen, and not the same results for <100> are reproduced. For this kind of wafers the FT-IR results (see figure 6.8) showed a different configuration of the Si-O-Si molecules: the lower stretching-frequency was correlated with a smaller bonding angle. Pointing to this aspect, it can be supposed that the thermally stimulated inter-diffusion is more impeded in the sub-oxide alloy. The amorphous silicon, in its structural state, should not have a particular orientation-dependency; however, the presence of the partially crystalline interface (see the SE characterization) suggests that the orientation of the wafer can act as guide-line to the entire amorphous layer, as the SRO and the LRD are configured. Also, it has to be noted that the normal a-Si:H has a similar behaviour with the one seen in figure 6.37, and no improvement of passivation, as done by Descoedres in [Des11], was observed using <111> wafer. A possible explanation is a lower suitability of our deposition process (or even the cleaning step) with these particular surfaces. Anyway a degradation with high oxygen content is reproduced also in this measurement.

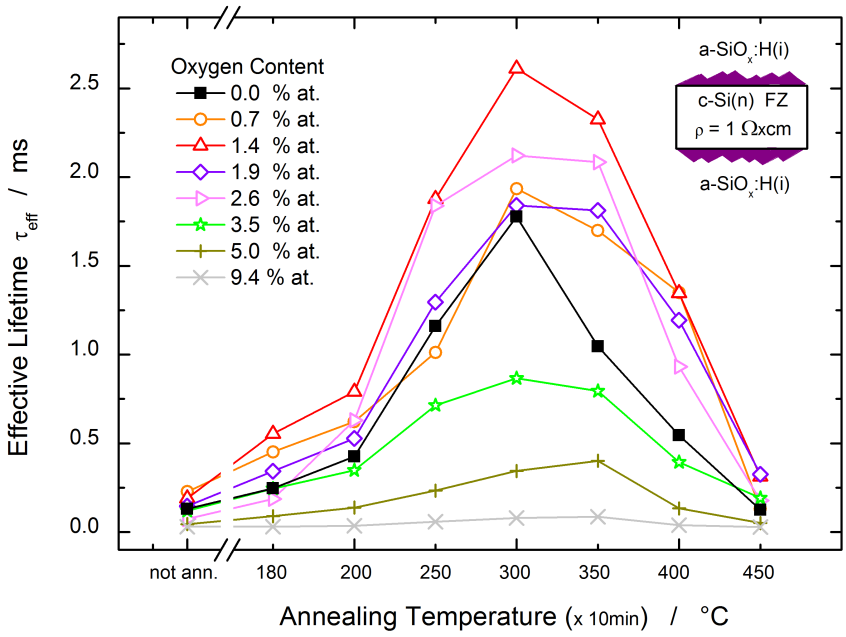

Figure 6.39: Lifetime of a-SiO$_x$:H(i) layers on texturized wafers

QSSPC measurements on *intrinsic* texturized wafers are shown in figure 6.39. In this case the general results observed for <100> planar surfaces, i.e. the passivation improvement with low oxygen content, the degradation at high C_O and the higher stability at 400 and 450°C are reproduced in this scale. The growth of a-Si on these wafers has a quite complex behaviour, that is still under discussion.

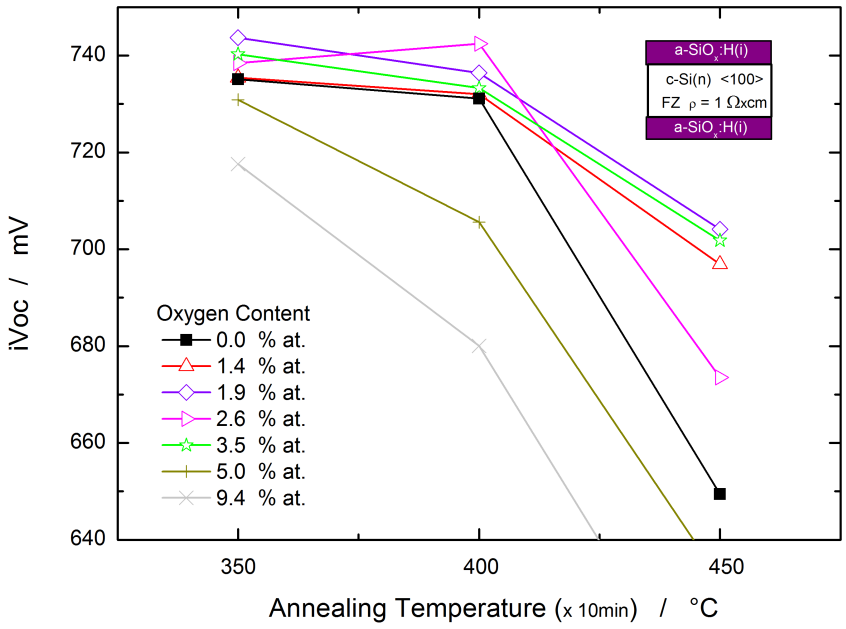

Figure 6.40: iV$_{oc}$ of a-SiO$_x$:H(i) layers on <100> wafers

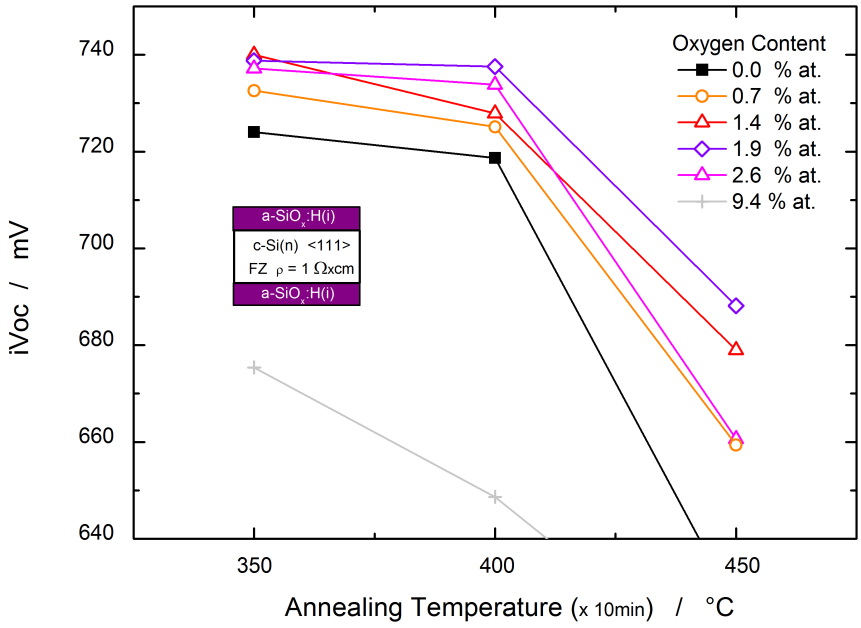

Figure 6.41: iV$_{oc}$ of a-SiO$_x$:H(i) layers on <100> wafers

The *implied* V$_{oc}$ calculated from the same QSSPC measurements can give an idea of the consequences of this passivation results on a solar cell. Figures 6.40 and 6.41 show the *i*Voc results in the annealing range 300°C-450°C for <100> and <111> planar samples. With this measurement it is even more clear that the improvement of the

low incorporated oxygen, especially at the degradation that affects the normal a-Si:H (black points) at 450°C is clearly reduced in the wafers with sub-oxide alloys. Also in this case, high oxygen content show abundant and fast degradation. All the results are plotted with a reasonable range, since values under 640 mV are not suitable for a solar cell production.

2. Stack layers with *intrinsic* a-SiO$_x$:H

The stack system give different and lower life-time results due to the already discussed fermi-level dependent defects, as the *p-doped* top layer creates more recombination centres shifting the fermi-level of the system i/p. Coherence between the H effusion and the QSSPC measurements is expected, for the same reasons outlined by De Wolf in [DWo07]. The abundant H losses observed in the FT-IR spectra suggest a reduced passivation during the annealing steps.

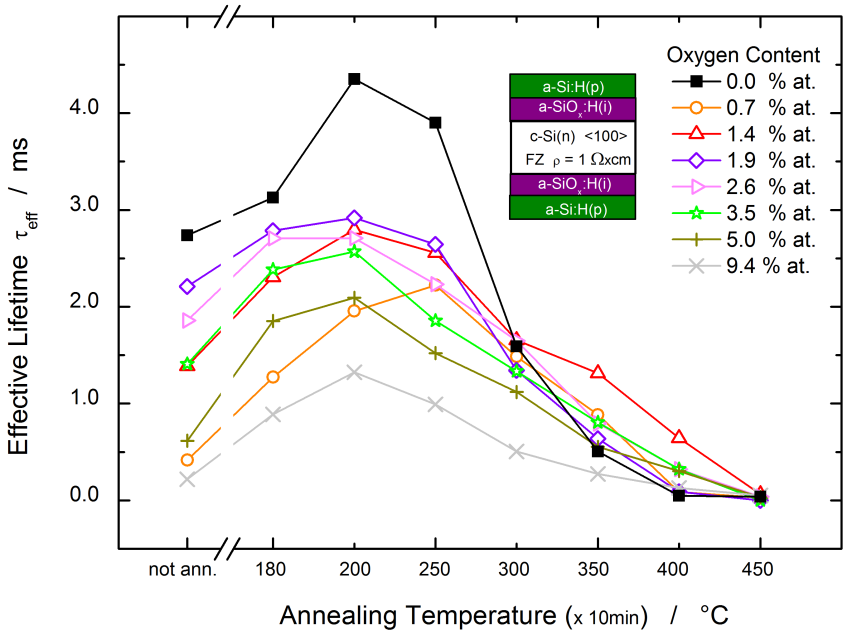

Figure 6.42: Lifetime from the stack a-SiO$_x$:H(i)+ a-Si:H(p) layers on <100> wafers

In figure 6.42 the lifetime results are shown for <100> planar wafers. As expected, lower results are obtained in comparison with the ones of figure 6.37. Also, not the same improvement are observed when incorporating oxygen in the *intrinsic* layer: until 300°C the sample without any oxygen has evidently more saturated DB. A possible explanation for this behaviour can be a better suitability between i and p layer both without oxygen, further investigation is necessary. In the last annealing steps anyway it is possible to distinguish the improvement of the sub-oxides alloys, as the normal a-Si:H degrades more and faster.

Similar results, shown in figure 6.43, are obtained on <111> oriented surfaces, indicating that the *doped* layer on top acts in the same way on different orientations. Therefore, also on texturized wafers (see figure 6.44), an analogous trend is obtained

(only one sub-oxide layer, with C_O = 1.4%, showed a better passivation quality). However, the thermal stability for T≥350°C is clearly increased for samples with oxygen incorporation.

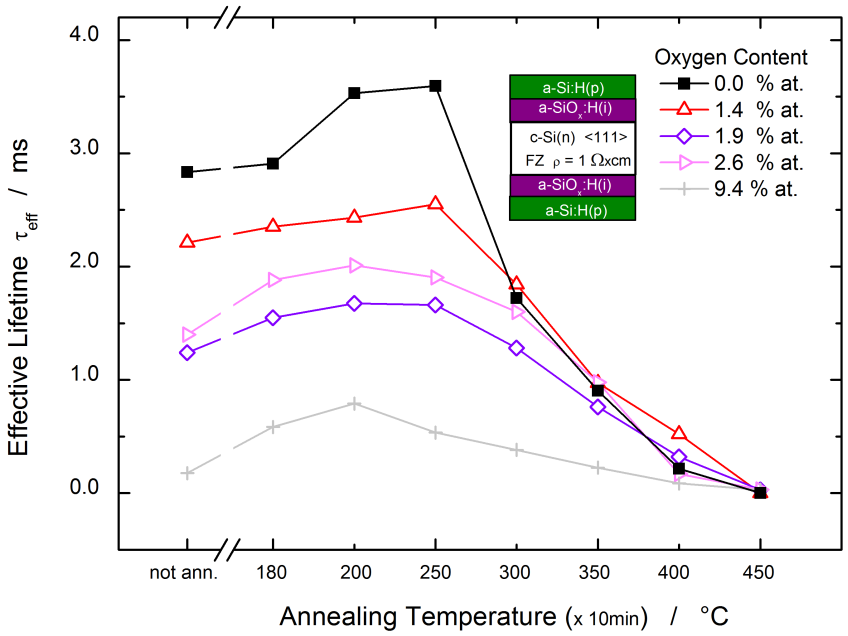

Figure 6.43: Lifetime from the stack a-SiO$_x$:H(i)+ a-Si:H(p) layers on <111> wafers

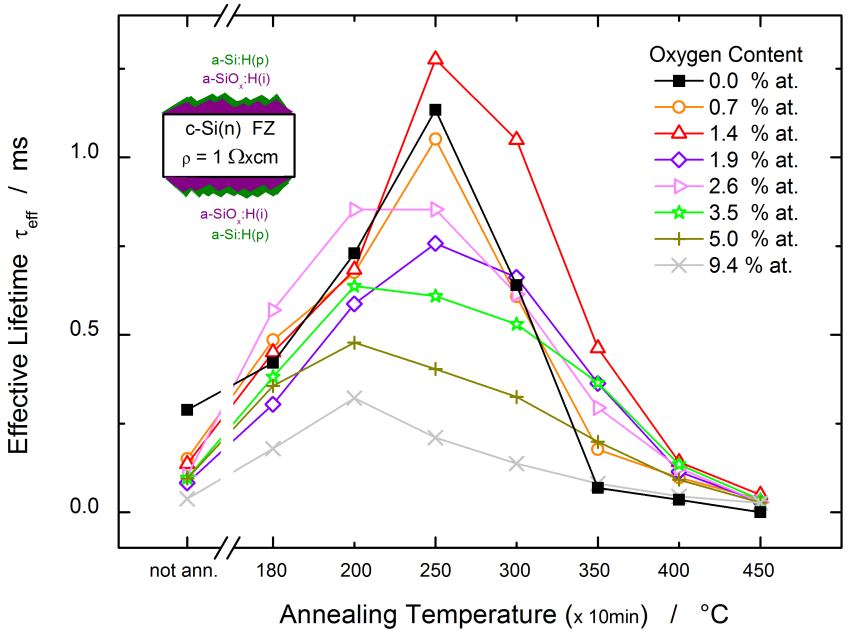

Figure 6.44: Lifetime from the stack a-SiO$_x$:H(i)+ a-Si:H(p) layers on texturized wafers

The correspondence with the H effusion results can be noted in the temperature position of the lifetime peak, where it is evident that the i layers of the previous paragraph reveal a maximum at 300°C while the stack system has its maximum commonly at 250°C, meaning that the anticipated effusion in this latter case is correlated with a fast thermal de-saturation of the Si DB.

3. Sub-carbides passivation layers

The incorporation of carbon gives improvements on the passivation quality of amorphous silicon, as was already observed in literature [Suw11]. Therefore an analysis of lifetime measurements subcarbides is shown in the following.

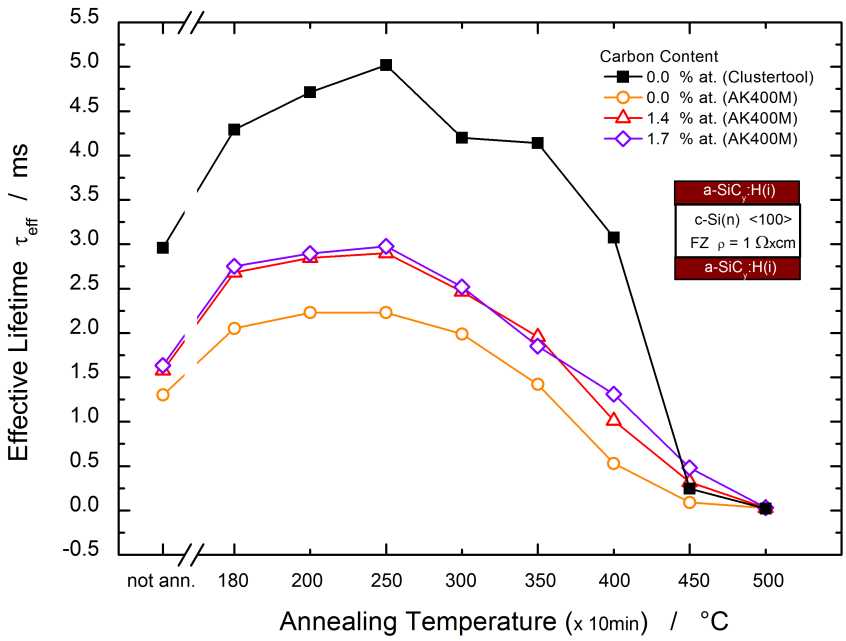

Figure 6.45: Lifetime from a-SiC$_y$:H(i) layers

Coherently with the effusion spectra, the H incorporated from the Clustertool is really higher (around twice the density) than the one from the AK400M; hence all the results are shown with a Clustertool reference a-Si:H. In figure 6.45 the lifetime results are illustrated for i layers of a-SiC$_y$:H, on <100> oriented wafers. The good matching with FT-IR spectra can be found considering that also the lifetime of the sample from the Clustertool is around the double of the one of samples from AK400M. Considering only this latter case, the better passivation due to the carbon is quite evident. Again, analogous observations were made on the stack systems, see figure 6.46. It can be seen that at high annealing temperatures ($>$ 400°C) the passivation quality of the subcarbides alloys is even better than the sample from Clustertool, clearly showing that the degradation occurring in an a-Si layer can definitely be reduced incorporating this kind of alloys. The improvement of carbon atoms in the amorphous network confirm the results of Suwito [Suw11].

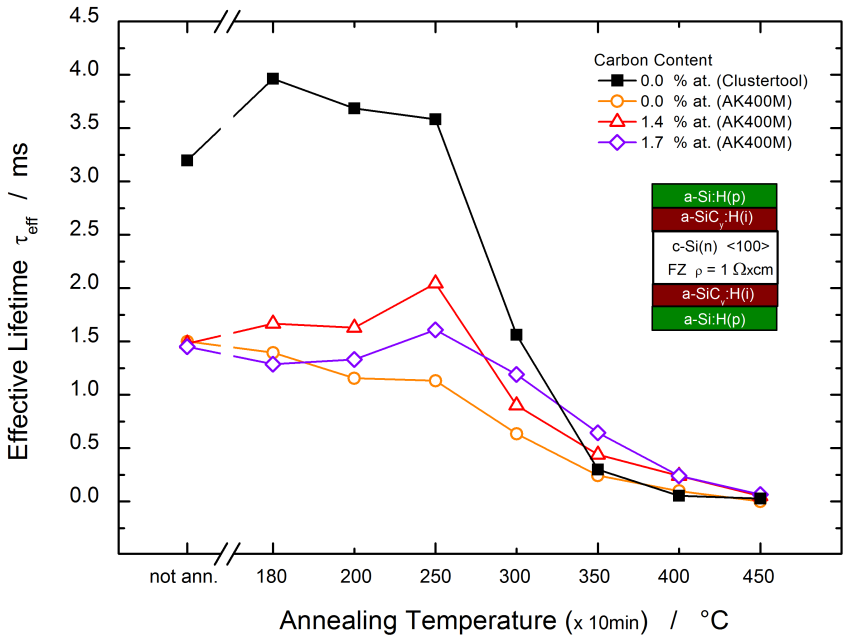

Figure 6.46: Lifetime from the stack a-SiC$_y$:H(i) + a-Si:H(p)

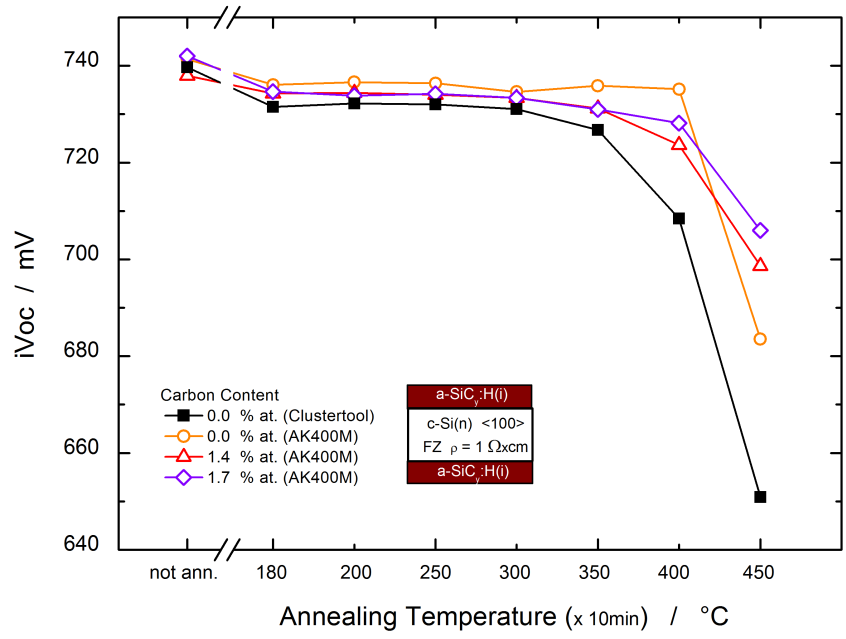

Figure 6.47: iV$_{oc}$ from a-SiC$_y$:H(i) layers

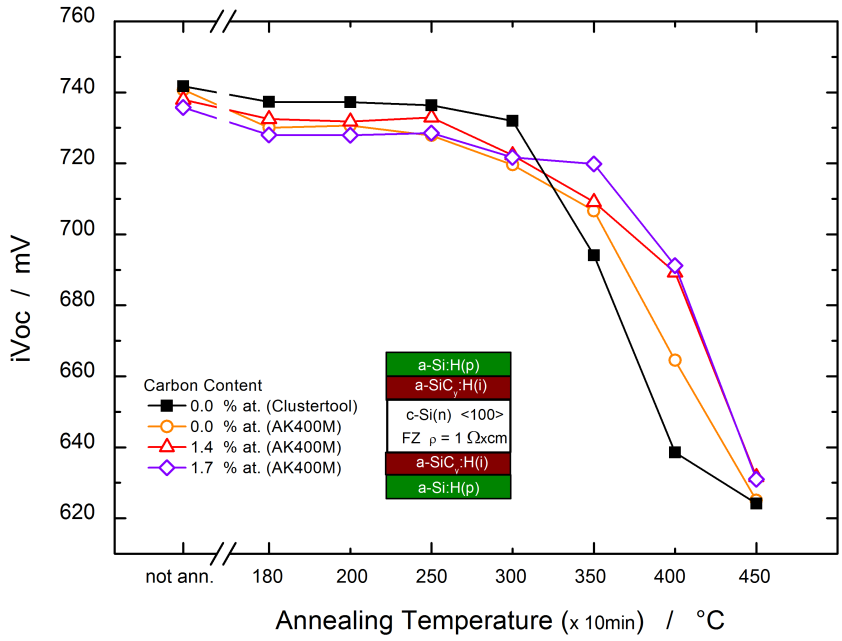

Figure 6.48: iV$_{oc}$ from the stack a-SiC$_y$:H(i) + a-Si:H(p)

The *implied* V$_{oc}$ results are reported for these samples as well, for i and i+p systems in figures 6.47 and 6.48, respectively. In both graphs the beneficial effect of the alloy at high annealing T is quite evident. The physical explanation of this result is the higher compactness of the amorphous structure when an alloy system is the basis of the entire layer, as observed from the several investigations of previous paragraphs. H escaping is reduced because C (or O) atoms modify the electrical surrounding in a way that the density of strong bonds Si-H is increased in the overall layer, and especially at the interface with the c-Si. Therefore the thermal stability results with the presence of these strong bonds that correspond to constantly saturated DB, even at high temperatures (T $\geq$ 350°C). The iV$_{oc}$ and the lifetime observations confirm this analysis.

4. SunsV$_{oc}$ results

The PECV deposition of a-Si layer is not always a stable process, and the reproducibility of the results is an important issue, especially regarding the passivation properties of these thin films. This aspect will be further outlined in the paragraph 6.4; however at this point the next results will be presented.

The incorporation of the oxygen inside the *intrinsic* layers was observed until now (especially at high T) to result in a slightly reduced thermal degradation. SunsV$_{oc}$ measurements were performed to obtain a voltage output indicating the passivation quality of the amorphous silicon. Figure 6.49 shows the SunsV$_{oc}$ results obtained for samples having the stack a-SiO$_x$:H(i) + a-Si:H(p) + ITO on the front side, and the same structure with a n-layer on the back side, to form a BSF. For this measurement 5 samples for each variation (texurized and planar, CO_2/SiH_4 = 0-0.35 %) were used.

The trend reproduces the observation made on iV_{oc} from the QSSPC data: a quite constant value for tempering under 300°C (in the texturized samples an inter-diffusion occurs) and a fast decrease in the last annealing steps. The improvement of the oxygen in this case in not observed, as at high temperature the samples with $C_O = 1.4\%$ showed a faster degradation than normal a-Si:H (black points). Only in the texturized case, at first annealing steps, the oxygen seems to improve slightly the Si DB saturation. These result can be addressed to the instability of the deposition process, as mentioned above. So further examinations are necessary. Anyway, as compared to prior samples these measurements showed that the external voltage is dropping in the same way as the iV_{oc}. In other words, it is clear that the goping efficiency is not affected by annealing, but the passivation is. The degradation due to the H effusion is therefore observed with this other opto-electronic tool as well.

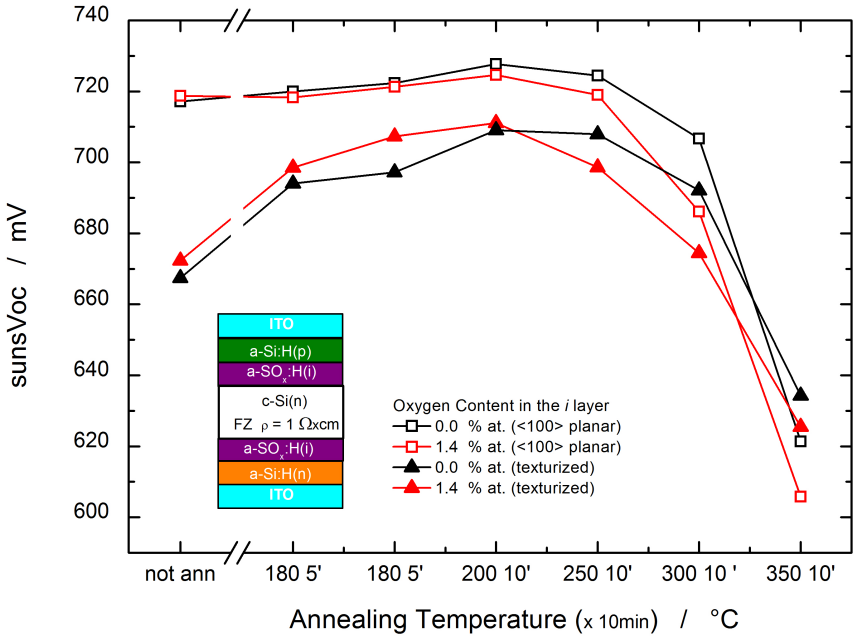

Figure 6.49: SunsV_{oc} results from the stack a-SiO$_x$:H(i) + a-Si:H(p)+ITO

6.2.4 Optical behaviour after annealing

The structural variations occurring during the thermal annealing have consequences on the optical properties of the a-Si layers. Until now the characterization has shown that the tempering induce partial crystallization, H effusion and degradation of passivation, phenomena depending on the specific a-Si layer under consideration. Using the spectroscopic ellipsometer measurements, it is possible to study the thermal behaviour of the refractive index and of the energy gap, in order to predict a different reaction of the annealed material to the incoming radiation.

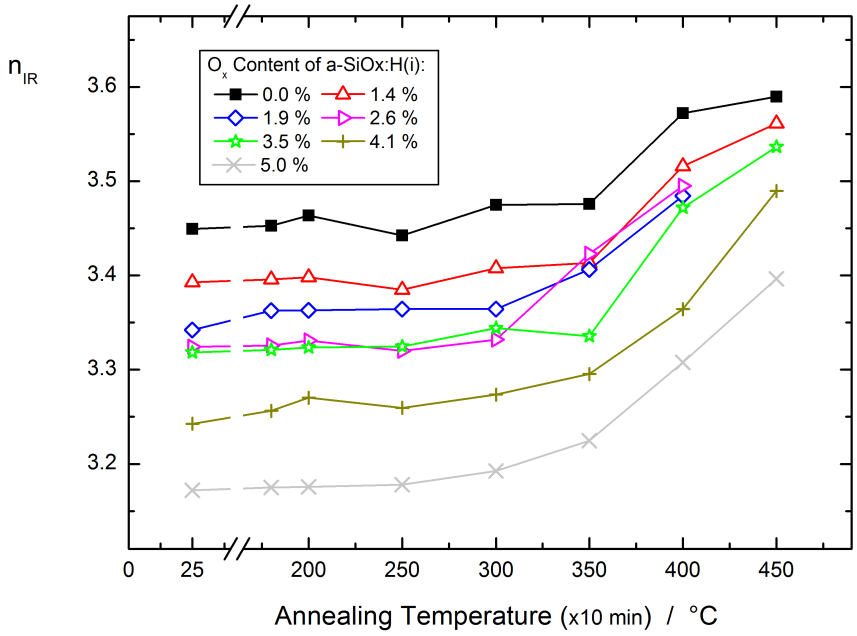

Figure 6.50: Thermal behaviour of *static* refractive index for a-SiO_x:H(i) layers

From the crystallization analysis the imaginary *pseudo*dielectric function was observed to increase with the thermal annealing. Knowing that $\epsilon_2 = 2nk$, an influence on the refractive index is expected. Figure 6.50 shows the *static* refractive index for a-SiO_x:H *intrinsic* layers. As known, the refractive index is related to the density of a material, therefore the changes observed indicate a modification in the microstructure that we have already described above. It is interesting to observe that until 300°C the n_{IR} remains mostly constant. The strong increase in the last three annealing steps can be explained by the fact that the material is acquiring a new density, due to the thermal relax of the amorphous structure expressed as a crystallization collapse. This result can be correlated with the increase of the thickness of the *interface* layer (see figure 6.28), that contains a certain density of crystallites.

The absorption (or the transparency) of the layer can be affected by the annealing temperature as well. Figure 6.51 shows the optical gap E_{04} for a-SiO_x:H(i) layers. The results confirm the considerations of Mueller in [Muel10], where the decrease at high T annealing is attributed to the H effusion. Indeed the graph looks really similar to the FT-IR results of figures 6.31 and 6.30, meaning that the molecular anti-bonding states theory can be used for the interpretation of this phenomenon. Until 300°C we observed that only inter-diffusion of atomic H is occurring inside the layers, therefore the energy gap remains mostly constant: the height of the starting point is influenced by the oxygen, as observed in figure 6.21. The H effusion at high T corresponds to a reduction of the Si-H anti-bonding states, and so a reduction of the energy gap. Therefore the high T annealing provokes not only a degradation of the passivation, i.e. an increase of Si DB due to the breaking of Si-H bonds, as we observed on the previous paragraph, but also a reduction on the transparency of the thin film; the same thermal phenomenon is responsible of two degradating aspects for a SHJ solar cell: high density

of defects related recombination centres and increase of absorption losses.

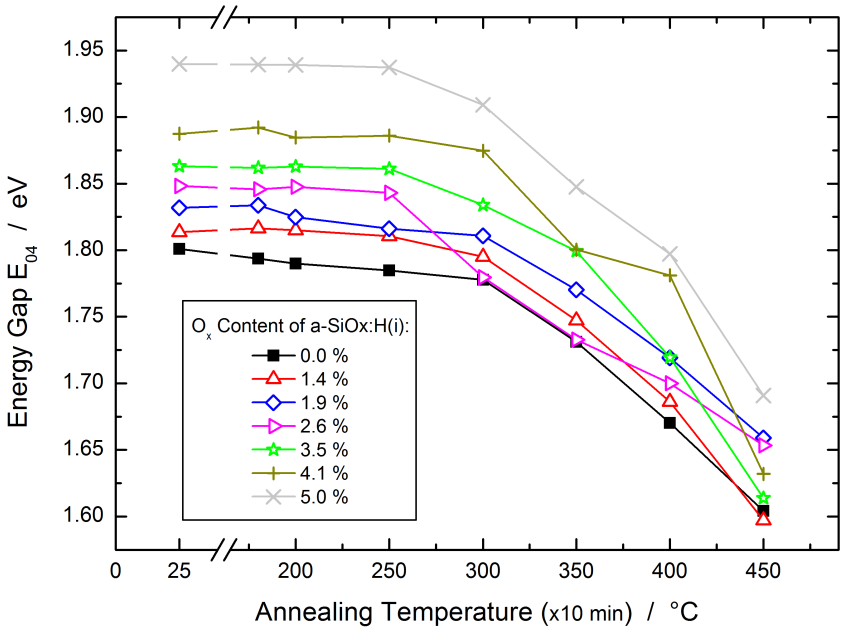

Figure 6.51: Energy gap E_{04} of a-SiO$_x$:H(i) layers as function of T annealing

6.2.5 Annealing effects on a SHJ solar cell

Knowing the effects that the annealing acts on the a-Si layers, it is possible to understand better the response of a real SHJ solar cell when exposed to thermal processes. Figure 6.52 shows the sketch of the solar cell that was produced with the a-Si:H buffer layer and the ITO only on the front side.

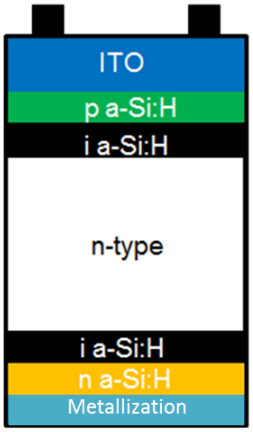

Figure 6.52: Sketch of the SHJ solar cell

This SHJ was exposed at a tempering of different annealing steps of 5' each (until 350°C). The *open-circuit* voltage of the solar cell measured after each annealing step is represented in figure 6.53. The graph is quite similar to the iV$_{oc}$ and SunsV$_{oc}$ results

obtained above. The influence of the H effusion at the highest tempering is evident, as a change in the parasitic absorption is occurred: therefore in this case as well, our results about the lifetime suggest that incorporation of O_x or C_y atoms in the *intrinsic* layer should lead to a lower output degradation.

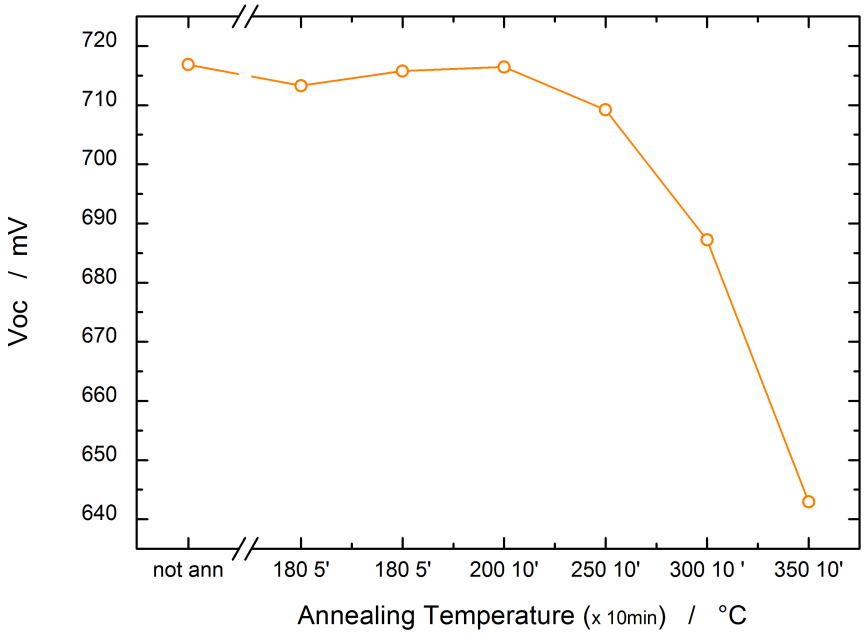

Figure 6.53: Voc from the SHJ solar cell

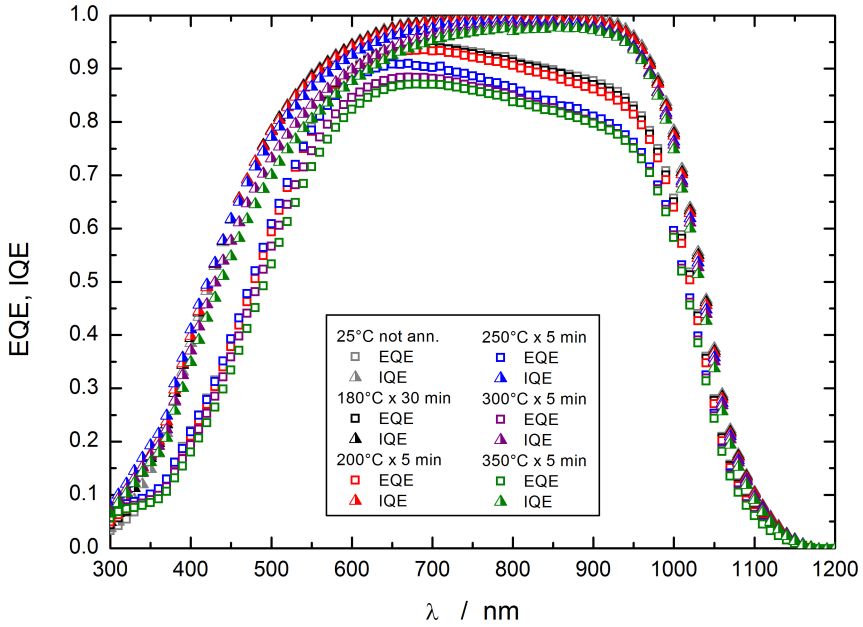

Figure 6.54: EQE, IQE and R for a SHJ solar cell

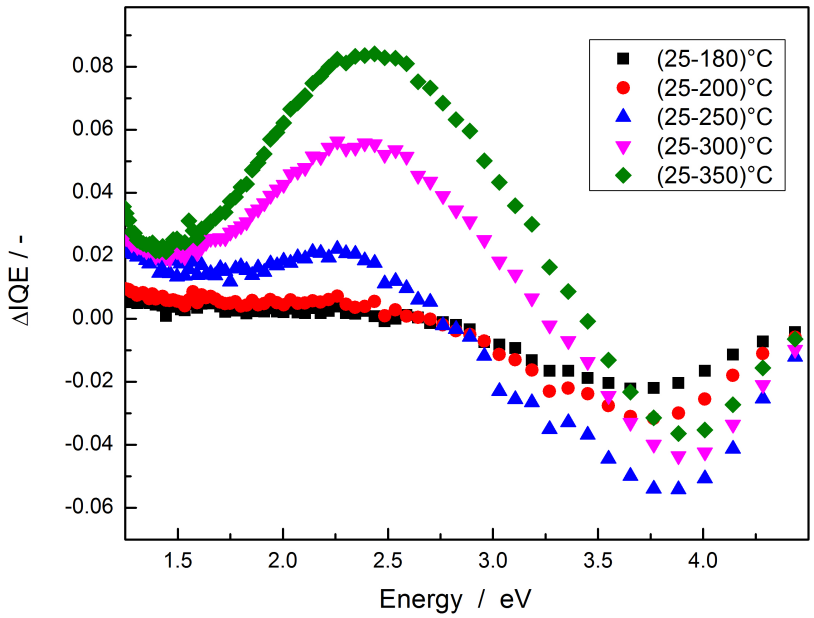

Figure 6.55: ΔIQE at each T annealing

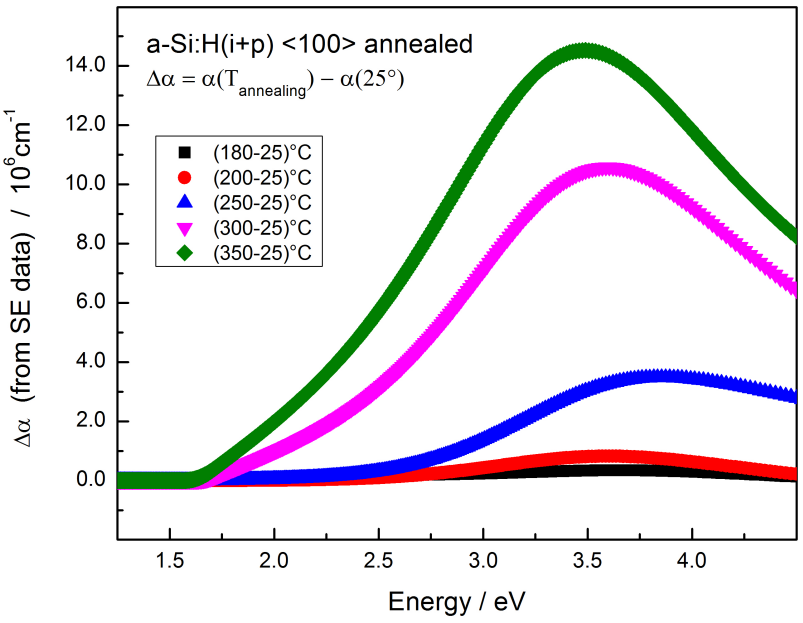

Figure 6.56: $\Delta\alpha$ from SE data of stack samples: a-Si:H(i)+a-Si:H(p)

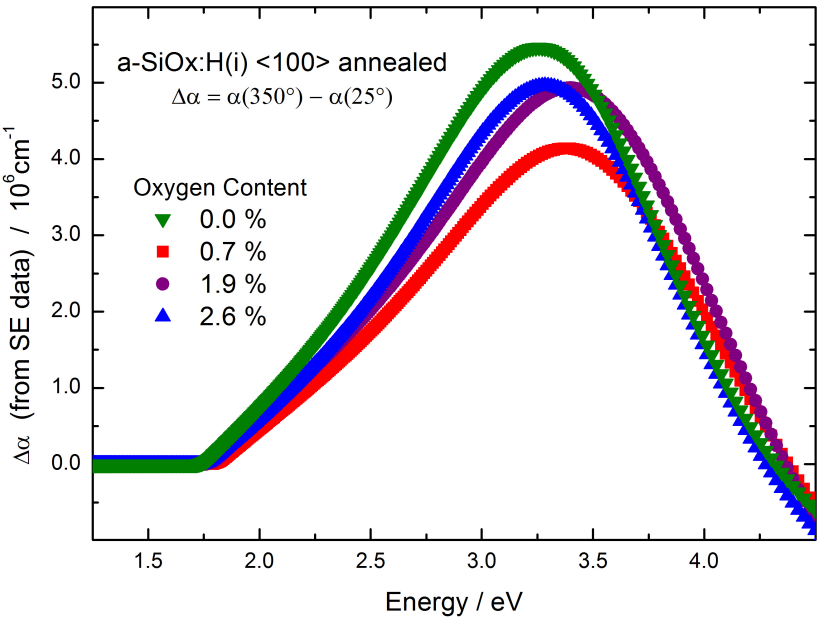

Figure 6.57: $\Delta\alpha$ from SE data of i samples: a-SiO$_x$:H(i)

The opto-electronic properties were measured by the pv-tool Loana-system, observing the *External* and the *Internal Quantum Efficiency*, defined as:

$$EQE = \frac{electrons/sec}{incident\ photons/sec} \tag{6.2}$$

$$IQE = \frac{electrons/sec}{absorbed\ photons/sec}. \tag{6.3}$$

The IQE is a quantity from which the effects of reflection are excluded and describes only the absorption within the cell. The *reflectance* quantifies the reflection losses at the surface. Figure 6.54 shows the EQE and the IQE as functions of the wavelength λ, after each annealing step. The annealing increases the *reflectance* and reduces the IQE and the EQE. Figure 6.55 shows even better the tempering effect: the graph represents, as function of the energy, the $\Delta IQE = IQE(25°C) - IQE(T_{annealing})$: considering just each thermal contribution, it is evident that increasing the temperature there are two different peaks of reduced efficiency. To investigate this thermal behaviour further it is necessary to check the absorption responses and the V$_{oc}$ signal, in order to compare these results with the previous observations.

In figure 6.56 the $\Delta\alpha = \alpha(T_{annealing}) - \alpha(25°C)$ for the stack layer i+p constituted by normal a-Si:H, without oxygen. The absorption coefficient was calculated with the formula

$$\alpha = \frac{4\pi k}{\lambda} \tag{6.4}$$

where the k values were extrapolated from the SE measurements.

A clear correspondence between $\Delta\alpha$ and ΔIQE can be established, meaning that the absorption losses in the a-Si layers (increased with the annealing), results already

observed in the previous paragraph with the decrease of the optical gap, reduce the final efficiency of the cell. Also, it has to be noted that not all the range is covered by the a-Si absorption losses; therefore the first peak of ΔIQE, positioned at low energy, can be attributed to the conductive ITO. At very short wavelength the improvement of the IQE is due to higher transparency in the TCO. These aspects are beyond the scope of this thesis and will not be discussed in more detail.

Studying the sub-oxides alloys we observed a better transparency, even at high T. So, in figure 6.57 it is represented the $\Delta\alpha$ of the 350°C thermal contribution. As the FT-IR spectra revealed, the effusion of the H occurs in a-SiO_x:H layers as well, hence there is always a transparency reduction. Anyway the incorporation of the oxygen give lower results of $\Delta\alpha$, suggesting that, if produced a solar cell with this kind of layers, lower reduction of IQE should be obtained.

To sum the part of the annealing effects on a SHJ solar cell it can be pointed out that the changes occurring in the range in which a-Si is absorbing could be qualitatively explained: H effusion leads to a decreased transparency of amorphous silicon.

Summary of the section 6.2

The experimental results of section 6.2, regarding the isochronal annealing experiments conducted to study the thermal properties of a-SiO_x and a-SiC_y layers, are resumed here.

- The crystallization of amorphous silicon layers was studied using the imaginary *pseudo*-dielectric function extracted from SE measurements: the samples with incorporated oxygen atoms did not crystallize as the normal a-Si:H, when exposed to 600°C, revealing the higher thermal stability of the alloy system.

- Effusion spectra were obtained calculating the hydrogen content from Si-H SM peaks at several annealing steps. H effusion evidenced a quite similar trend for a-Si:H, a-SiO_x:H and a-SiC_y:H samples; the main difference was that, increasing the atomic heterogeneity, the LSM peak was reduced and the HSM increased (as observed in section 6.1): this aspect remained dominant during all the annealing steps. Futhermore, samples from *AK400M*, resulted more stable (i.e. with less H effusion) than the ones deposited in the *Clustertool*: this observation is coherent with the voids content created during the deposition process, as the voids facilitate the hydrogen losses and the *Clustertool* processes create more porous amorphous layers.

- Lifetime and iV_{oc} measurements showed an improvement after thermal exposure only for low-content suboxide and subcarbide layers, that is under 3 % of O_x or C_y incorporation: the measured higher values, respect to a-Si:H, are explained in the range 180°C-250°C with an easier interdiffusion of H atoms passivating the Si DBs, at the interface with the substrate; in the range 300°C-450°C higher lifetime is related to a reduced hydrogen effusion. Samples with $C_O > 3\%$ exhibited a degraded passivation quality of the amorphous silicon layer, due to the high percentage of voids, with an higher number of both weak Si-H bonds and Si DBs.

- Increase of the *static refractive index* n_{IR} due to a re-arrengement of the amorphous network (approaching to a crystalline state) and decrease of the energy gap due to the H losses (meaning a reduced transparency of the layer under tempering) were observed in the range 300-450°C; the alloy system clearly showed a retardation in the thermal effect on these optical properties.

- EQE, IQE and reflectance measurements were made on a real solar cell, containing a-Si:H as passivating layer: the reduced *internal quantum efficiency* ΔIQE during the annealing steps (180-350°C) showed good correlation with the corresponding reduced absorption coefficient $\Delta\alpha$ of the a-Si:H layer. Studying suboxide thin films, the $\Delta\alpha$ of a-SiO_x was observed to be higher than the one of a-Si:H, suggesting that, if a solar cell were produced with these passivating layers, lower reduction of IQE should be obtained.

6.3 Final considerations

A first consideration about the results of this thesis is spent on the Urbach energy. A new method was implemented in the present work to improve the fit of the Cody-Lorentz model, and to obtain more reliable values, consists in the use of an *EMA* layer containing a specific voids content. The linear fit in the left plot of figure 6.58 confirms and explains the trend shown in figure 6.19: the disorder expressed by the Urbach parameter, that gives informations about the electronic tail states, is intimately correlated to the porosity of the amorphous silicon. The voids percentage, as already mentioned in paragraph 6.1.2d, depends on the plasma deposition process and increases with the oxygen incorporation. The first conclusion is that a-SiO_x:H is a more porous and therefore a more *disordered* material than standard a-Si:H.

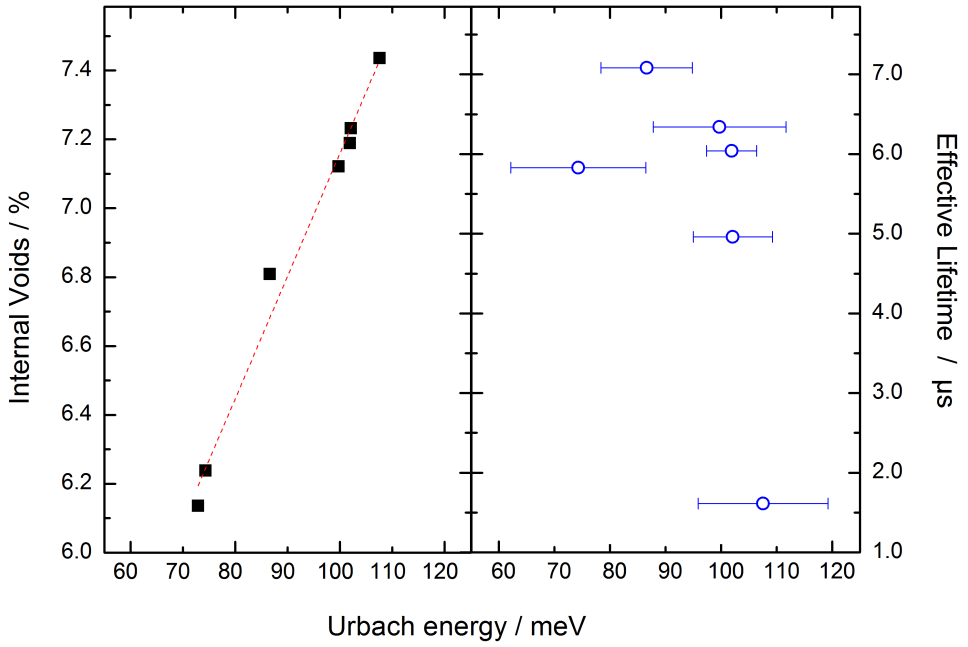

Figure 6.58: Internal voids content (left) and effective lifetime (right) vs Urbach energy of a-SiO_x:H(i) layers. The line in the left is a guide to the eye

The right plot of figure 6.58 shows how the lifetime is related to the Urbach energy. The large error bars reduce a complete understanding on how structural disorder could influence the quality passivation. Anyway it is clear that only little incorporation of oxygen in the sub-alloy layer ($< 3\%$), corresponding to a small increase of the Urbach energy ($\lesssim 100$ meV) can give a high effective lifetime; while a larger incorporation - i.e. a larger disorder - degrades the opto-electronic properties of the deposited material. A slight decrease of the lifetime with increasing Urbach energy was observed by Schulze [Sch11], investigating standard a-Si:H with different temperature depositions. In our results the decrease is quite sharp, as the influence of the oxygen on the passivation of DBs is quite strong. A suboxide a-Si layer, as mentioned above, has a more complex and disordered structure: this fact explains not only the deep decrease of the lifetime but also the discrepancy between our values of Urbach energies and the ones shown

in [Sch11]. Also, the deposition process is affecting the hydrogen incorporation and the voids content of the film, explaining the differences from the comparison of two different plasma processes as well.

The figure 6.59 contains the main results obtained in the annealing experiments: the high temperatures, i.e. from 300°C until 450°, provoking abundant H effusion, cause two different combined deteriorations for a-Si layers: the reduction of the transparency of the layer, as the decrease of the energy gap involves an increase of the absorption losses, and the photo-generated charge carriers lifetime degradation, as the thermal stress leaves many non-saturated Si DB.

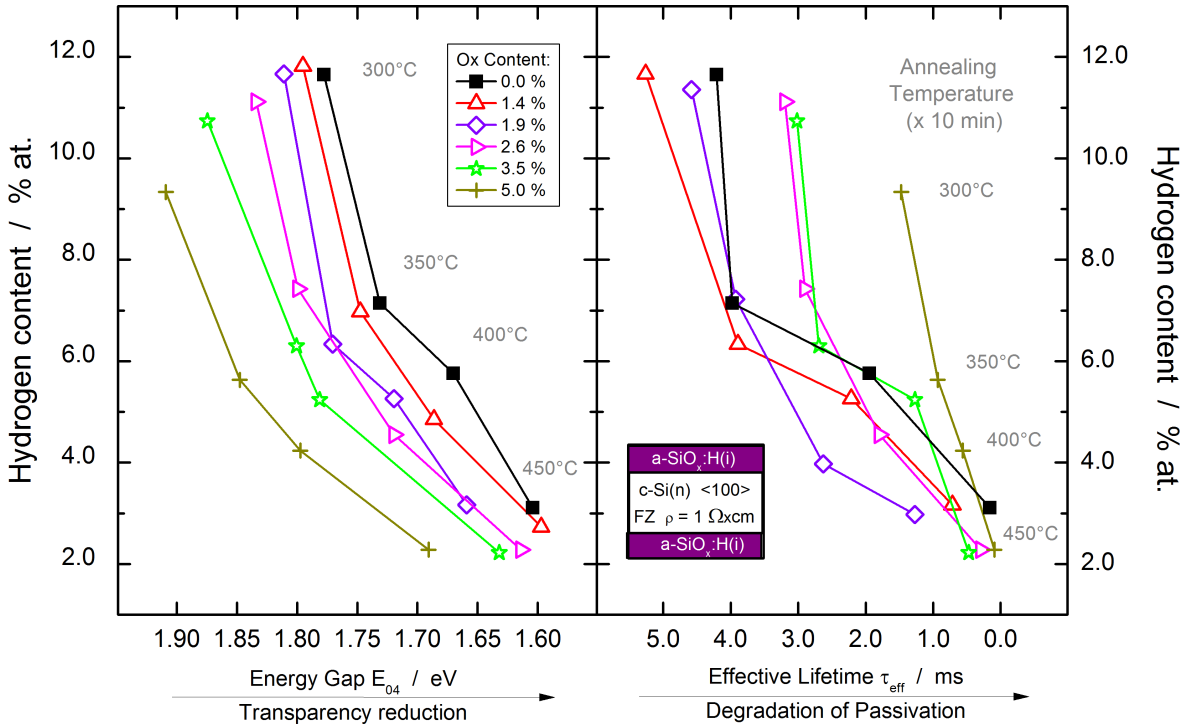

Figure 6.59: High T phenomena on a-SiO$_x$(i):H layers: H effusion, lifetime degradation, transparency reduction

These two correlations can be explained with the following theoretical models:

- the molecular orbital theory, where the anti-bonding states of Si-H molecules contribute to a wide band gap; as these bonds are destroyed by the annealing, the layer absorbs a higher number of photons, reducing the current output.
- the SRH theory by which the recombination rate is inversely proportional to the density of the DB, that increases with the H effusion; so the lifetime and the V$_{oc}$ output decrease down to a degraded state.

The latter behaviour was identified as a *stretched-exponential decay*, see [DWo08], caused by the hydrogen release from the trap sites, that have a distribution of energies and barrier heights to overcome: this interpretation considers the system as

relaxing toward the equilibrium (breaking of Si-H bonds) from the agitated state due to the thermal stress.

The effect of the oxygen introduction inside the a-Si layer, as already discussed, is an increase of the transparency (energy gap) and a reduction of the lifetime degradation: therefore the sub-alloy system can be considered a way to quantitatively reduce these thermal effects on the amorphous silicon.

As was seen previously, figure 6.23 relates the energy gap with a simulated short-current density from a SHJ front side constituted by a-SiO_x:H(i)/a-Si:H(p)/ITO. A relationship can be imposed between the iV_{oc} and the J_{sc}, obtained for different oxygen content, as plotted in figure 6.60. From this last graph it is clear that the just described thermal improvement of as deposited sub-oxide a-Si layer can be realized only under specific restrictions of the output characteristics: as predicted from the Urbach energy considerations, with low oxygen content (i.e. $<$ 5% for our deposition system) a well passivating layer can be obtained, as higher O content in the sub-alloys resulted in a higly disordered and porous structural network, with a tendency to incorporate more molecular H_2 inside the voids than saturating the Si DB. This latter hypothesis is in agreement with [Ein10b] and seems to be coherent with our observations.

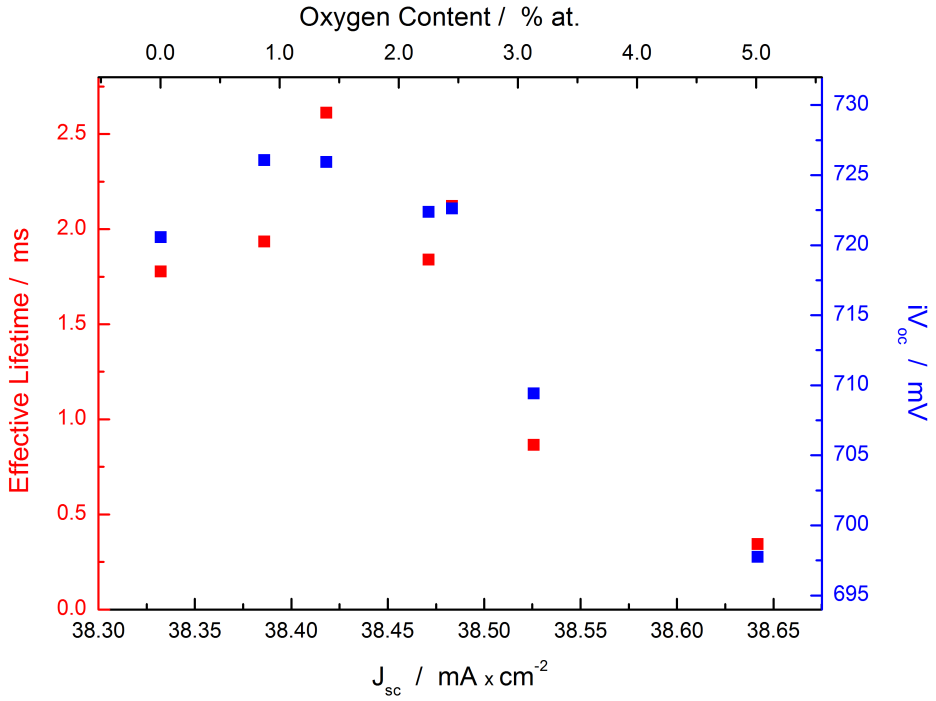

Figure 6.60: Lifetime (and iV_{oc}) vs simulated J_{sc} for different oxygen content in a-SiOx:H layers

6.4 Errors analysis

6.4.1 Structural investigation

Deposition Process

As mentioned during the discussion of the results, the plasma enhanced CVD constitutes a difficult process to stabilize, and the reproducibility of deposition results is an important issue related to the large amount of involved process parameters. The single process therefore can strictly influences the physical properties of the deposited a-Si thin layers, like the Si DB saturation, the epitaxial growth of the interface, a defined incorporation of the desired atomic specie.

The sub-alloy deposition showed that oxygen and carbon atoms, like in the primitive form of some CO_2 or CH_4 radical molecules, can remain adsorbed on the surfaces of the vacuum chamber walls: during a further deposition this can cause the presence of a non-desired atomic specie inside the layers. Therefore it was necessary to open and clean the vacuum chamber after the depositions occurring with CO_2.

As said, for the process many parameters have to be set. Actual temperature during deposition however is lower than the set-temperature due to thermal equilibrium with the surroundings of the cold wall reactor.

An other quantity difficult to reproduce is an exact value of the nm-size thickness d of a-Si layers: the overall deposition showed a statistical error of $\Delta d = \pm 1$ nm. Considering our samples of about 11 or 15 nm, the absolute error is $\Delta d/d = 6 - 10\%$. Anyway in the investigations of this thesis no influence or high dependency was observed from the thickness of the layers on the measured quantities (like the density from FT-IR, or the crystallinity from the SE).

SE analysis

Considering the spectroscopic ellipsometer for all the characterizations the pseudo-dielectric function was assumed valid but, as specified at the beginning, it comes from an optical model and is an indirect measurement quantity, a fact that could bring some suspect about the reliability of the results. However the large use that was made in literature authorizes to trust the physical behaviour that come from these pseudo-optical functions.

Also, the fitting procedure coming from SE was found to be less suitable with thick samples (for example the *i+p* stack), and with abundant oxygen incorporated: for *intrinsic* films an $MSE = 1.6 \div 2.8$ was found while for the entire stack the MSE was $3.0 \div 4.8$. This could bring observational errors especially on the considerations about the stack samples.

FT-IR and Contents calculation

The evaluation of the FT-IR spectra, with the related issues as the baseline and the fringes correction, was already discussed in paragraph 5.1.2: this entire analysis could bring wide errors ($\approx 30\%$, as seen by [Suw11]) in the exact estimation of the peak integral.

The errors propagation theory was used to observe the fluctuations in the contents calculation, using the formula for a function f depending from a variable x:

$$\Delta f = \left(\sum_{i=1}^{n} \left(\frac{\partial f}{\partial x} \Delta x_i \right)^2 \right)^{1/2} . \tag{6.5}$$

In our case the observed error in the H and Si density depends mostly from the peak integral. Considering only the gaussian deconvolution analysis an error $\Delta N \approx 10^{18}$ and $\Delta C_X < 1\%$ for the atomic densities and the contents was obtained. Considering the uncertainty brought back from the spectra correction, the estimated error is $\Delta C_X = 3 \div 5\%$, confirming the analysis of Schulze [Sch11].

Also, two sources of systematic errors were found in the theoretical assumptions:

- in the LL relation (eq. 5.15) the atomic densities do not take account of the internal voids. This could lead to an overestimation of the N_{Si}, that is anyway more accurate than the generally used $N_{Si} = N_{cSi} = 5 \times 10^{22}\ cm^{-3}$ like in [Sme07], [Sch11].
- the choice of the oxygen constant $C_{Si-O-Si} = 1.48 \times 10^{19} cm^{-2}$ by [Ino95] is also an arbitrary selection, that does not consider the fluctuations of the Si-O effective charge: anyway the rough confirmation by Einsele in [Ein12] allows to consider this content estimation reliable.

6.4.2 Open-air thermal measurement

The oxidation of the a-Si layers is an issue that was widely treated in literature (see for example [Bro11]). In our measurements the air exposure after the deposition caused the growth of an oxide surface on top, clearly distinguishable from SE fitting procedure and from the non-annealed spectra of FT-IR (giving an additional, but negligible, error to the oxygen estimation). This was also the reason why in the SE model a roughness layer was found to give the highest MSE.

The annealing on the hot-plate at ambient-air was observed to highly increase the oxidation rate of the surface layer and of the Si-O-Si SM peak. No influence anyway was found in the content calculations (the C_O was obtained just from the non-annealed samples) and on the optical functions (the k values of the Si-Ox layer are 0 at each wavelength, total transparency).

The hotplate gave an instrumental error of $\Delta T = \pm 1°C$; and the annealing time exposure can be considered fluctuating as well of around $\Delta t = \pm 5 - 10\ s$: these errors could bring uncertainty on the estimation of the H effusion or the lifetime, due to their influence on the energy budget needed to break a Si-H bond.

Finally, for the lifetime measurement itself the principal errors that can be identified are the uncertainty of the resistivity of the wafer given by the manufacturer (usually $\Delta\rho = \pm 0.02\ k\Omega$) and the one related to the choice of the optical constant for the calculation of the iVoc.

CHAPTER 7

Conclusion

In this thesis different *intrinsic* sub-oxide and sub-carbide alloys of hydrogenated amorphous silicon (a-Si:H) thin films were deposited and investigated, with the aim to create alternatives to the standard a-Si passivation layers for *silicon heterojunction* (SHJ) solar cells, which are stable up to 400°C. The objective is to avoid the thermal degradation of their opto-electronic properties, especially the passivation, during the post-deposition processes (like the metallization).

Optical tools, as *Fourier transform infrared spectroscopy* (FT-IR) and *spectroscopic ellipsometry* (SE), were used to observe the bonding configurations and the structural properties of the PECV deposited thin films. For the first time for silicon solar cells the H, O_x and C_y content was evaluated qualitatively using purely FT-IR and SE: a new method consisting in a combination of the Brodsky-Cardona-Cuomo analysis of FT-IR spectra [BCC77] and the Lorentz-Lorenz relation was studied, which allowed to explicitly calculate the N_{Si} for amorphous silicon, without using a constant value for it as usually done in literature. The deposition results showed that the incorporation of low percentage ($< 10\%$) of oxygen and carbon atoms inside the amorphous silicon allows to tune the density and the transparency of the layers. This was confirmed with *secondary ion mass spectroscopy* (SIMS) data of a previous work. The alloy system was observed to contain more voids, which increase almost linearly with the atomic heterogeneity, and a higher mean-bond-angle dilated network. The increase of the *amorphousity grade* corresponds to a higher long range disorder of the nano-sized structure, confirmed by the increase of Urbach energy, parameter extrapolated from the Cody-Lorentz optical model, as recently shown in [Ge13]. A new method to evaluate the Urbach energy measurements was used for the first time. This involves the addition of an *effective medium approximation* (*EMA*) layer in the fit analysis, with the voids percentage inserted as a fixed value obtained by FT-IR: this method gives more reasonable values respect to the ones over-estimated from the Cody-Lorentz model.

Also, the growing amount of additional voids was seen to be coherent with the shifting from low stretching mode to the high stretching mode of the Si-H IR absorption peak (as the hydrogen acquires more energy to vibrate in a more dilated structure, where the O_x or C_y have modified the dipolar surrounding) and with the mostly linear

decrease of the *static refractive index*, n_{IR}: these observations confirm the results of Einsele [Ein12]. FZ c-Si wafers were used for the a-Si deposition, with <100> and <111> surface orientations. The <111> wafers showed lower *coordination number* <r> and a lower Si-O-Si absorption frequency, i.e. a lower bonding-angle, revealing a slightly different atomic arrangement. The stack system (*intrinsic + p-doped* layers) was observed to have a higher density than the single layer, and hence a higher refractive index, a higher voids percentage and higher H content: these aspects are explained mainly by the two subsequent depositions processes, with an hydrogenation between the two a-Si thin films. This phenomenon was not found in literature and is strictly related to the process for which it was described.

Isochronal annealing measurements were performed to study the structural and the electronic changes of a-Si after stress exposure induced by tempering. The Si-rich a-SiO_x:H and a-SiC_y:H layers exhibited a higher thermal robustness, as no crystallization occurred after high T exposure ($\approx$ 600 °C), differently from the standard a-Si:H. Hydrogen effusion measurements were executed studying the decrease of the FT-IR signal (Si-H SM mode). Annealing temperatures $<$ 300 °C were observed to stimulate H inter-diffusion, improving the Si DB passivation at the interface with the wafer and therefore the *effective lifetime* τ; on the other hand at higher temperatures (especially in the range 300-450 °C) abundant hydrogen effusion takes place due to the Si-H bonds' rupture, causing two combined deteriorations of a-Si layers: electronic degradation and transparency reduction (observed by the decrease of the energy gap). A low percentage of oxygen (or carbon), i.e. $C_{O(C)} \leq 3.5\%$, was seen to be necessary to avoid that the high porosity of the sub-alloy layer cooperates with the tempering, facilitating the H effusion: this hypothesis was taken from [Ein12] and seems to be coherent with our analysis. The results concerning the relationship between H effusion and lifetime degradation (particularly the Fermi-level dependent defects inside the stack systems) confirm the findings of De Wolf about a-Si:H [DWo07]. However alloying of a-Si alone does not yet improve the temperature stability as seen from the comparison with layers from different deposition tools.

The content determination of H, O and C was substantially improved by the implementation of a more developed and realistic model, enabling the analysis of a-Si alloys with simple techniques like SE and FT-IR. This lead to the finding that the incorporation of carbon or oxygen atoms increases the disorder which also resulted in an increased Urbach energy. Finally, studying a-SiO_x:H and a-SiC_y:H, allowed us to conclude that incorporating low percentages of oxygen or carbon atoms inside the a-Si buffer layer of a SHJ solar cell increase the thermal stability of about 50°C as compared to pure a-Si:H.

Nomenclature

Abbreviations

a-Si:H	Amorphous silicon hydrogenated
AM	Air mass
BCC	Brodsky-Cardona-Cuomo method
BSF	Back surface field
CL	Cody Lorenz
CRN	Continuous random network
CZ	Czochralski
DB	Dangling bond
EMA	Effective medium approximation
EQE	External quantum efficiency
FF	Fill factor
FT-IR	Fourier transform infrared spectroscopy
FZ	Float-zone
HIT	Heterojunction with an intrinsic thin layer
HOMO	Highest occupied molecular orbital
HSM	High stretching mode
ICP	Coupled inductive plasma
IQE	Internal quantum efficiency

L-L	Lorentz-Lorenz
LRD	Long range disorder
LRO	Long range order
LSM	Low stretching mode
LUMO	Lowest unoccupied molecular orbital
MSE	Mean standard error
PECVD	Plasma enhanced chemical vapour deposition
PV	Photovoltaic
PVD	Physical vapour deposition
QSSPC	Quasi steady-state photoconductance
RBM	Random bonding model
RDF	Radial atomic distribution function
SE	Spectral ellipsometry
SHJ	Silicon heterojunction
SIMS	Secondary ion mass spectrometry
SRH	Schokley-Read-Hall
SRO	Short range order
SWE	Staebler-Wronsky effect
TCO	Transparent conductive oxide
TL	Tauc Lorentz
WM	Wagging mode

Symbols

<r>	Average coordination number
α	Absorption coefficient
η	Efficiency
C_{ω_0}	Absorption constant
E_{04}	Optical energy gap defined as energy value at $\alpha = 10000$ cm^{-2}
I_{mpp}	Current at maximum power point

J_{los}	Current density losses
J_{sc}	Short-circuit current density
N_H	Hydrogen atomic density
n_∞,n_{IR}	Static refractive index
V_b	Built-in potential
V_{mpp}	Potential at maximum power point
iVoc	Implied open-circuit voltage
C_O	Oxygen content (atomic percentage)

List of Figures

List of Tables

Bibliography

[Ang08] H. Angermann, L. Korte, et al.: *Optimisation of electronic interface properties of a-Si:H/c-Si hetero-junction solar cells by wet-chemical surface pre-treatment.* Thin Solid Films **516(20)** 6775-6781 (2008).

[Asp83] D.E. Aspnes and A.A. Studna: *Dielectric functions and optical parameters of Si, Ge, GaP,GaAs, GaSb, InP, InAs and InSb from 1.5 to 6.0 eV.* Phy. Rev. B **27-2** 985 (1983)

[Bas10] D. K. Basa et al.: *Spectroscopic ellipsometry study of hydrogenated amorphous silicon carbon alloy films deposited by plasma enhanced chemical vapor deposition.* Journ. of Appl. Phys. **107**, 023502 (2010)

[BCC77] M. H. Brodsky, M. Cardona, and J. J. Cuomo: *Infrared and Raman Spectra of the silicon-hydrogen bonds in amorphous silicon prepared by glow discharge and sputtering* Phys. Rev. B **16** 3556 (1977).

[Bea78] K.E. Bean: *Anisotropic etching of silicon.* IEEE Transactions on Electron Devices ED-25(10) 1185-1193 (1978).

[Biv07] M. Bivour: *Realisierung eines neuartigen Kontaktsystems fuer rueckseitig kontaktierte amorph/kristalline Silizium-Heterosolarzellen.* Diplomarbeit, Fachhochschule fuer Technik und Wirtschaft, Berlin (2007).

[Biv10] M. Bivour, C. Meinhardt, D. Pysch, C. Reichel, K.-U. Ritzau, M.Hermle, S.W. Glunz: *n-type Si solar cells with amorphous/crystalline Silicon Heterojunction rear emitter.* Presented at the 35th PVSC, June 20-25, 2010, Honolulu, Hawaii

[Biv12] M. Bivour, C. Reichel, M. Hermle, S. W. Glunz: *Improving the a-Si:H(p) rear emitter contact of n-type silicon solar cells* Solar Energy Materials & Solar Cells **106** 11–16 (2012)

[Bor97] A. Borghesi, A. Sassella et al.: *Ellipsometric characterization of amorphous and polycrystalline silicon films deposited using a single wafer reactor* Appl. Phys. Lett **70**(7) 892 (1997)

[Bro11] A.C. Bronneberg, A.H.M. Smets, M. Creatore, M.C.M. van de Sanden: *On the oxidation mechanism of microcrystalline silicon thin films studied by Fourier transform infrared spectroscopy* Journal of Non-Crystalline Solids **357** 884-887 (2011)

[Car80] M. Cardona et al.: *Infrared Spectrum and Structure of Hydrogenated Amorphous Silicon* Phys. Stat. Sol. (b) **100**, 43 (1980)

[Car83] M. Cardona: *Vibrational Spectra of Hydrogen in Silicon and Germanium* Phys. Stat. Sol. (b) **118**, 463 (1983)

[Cha95] Chapin, D.M., Fuller, C.S., Pearson, G.L.: *A new silicon p-n junction photocell for converting solar radiation into electrical power.* J. Appl. Phys. **25**, 676-677 (1995)

[Cod84] G.D. Cody: *Semiconductors and Semimetals* edited by J.I. Pankove vol. **21B** p.11 (1984)

[Col00] R.W. Collins et al. : *Real time analysis of amorphous and microcrystalline silicon film growth by multichannel ellipsometry* Thin Solid Films **364** 129-137 (2000)

[Cus94] J. S. Custer, M. 0. Thompson et al.: *Density of amorphous Si* Appl. Phys. Lett. **64** 437 (1994)

[Dem12] B. Demaurex, S. De Wolf, A. Descoeudres, Z. C. Holman and C. Ballif: *Damage at hydrogenated amorphous/crystalline silicon interfaces by indium tin oxide overlayer sputtering* Appl. Phys. Lett. **101** 171604 (2012)

[Des11] A. Descoeudres et al.: *Improved amorphous/crystalline silicon interface passivation by hydrogen plasma treatment* Appl. Phys. Lett. **99**, 123506 (2011)

[Din13] K. Ding et al.: *Optimized amorphous silicon oxide buffer layers for silicon heterojunction sola cells with microcrystalline silicon oxide contact layers.* Journ. of Appl. Phys. **113**, 134501 (2013)

[DWo07] S. De Wolf and M. Kondo: *Boron doped a-Si:H/c-Si interface passivation: Degradation mechanism* Appl. Phys. Lett. **91**, 112109 (2007)

[DWo08] S. De Wolf and al.: *Stretched-exponential a-Si:H/c-Si interface recombination decay.* Appl. Phys. Lett. **93**, 032101 (2008)

[DWo10] S. De Wolf, A.Descoeudres: *High-efficiency heterojunction solar cells: From physics to production lines* Solid-State and Integrated Circuit Technology (ICSICT) (2010)

[DWo12] S. DeWolf, A. Descoeudres, Z.C. Holman and C.Ballif: *High-efficiency Silicon Heterojunction Solar Cells: A Review* Green, Vol.**2** (2012)

[Efs92] H. Efstathiadis: *Atomic bonding in amorphous hydrogenated silicon carbide alloys: A statistical thermodynamic approach* Phys. Rev. B **46**, 13119-13130 (1992)

[Ein10a] F. Einsele: *Amorphe Siliziumoxidschichten zur Oberflaechenpassivierung und Kontaktierung von Heterostruktur-Solarzellen aus amorphem und kristallinem Silizium* PhD thesis - Fakultaet fuer Elektrotechnik und Informationstechnik der Rheinisch-Westfaelischen Technischen Hochschule Aachen (2010)

[Ein10b] F. Einsele, W. Beyer, and U. Rau: *Annealing studies of sub-stoichiometric amorphous SiO_x layers for c-Si surface passivation.* Phys. Stat. Sol. C **7**, No. 3-4, 1021-1024 (2010)

[Ein12] F. Einsele, W. Beyer, and U. Rau: *Analysis of sub-stoichiometric hydrogenated silicon oxide films for surface passivation of crystalline silicon solar cells* Journal of Applied Physics **112** 054905 (2012)

[Enig] http://www.enigmatic-consulting.com, looked up on 17/06/2013

[Eu-Pan13] http://eu-solar.panasonic.net, looked up on 17/06/2013

[EUPV07] EU PV technology platform. *A strategic research agenda for photovoltaic solar energy technology* (2007)

[Fer02] A.S. Ferlauto, G.M. Ferreira, J.M. Pearce, C.R. Wronski, R.W. Collins, X. Deng, G. Ganguly, J. App. Phys. **92** (2002) 2424.

[Fuj07] H. Fujiwara: *Spectroscopic Ellipsometry: Principles and Applications* John Wkiley and Sons, Ltd (2007)

[Fuj07b] H. Fujiwara et al.: *Application of hydrogenated amorphous silicon oxide layers to c-Si heterojunction solar cells* Appl. Phys. Lett. **91**, 133508 (2007)

[Gas11] F. Gasparri: *Optoelectronic Properties of Amorphous Silicon the Role of Hydrogen: From Experiment to Modeling* University of Ontario Institute of Technology, Canada (2011)

[Ge13] J. Ge, T. Mueller et al.: *Analysis of intrinsic hydrogenated amorphous silicon passivation layer growth for use in heterojunction silicon wafer solar cells by optical emission spectroscopy* J. Appl. Phys. **113**, 234310 (2013)

[Gri86] P. R. Griffiths and J. A. de Haseth: *Fourier Transform Infrared Spectroscopy* John Wiley and Sons, New York, (1986).

[Gru06] Marius Grundmann *The Physics of Semiconductors, An Introduction Including Devices and Nanophysics* Springer (2006)

[Hal52] R. N. Hall: *Electron-hole recombination in germanium*, Physical Review **87**, 387 (1952).

[Har10] A. M. Hartel et al. : *Amorphous Si_xC_{1-x}:H single layers before and after thermal annealing: Correlating optical and structural properties* Solar Energy Materials **94** 1942-1946 (2010)

[Her2012] J. L. Hernandez et al. : *High Efficiency Silver-Free Heterojunction Silicon Solar Cell* Japanese Journal of Applied Physics **51** 10NA04 (2012)

[Hig90] Higashi, G. S., Y. J. Chabal, et al.: *Ideal hydrogen termination of the Si(111) surface.* Applied Physics Letters **56(7)** 656-658 (1990).

[Hig90] G. S. Higashi et al., Appl. Phys. Lett. **56**, 656 (1990)

[Hol12] Z. C. Holman et al. : *Current Losses at the Front of Silicon Heterojunction Solar Cells* Journ. of Photovoltaics, **2** 1 (2012)

[Ifi10] S. M. Ifiquar: *Structural Studies on Semiconducting Hydrogenating Amorphous Silicon Oxide Films* Energy Research Unit, Indian Association for the Cultivation on Science

[Ino95] L. He, T. Inokuma, Y. Kurata, and S. Hasegawa, J. Non-Cryst. Solids **185** 249 (1995).

[Jan04] A. Janotta: *Doping and its efficiency in a-SiOx:H .* Phys. Rev. B **69**, 115206 (2004)

[Jan06] S. Janz: *Amorphous Silicon Carbide for Photovoltaic Applications* PhD Thesis, Fraunhofer ISE Freiburg (2006)

[Jan97] T. Jana et al.: *Silicon oxide thin films prepared by a photo-chemical vapour deposition technique* Journal of material science **32** (1997) 4985-4900

[Jel94] Jellison, G. E., Jr. and F. A. Modine: *Optical functions of silicon at elevated temperatures.* Journal of Applied Physics **76**(6): 3758- 3761 (1994).

[Jon41] R. C. Jones: *New calculus for the treatment of optical systems. Description and discussion of the calculus.* Journal of the Optical Society of America **31** Nr. 7, 488-49 (1941)

[Ker03] M. J. Kerr, A. Cuevas, and P. Campbell. *Limiting Efficiency of Crystalline Silicon Solar Cells Due to Coulomb-Enhanced Auger Recombination.* Progress in Photovoltaics: Research and Applications **11** 97-104 (2003)

[Kol04] A. Kolodziej: *Stabler-Wronsky effect in amorphous Silicon and its alloys* Opto-Electronic Review **12(1)** 21-32 (2004)

[Kon07] M. Kondo, S. De Wolf: *Abruptness of a-Si:H/c-Si interface revealed by carrier lifetime measurements.* Appl. Phys. Lett. **90**, 042111 (2007)

[Kra72] B. Kramer: *Electronic properties of amorphous solids* Adv. Solid State Phys. (Festkorperprobleme) **12**, 133 (1972)

[Kus87] M.J. Kushner: *On the balance between silylene and silyl radicals in rf glow discharges in silane: The effect on deposition rates of a-Si:H* J. Appl. Phys. **62** 2803 (1987)

[Lan92] A. A. Langford, M. L. Fleet, B. P. Nelson, W. A. Lanford, and N. Maley: *Infrared absorption strength and hydrogen content of hydrogenated amorphous silicon* Phys. Rev. B **45**, 13367 (1992).

[Lau87] P. Lautenschlager, M. Garriga et al.: *Temperature dependence on the dielectric function and interband critical points in silicon* Phys. Rew. **36-9** 4821 (1987)

[Lev03] D.Levi et al.: *In-Situ Studies of the Growth of Amorphous and Microcrystalline Silicon Using Real-Time Spectroscopic Ellipsometry* National Center for Photovoltaics and Solar Program Review Meeting Denver, Colorado March 24-26, 2003

[Lor880] L. Lorenz, Ann. Phys. (Leipzig) **11** 702 (1880).

[Lort880] H. A. Lorentz, Ann. Phys. (Leipzig) **9** 641 (1880) .

[Los01] M. Losurdo, F. Roca, P. Capezzuto and G. Bruno: *Spectroscopic ellipsometry study of interfaces and crystallization behaviour during annealing of a-Si:H films* Thin Solid Films **383** 69-72 (2001)

[Los03] M. Losurdo et al.: *Dielectric function of nanocrystalline silicon with few nanometers (< 3 nm) grain size* Applied Physics Letters **82**-18 2993-5 (2003)

[Luc78] J. C. Knights, G. Lucovsky and R. J. Nemanich: *Hydrogen bonding in silicon-hydrogen alloys* Philosophical Magazine B VOL.**3-7** No. 4, 467-475 (1978)

[Luc83] G. Lucovsky, J. Yang, S. S. Chao, J. E. Tyler, and W. Czubatyj: *Oxygen-bonding environments in glow-discharge-deposited amorphous silicon-hydrogen alloy films* Physical Review B **28(6)**, 3225 (1983).

[Luc86] P.G. Pai, S.S. Chao, Y. Takag and G. Lucovsky: *Infrared spectroscopic study of SiOx films produced by plasma enhanced chemical vapor deposition* Journal of Vacuum Science and Technology A **4(3)** 689-94 (1986).

[Mat04] A. Matsuda: *Microcrystalline silicon. Growth and device application.* Journal of Non-Crystalline Solids **1-12** 338-340 (2004)

[McI10] S. C. Baker-Finch and K. R. Mcintosh: *A freeware program for precise optical analysis of the fron surface of a solar cell.* 35th IEEE Photovoltaic Specialists Conference, Honolulu (2010)

[McI12] S. C. Baker-Finch and K. R. Mcintosh: *OPAL 2: Rapid Optical Simulation of Silicon Solar Cells.* PV Lighthouse, Coledale, NSW 2515, Australia (2012)

[Mei10] Meinhardt, C., D. Pysch, et al.: *Optimization and analysis of deposition processes of amorphous silicon for silicon heterojunction solar cells.* Proceedings of the 25th European Photovoltaic Solar Energy Conference and Exhibition, Valencia, Spain (2010)

[Mon13] A. Mondon, M.N. Jawaid, J. Bartsch, M. Glatthaar, S.W. Glunz: *Microstructure Analysis of the Interface Situation and Adhesion of Thermally Formed Nickel Silicide for Plated Nickel-Copper Contacts on Silicon Solar Cells.* Paper not yet published.

[MSU] http://www.cem.msu.edu, looked up on 17/06/2013

[Muel10] T. Mueller et al.: *Crystalline silicon surface passivation by high-frequency plasma-enhanced chemical-vapor-deposited nanocomposite silicon suboxides for solar cell applications.* Journ. of Appl. Phys. **107**, 014504 (2010)

[Mun09] D. Munoz et al.: *Optimization of KOH etching process to obtain textured substrates suitable for heterojunction solar cells fabricated by HWCVD* Thin Solid Films **517** 12 3578-3580 (2009)

[Nag99] H. Nagel, C. Berge and A.G. Aberle: *Generalized analysis of quasi-steadystate and quasi-transient measurements of carrier lifetimes in semiconductors.* Journal of Applied Physics **86**(11), 6218-21 (1999).

[Phi72] H. R. Philipp: *Optical and bonding model for non-crystalline SiOx and SiOxNy materials* Journal of Non-Crystalline Solids **8-10** 627-632 (1972)

[Phs79] J. C. Phillips: *Topology of covalent non-crystalline solids I: Short-range order in chalcogenide alloys.* Journal of Non-Crystalline Solids, **34(2)** 153-181 (1979).

[PhysRut] http://www.physics.rutgers.edu, looked up on 17/06/2013

[Pie72] D.T. Pierce and W.E. Spicer: *Electronic Structure of Amorphous Si from Photoemission and Optical Studies* Physical Review B **5(8)** 3017-3029 (1972).

[Pow93] M. J. Powell and S. C. Deane, Phys. Rev. B 48, 10815 (1993).

[Pri11] P.S. Priambodo, N.R. Poespawati, D. Hartanto, Chapter book: Solar Cell Technology, INTECH Open Access Publisher (2011), ISBN 978-953-307-316-3

[Pved] http://www.pveducation.org/pvcdrom, looked up on 17/06/2013

[Rei08] K.A. Reinhardt and W. Kern: *Handbook of Silicon Wafer Technology* William Andrew Inc. (2008)

[Ric13] A. Richter, M. Hermle and S. Glunz: *Reassessment of the Limiting Efficiency for Crystalline Silicon Solar Cells* IEEE Journal of Photovoltaics, vol.PP, no.99, pp.1-8 (2013)

[Rob00] J. Robertson: *Deposition mechanism of hydrogenated amorphous silicon.* Journal of Applied Physics **87(5)** 2608-2617 (2000).

[Rob00] J. Robertson : *Deposition mechanism of hydrogenated amorphous silicon.* Journal of Applied Physics **87**(5): 2608-2617 (2000).

[Sch10] T. F. Schulze *Electrical transport mechanisms in a-Si:H/c-Si heterojunction solar cells* J. Appl. Phys. **107**, 023711 (2010)

[Sch11] T. F. Schulze *Impact of Fermi-level dependent defect equilibration on Voc of amorphous/crystalline silicon heterojunction solar cells*

[Sch74] H. Schlangenotto, H. Maeder and W. Gerlach: *Temperature dependence of the radiative recombination coefficient in Silicon*, physica status solidi a **21(1)**, 357-67 (1974).

[Schu11] J.-W. Schuttauf *Amorphous and crystalline silicon based heterojunction solar cells* Phd Thesis, University of Utrecht (2011)

[Sea98] T. Searle: *Properties of Amorphous Silicon and its alloys* INSPEC, The Institution of Electrical Engineers, University of Sheffield, United Kingdom

[Sho52] W. Shockley and W.T.J. Read: *Statistics of the recombinations of holes and electrons*, Physical Review **87(5)**, 835-42 (1952).

[Sin96] R. A. Sinton and A. Cuevas: *Contactless determination of current-voltage characteristics and minority carrier lifetimes in semiconductors from quasisteadystate photoconductance data* Appl. Phys. Lett. **69** 2510 (1996)

[Sme07] A.H. Smets: *Growth Related Material Properties of Hydrogenated Amorphous Silicon* Phd thesis, Eindhoven University of Technology (2003)

[Sog06] T. Soga: *Nanostructured Materials for Solar Energy Conversion* Nagoya Institute of Technology, Japan, Elsevier (2006)

[Sta77] D.L. Staebler and C.R. Wronski: *Reversible conductivity changes in discharge-produced amorphous Si* Appl. Phys. Lett. **31** 292-294 (1977).

[Str91] R. A. Street. *Hydrogenated Amorphous Silicon.* Cambridge University Press, 1991.

[Stu89] Stutzmann, M.: *The defect density in amorphous silicon.* Phil. Mag. B **60** 531-546 (1989)

[Suw11] D. Suwito: *Intrinsic and doped amorphous silicon carbide for the surface passivation of silicon solar cells* PhD Thesis, Fraunhofer ISE Freiburg (2011)

[Tan92] M. Tanaka et al.: *Development of New a-Si/c-Si Heterojunction Solar Cells: ACJ-HIT (Artificially Constructed Junction-Heterojunction with Intrinsic Thin-Layer)* Jpn. J. Appl. Phys. **31** (1992) pp. 3518-3522 RD Headquarters, Sanyo Electric Co., Ltd. Hashiridani, Hirakata, Osaka 573

[Tau66] J. Tauc, R. Grigorovici, and A. Vancu, Phys. Status Solidi **15**, 627 (1966).

[Tom] N. Tomozeiu: *Silicon Oxide (SiOx,* $0 \leq x \leq 2$*): a Challenging Material for Optoelectronics* RandD Department, Océ Technologies B.V., The Netherlands

[Tom05] H.G. Tompkins: *Handbook of Ellipsometry* Springer (2005)

[Urb53] F. Urbach: *The Long-Wavelength Edge of Photographic Sensitivity and of the Electronic Absorption of Solids.* Phys. Rev. **92**, 1324 (1953)

[vdH91] J. C. van den Heuvel, M. J. Geerts and J. W. Metselaar: *The relation between the optical properties and the hydrogen concentration in a-Si:H* Solar Energy Materials **22** 185-194 (1991)

[vSa11] W. van Sark, L. Korte and F. Roca: *Physics and Technology of Amorphous-Crystalline Heterostructure Silicon Solar Cells* Springer-Verlag Berlin Heidelberg (2011)

[vSw94] R. A. C. M. M. van Swaaij et al. : *Local structure and bonding states in a-$Si_{1-x}C_x$:H* Journ. of Appl. Phys. **76** 251 (1994)

[Wak98] M. Wakagi, H. Fujiwara, R. W. Collins: *Real time spectroscopic ellipsometry for characterization of the crystallization of amorphous silicon by thermal annealing* Thin Solid Films 313-314 464-468 (1998)

[Wikipedia] http://www.wikipedia.com, looked up on 17/06/2013

[Woo72] F. Wooten: *Optical properties of solids* Academic Press London (1972)

[Yab86] Yablonovitch, E., D. L. Allara, et al. : *Unusually low surface-recombination velocity on silicon and germanium surfaces.* Physical Review Letters **57(2)** 249-252 (1986).

[Zac32] W. H. Zachariasen: *The atomic arrangement in glasses* J. Am. Chem. Soc. **54(10)** 3841-3851 (1932)

Acknowledgement

Firstly I would like to thank Prof. Daniela Cavalcoli, Dr. Martin Hermle and the PhD student Kurt-Ulrich Ritzau for the supervision of the work. A special gratitude goes to Kurt, offering me the possibility to write my thesis at the Fraunhofer ISE and for the help and the support given in all these months.

I would also like to thank: Jan Holtkamp, Dirk Wagenmann and Karin Zimmermann for the labs introductions and the suggestions given to perform my experiments, Ankit Khanna for the metallization introduction, Antonio Leimenstoll and Felix Schaetzle for the samples cleaning.

My sincere thanks are addressed to all the colleagues of the F-building (SEC department), which gave me a pleasant stay at ISE: Torge Behrendt, Ino Geisemeyer, Vahid Gerami, Chu Haifeng, Davide Impera, Tim Niewelt, Repo Paivikki, Markus Reusch, Marc Ruediger, David Schuldis, Heiko Steinkemper. Particular thanks go to Valentina Roberti, her friendship was important during all this experience in Freiburg.

Furthermore, special thanks to the Roggatz family, who has first showed me the kindness and hospitality of Germans.

Finally I thank my parents, my brother Luca and my love Caterina for all the comforting and the encouraging words that helped me to go on with my motivations and my studies.